Astronomy Letters, Vol. 27, No. 1, 2001, pp. 1–14. Translated from Pis'ma v Astronomicheskiĭ Zhurnal, Vol. 27, No. 1, 2001, pp. 3–18.

Studies of the Fine Structure of the Object 1803+784

S. Britzen[1, 2], A. Witzel[1], T. P. Krichbaum[1], T. MacSlow[3], and L. I. Matveyenko[4]*

[1] *Max-Planck-Institut für Radioastronomie, Auf dem Hügel 69, Bonn, 53121 Germany*
[2] *Joint European Institute for Radio Astronomy, Holland*
[3] *Jodrell Bank, Nuffield Radio Astronomy Laboratories, UK*
[4] *Space Research Institute, Russian Academy of Sciences, ul. Profsoyuznaya 84/32, Moscow, 117810 Russia*

Received July 21, 2000

Abstract—We have investigated the fine structure of the object 1803+784 at a wavelength of 18 cm with an angular resolution of ~0.5 mas. The structure consists of a core (injector) and a jet. The angle of the relativistic plasma outflow is equal to the angle of a conical diverging helix—the trajectory of compact components, suggesting a similar shape of the jet. The helical structure and the curvature of the jet axis are assumed to be determined by rapid and long-period precession of the rotation axis. The core radio emission at 18 cm is attenuated by absorption in the ambient ionized medium (cocoon wall) by >25 db. The bright compact component is the nearby part of the jet extending outside the dense part of the screen. Ionization variations in the medium cause low-frequency radio variability. Screen parameters are estimated. © *2001 MAIK "Nauka/Interperiodica".*

Key words: *active galactic nuclei, object 1803+784, low-frequency variability, absorption, VLBI*

INTRODUCTION

Quasars, BL Lac objects, Seyfert galaxies, and galaxies with active nuclei share many common properties, including their structure in the form of a core and a jet, radio variability, and spectra with high-frequency excesses. They belong to the same class—active galactic nuclei (AGN) objects. Substantial progress in understanding the active processes in their cores, the formation mechanism of jets, their helical structure, and the nature of compact features and extended transverse structures identified with shock waves has been made by studying the hyperfine structure of these objects over a wide radio spectral range (Rantakuro *et al.* 1992; Matveyenko *et al.* 1996). Theoretical models have been developed for the observed structures (Bisnovatyĭ-Kogan *et al.* 1969; Shakura and Sunyaev 1973; Begelman *et al.* 1984; Falcke *et al.* 1995; Romanova *et al.* 1998).

The nature of the high-frequency radio outbursts attributable to the ejections of dense clouds of relativistic plasma and the cause of the low-frequency variability associated with transparency variations in the ionized medium that obscures the central part of the core region have been established (Marscher 1979; Matveyenko *et al.* 1980, 1992, 1996). Most AGN objects exhibit one-sided jets. The antijets that correspond to plasma flows moving in the opposite direction are assumed to be invisible, because the emission is highly beamed. However, they must be observed far from the injector outside the ionized medium. Thus, we do not completely understand what the limiting brightness temperature of compact components moving at relativistic velocities in a direction close to the observer's line of sight is. The limiting brightness temperature of a compact, optically thick cloud of relativistic plasma is bounded by Compton backscattering and is equal to $T_b = 10^{12}$ K (Kellermann and Pauliny-Toth 1969, 1981). The emission beaming of a cloud moving at a relativistic velocity ($v/c \approx 0.995$) reaches $\gamma \approx 10$, and the brightness temperature must increase by a factor of γ^2. However, no such high brightness temperatures of the components have been detected, within the limits of the measurement errors[1]. At the same time, no compact components of considerably lower brightness have been detected either, but this can be explained by the limited measurement sensitivity. The brightness temperatures of more extended structures, including distant parts of the jets, are recorded at $T_b \approx 10^7$ K.

The region of relativistic-plasma generation, acceleration, and injection is of particular interest. This region is observed as a bright compact radio source (core). Its emission has a flat spectrum and shows up most clearly at millimeter and centimeter wavelengths. The fine structure of the injector region must reflect the physical processes in it. The central regions of AGN objects are surrounded by an ionized medium observable in emission lines. This medium is transparent at high frequencies, but severely hampers observations at

* E-mail address for contacts: lmatveen@iki.rssi.ru

[1] The studies of Kellermann *et al.* (1998) in recent years show that some of the AGN objects have brightness temperatures $T_b \approx 10^{14}$ K.

Table 1. Parameters of VLBI stations

No.	Station	Antenna diameter, m	T_{sys}, K	F_{sys}, Jy	δF, mJy
1	Onsala	25	42	390	5.3
2	Effelsberg	100	40	19	1.3
3	Westerbork		170	230	8.3
4	Cambridge	25	23	212	5.3
5	Jodrell Bank	76	55	48	6.7
6	Evpatoria	70	75	54	41.6
7	Bear Lakes	64	163	214	8.3
8	Knock	25	45	520	51.6
9	Bologna	32	100	582	33.3
10	Noto	32	100	784	30.0
11	Shanghai	25	80	2024	217.0
12	VLBA PT	25	30	276	18.0
13	VLBA NL	25	30	276	18.0
14	VLBA BR	25	30	276	18.0
15	VLBA OV	25	30	276	18.0
16	VLBA SC	25	30	276	18.0
17	VLBA HN	25	30	276	18.0
18	VLA 27	(130)	45	11	1.2

Table 2. Parameters of radio interferometers

Baseline*	$B \times 10^6\lambda$	δF, mJy	φ_f, mas
2–18	44	1.2	4.5
2–15	45	5	4.4
2–11	40	21	5.0
7–12	47	18	4.3
7–18	46	5	4.3
11–18	54	20	3.7
11–12	54	78	3.7
11–16	63	78	3.2
5–11	45	47	4.4
6–12	51	27	3.9
6–18	51	7	3.9
10–15	51	23	3.9
10–18	50	6	4.0

* Baselines correspond to antenna numbers in Table 1.

low frequencies. For the quasar 3C 345, the low-frequency core emission is heavily attenuated, while the bright, compact component corresponds to the nearby part of the jet. Its emission strongly "illuminates" the residual core emission, which complicates its study (Matveyenko *et al.* 1992, 1996). Thus, to investigate the fine structure of the core and the jet formation region requires observations over a wide radio spectral range with a high angular resolution and a high sensitivity in a wide dynamic range (~50 db). The optical depth and brightness temperature of the components increase with wavelength, but the angular resolution decreases.

An optimum spectral range is 6–18 cm for studies of the middle and extended structure and millimeter wavelengths for studies of the structure in the core region. A typical AGN object similar in properties to the quasar 3C 345 is the source 1803+784. It has a simple power-law spectrum $F \sim f^{-\alpha}$ with spectral index $\alpha = 0.26 \pm 0.18$ (Witzel 1986). Its radio flux density at 13 cm is $F \approx 3$ Jy and varies with time by ~1 Jy. The variability time scale at decimeter (13–20 cm) wavelengths is ~1.5 years (Aller *et al.* 1994; Naundorf *et al.* 1994). At centimeter (3.6–6 cm) wavelengths, the radio flux density exhibits rapid (intraday) variations by several percent (Aller *et al.* 1994). These features must show up in the object's fine structure. Here, our goal is to investigate the fine structure of the source 1803+784.

VLBI PARAMETERS AND OBSERVING TECHNIQUES

The development of very long baseline interferometry (VLBI) (Matveyenko *et al.* 1965) has made it possible to investigate the fine and hyperfine structure of compact radio sources. At present, virtually all large radio telescopes in the world are combined into a single global network. The object 1803+784 was observed at 18 cm on May 29, 1993, from 00^h00^m until 20^h58^m UT using a VLBI network composed of 18 antennas. Signals were recorded with MK-2 systems in the band $\Delta f = 2$ MHz, and a correlation analysis of the data was performed on a dedicated computer at the Californian Institute of Technology. Antenna locations and diameters, telescope noise temperatures T_{sys} (in K), F_{sys} (in Jy), as well as actual sensitivities δF_i are given in Table 1.

The VLBI network is an antenna array composed of n elements that form $N = n(n-1)/2$ radio interferometers. The sensitivity of a radio interferometer is equal to the geometric mean of the sensitivities of its constituent elements:

$$\delta F = b\sqrt{\delta F_1 \delta F_2}, \text{ Jy},$$

where b is the loss factor.

For two-level single-bit digital systems, the total loss factor determined by signal quantization and sampling is $b \approx 2.5$ (Thompson *et al.* 1989). The interferometer sensitivity also depends on the loss of signal coherence due to heterodyne instability and tropospheric, ionospheric, equipment, and other effects. At $\lambda = 18$ cm, the ionosphere limits the coherent signal integration time to 100–150 s, depending on time of the day and solar activity. In our case, the integration time was taken to be 60 s. Maximum sensitivities δF for a number of radio interferometers, which reach several mJy, are listed in Table 2. As we see from the table, fluctuation sensitivities of the instruments range from 1.2 mJy to several tens of mJy. The 100-m telescope in Effelsberg and the VLA, which is equivalent to a 130-m dish, have a maximum sensitivity. Also given here are their baselines B and fringe sizes φ.

The results of our correlation analysis of the observational data were mutually calibrated by the method of

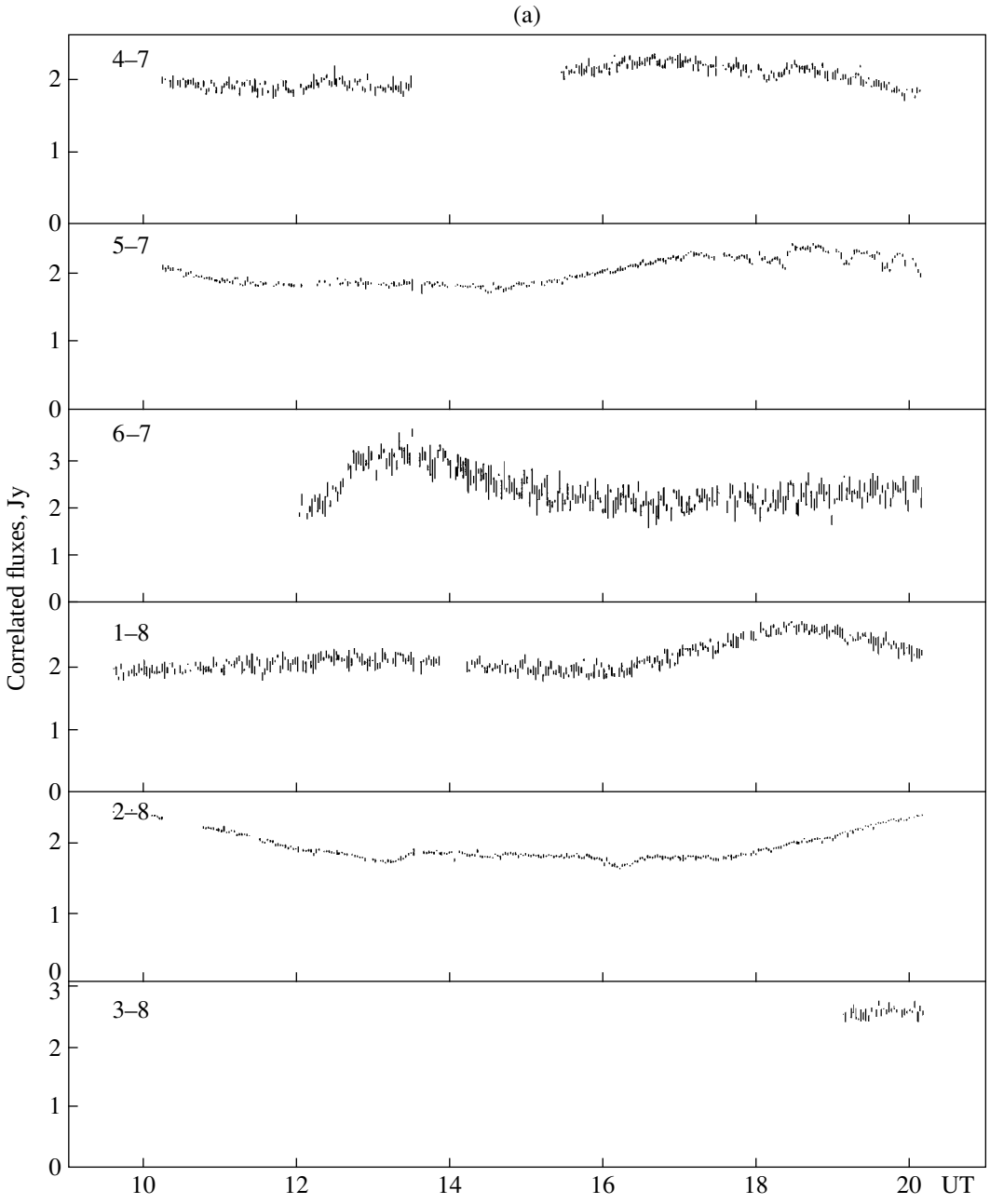

Fig. 1. (a) Correlated fluxes and (b) phases for the object 1803+784 obtained on several VLBI interferometers at $\lambda = 18$ cm (1993.41). Interferometer elements corresponds to numbers from Table 1.

closed phases and amplitudes (Cornell and Wilkinson 1981). These data in the form of plots of correlated fluxes F_{cor} and phases against time of observation t for several interferometers are shown in Figs. 1a and 1b. Figure 2 shows the correlated fluxes from the object 1803+784 obtained on all VLBI interferometers. As we see from Fig. 2, the correlated flux on long baselines ($\sim 62 \times 10^6 \lambda$) falls to $F_{cor} \approx 0.5$ Jy and corresponds to the emission from a compact structure. Based on these data, we constructed radio maps.

The spatial harmonics in the brightness distribution $T_b(x, y)$ of an object are given by the Fourier transform

$$S(u, v) = \iint T_b(x, y) \exp[j2\pi(Ux + Vy)]dxdy,$$

where U and V are the spatial harmonics. This transform is valid for objects whose brightness distribution can be represented as a set of incoherent point sources, as observed in the case of astronomical objects. The interferometer response corresponds to the spatial harmonic determined by the baseline projection onto the

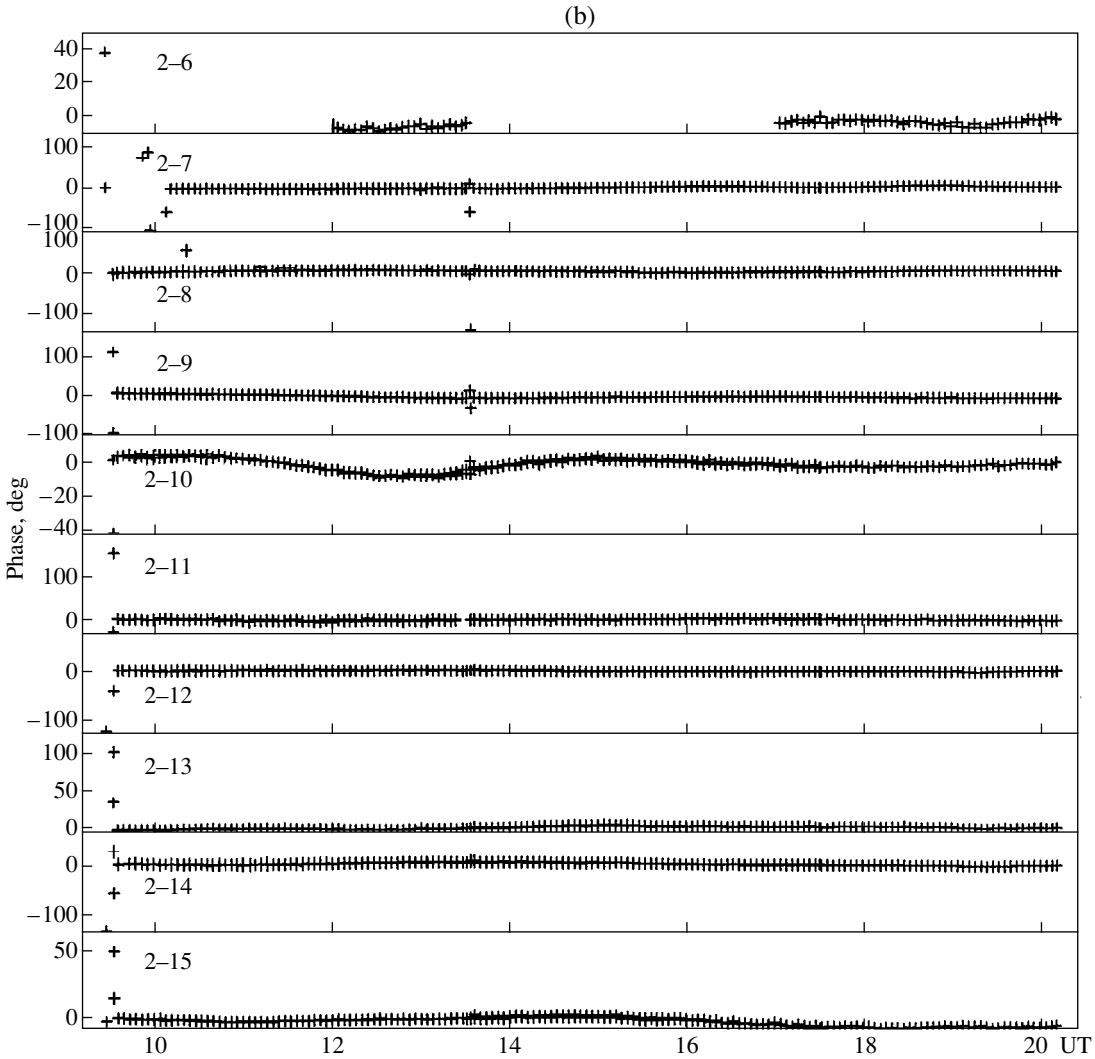

Fig. 1. (Contd.)

plane of the object under study, in wavelengths. Figure 3 shows the VLBI spatial frequency spectrum—the filling of the *UV* plane for the source 1803+784.

When the *UV* plane is completely filled, a $\sin(2\pi\xi U_{max})/(2\pi\xi U_{max})$ beam is formed. The level of the first sidelobe reaches 22% (Thompson *et al.* 1989). The beam FWHM is $0.705/B_{max}$. In our case, the maximum frequency is $80 \times 10^6\lambda$.

A synthesized beam is determined by the sum of harmonics (Meeks 1976)

$$P(x, y) = \frac{1}{N}\sum_{1}^{N} \cos 2\pi(U_i x + V_i y),$$

where N is the number of radio interferometers.

Figures 4a and 4b show sections $P(x)$ and $P(y)$ of the synthesized beam in the $U = 0$ and $V = 0$ principal planes. As we see from the figures, the FWHM of the main lobe is $P(Q_x) = 2.11$ mas and $P(Q_y) = 2.16$ mas. Incomplete filling of the *UV* plane, the "holes" at frequencies of $(18–27) \times 10^6\lambda$ and $(55–65) \times 10^6\lambda$, causes an increase in the level of the first sidelobes to 40%. The far sidelobes are bounded by the field of view. The VLBI field of view is determined by the correlation-zone width—the number of fringes which depends on signal reception band $m = f/\Delta f$. In our case, $m = 800$, corresponding a correlation-zone width of ~3″.

The derived brightness distribution of the object is distorted by the synthesized beam—a "dirty image." It can be corrected ("cleaned"). The cleaning accuracy depends on the accuracy of knowing the beam, which in many ways determines the dynamic range of the measurements. The beam is synthesized over the entire period of observations (24 hours). The temperature, weather conditions, atmospheric and ionospheric transparency, and visibility conditions for the source (elevation angle, parallactic angle, antenna polarization effects) vary during this period. This leads to amplitude

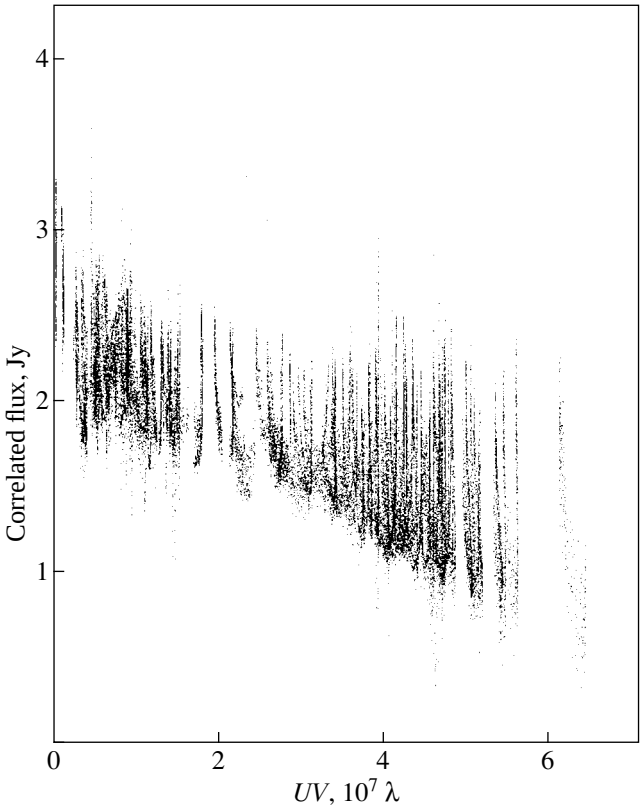

Fig. 2. Correlated fluxes from 1803+784 obtained on the global VLBI at λ = 18 cm (1993.41). The projected baselines are in 10^7 λ.

and phase errors and affects the accuracy of determining the synthesized beam, the level of its sidelobes, and, consequently, the dynamic range. If a bright compact object is present in the region under study, data calibration can be performed by using this reference source, which considerably reduces the measurement errors. However, the accuracy of the object's absolute position and of its brightness are determined by the accuracy of VLBI calibration based on reference objects. The VLBI dynamic range is equal to the maximum-to-minimum brightness ratio (Thompson *et al.* 1989). The lowest detectable brightness is determined by the instrument sensitivity and by the accuracy of compensating for the sidelobe level.

The "superresolution" of a radio interferometer makes it possible to measure sources of very small angular sizes and depends on fringe size φ_f and instrument sensitivity δF. The visibility functions of sources, $\gamma = F_{cor}/F_0$, with different brightness distributions, whose effective angular sizes do not exceed $\varphi_s \le 0.5\varphi_f$, are essentially identical, $\gamma \ge 0.4$. In this case, the baselines are $B/B_{0.5} \le 1.2$, where $B_{0.5}$ is the baseline for which $\gamma = 0.5$ (Meeks 1976). In order to establish the nature of the radio emission from a compact source, it will suffice to know its effective size. A Gaussian approximation of the radio brightness distribution is commonly used. In this case, the effective angular size of a source φ_s is

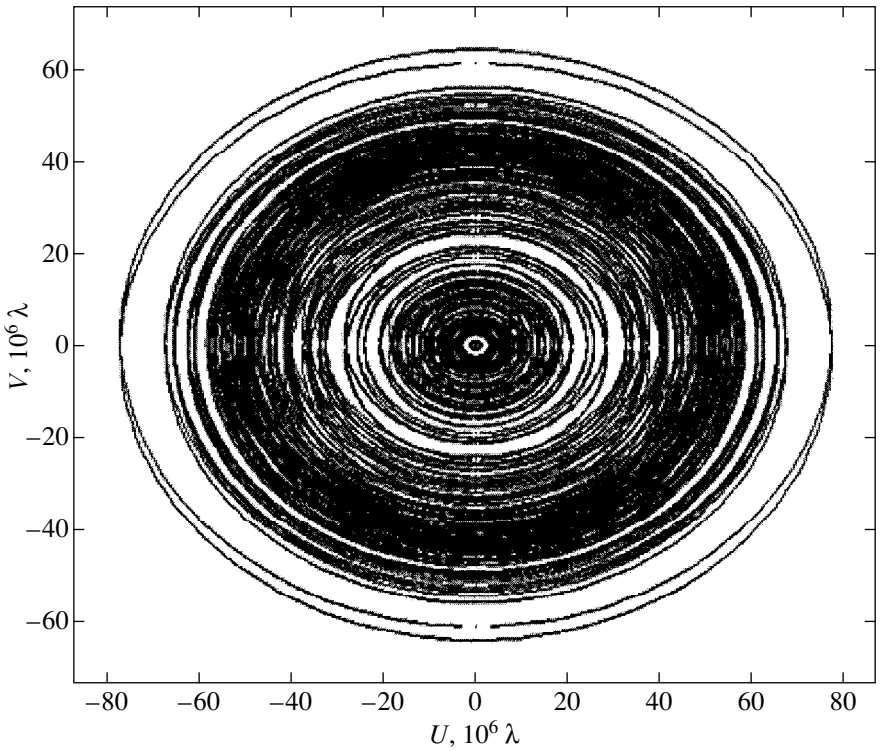

Fig. 3. Filling of the *UV* plane of the global VLBI at λ = 18 cm for 1803+784. The spatial frequencies (projected baselines) are in 10^6 λ.

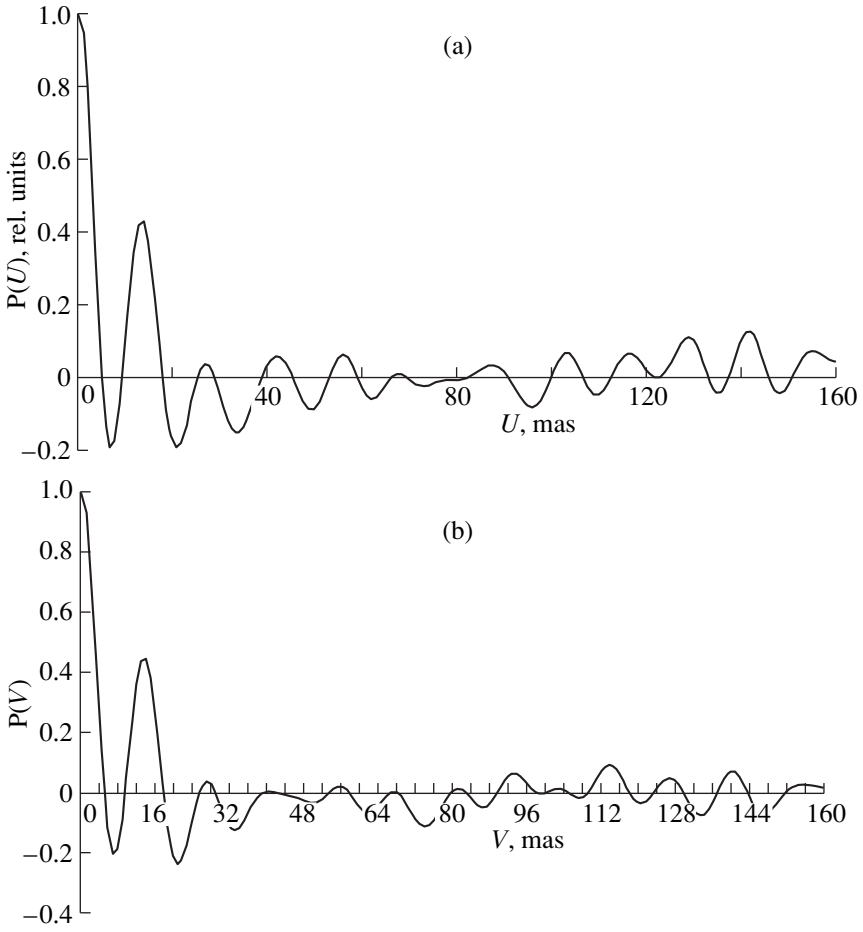

Fig. 4. Synthesized VLBI beam at λ = 18 cm in the principal (a) *U* and (b) *V* sections.

$$\varphi_s = \varphi_f\sqrt{|\ln\gamma|/3.35}.$$

The smallest detectable size of a source φ_s is determined by measurement errors, i.e., by the instrument sensitivity and its calibration accuracy. In our case, the interferometer sensitivities reach 2 mJy (Table 1). For a 10% accuracy of measuring the visibility function equal to $\gamma = 0.8$, the source size is $\varphi_s/\varphi_f = 0.25$ with a 20% error. On intercontinental baselines $B = (45–62) \times 10^6\lambda$ ($\varphi_f \approx 4$ mas), sources with angular sizes down to ~0.5 mas and radio flux densities of several tens of mJy can be measured.

The error in the relative positions of components also depends on signal-to-noise ratio (Meeks 1976) and is $F_{sys}/F_s\sqrt{2Bt}$; $\delta\varphi_s/\varphi_f = (1/2\pi)\delta F/F_s$ for a signal-to-noise ratio of 10 and reaches $\delta\varphi_s = 0.4$ mas in our case.

The expected minimum angular sizes of compact sources of synchrotron radiation Ω can be estimated from their peak brightness temperatures T_b and radio flux densities $F = 2kT_b\Omega/\lambda^2$. The limiting brightness temperature of a source of synchrotron radiation is determined by Compton backscattering and is $T_b \approx 10^{12}$ K (Kellermann and Pauliny-Toth 1969). The limiting angular size of a source at 18 cm is $\varphi_0 = 0.78F^{0.5}$ mas, where *F* is in Jy. The brightness of the compact source (Fig. 5a) is *B* = 1.129 Jy/beam (*Q* = 0.3 mas), and its limiting angular size is $\varphi_0 = 0.82$ mas.

On the other hand, the apparent angular sizes of sources are smeared because of scattering by interstellar inhomogeneities (Matveyenko 1978, 1984):

$$\varphi_{sc} \approx 10^{-3}\lambda^2|\sin b|^{-0.5} \text{ mas},$$

where *b* is the Galactic longitude of the object.

The coordinates of the object 1803+784 are $\alpha = 18^h03^m39^s.177$, $\delta = 78°27'54''.29$ (1950.0); they correspond to Galactic coordinates $l \sim 78°$ and $b \sim 30°$, and the scattering angle is $\varphi_{sc} \approx 0.46$ mas. Scattering increases the apparent angular size of the compact source in the Gaussian approximation to $\varphi_s = \sqrt{\varphi_0^2 + \varphi_{sc}^2}$ or $\varphi_s \approx 0.94$ mas, while its brightness temperature decreases to $T_b \approx 0.76 \times 10^{12}$ K.

Based on our observations, we constructed a hybrid map in the form of a set of point sources. In order not

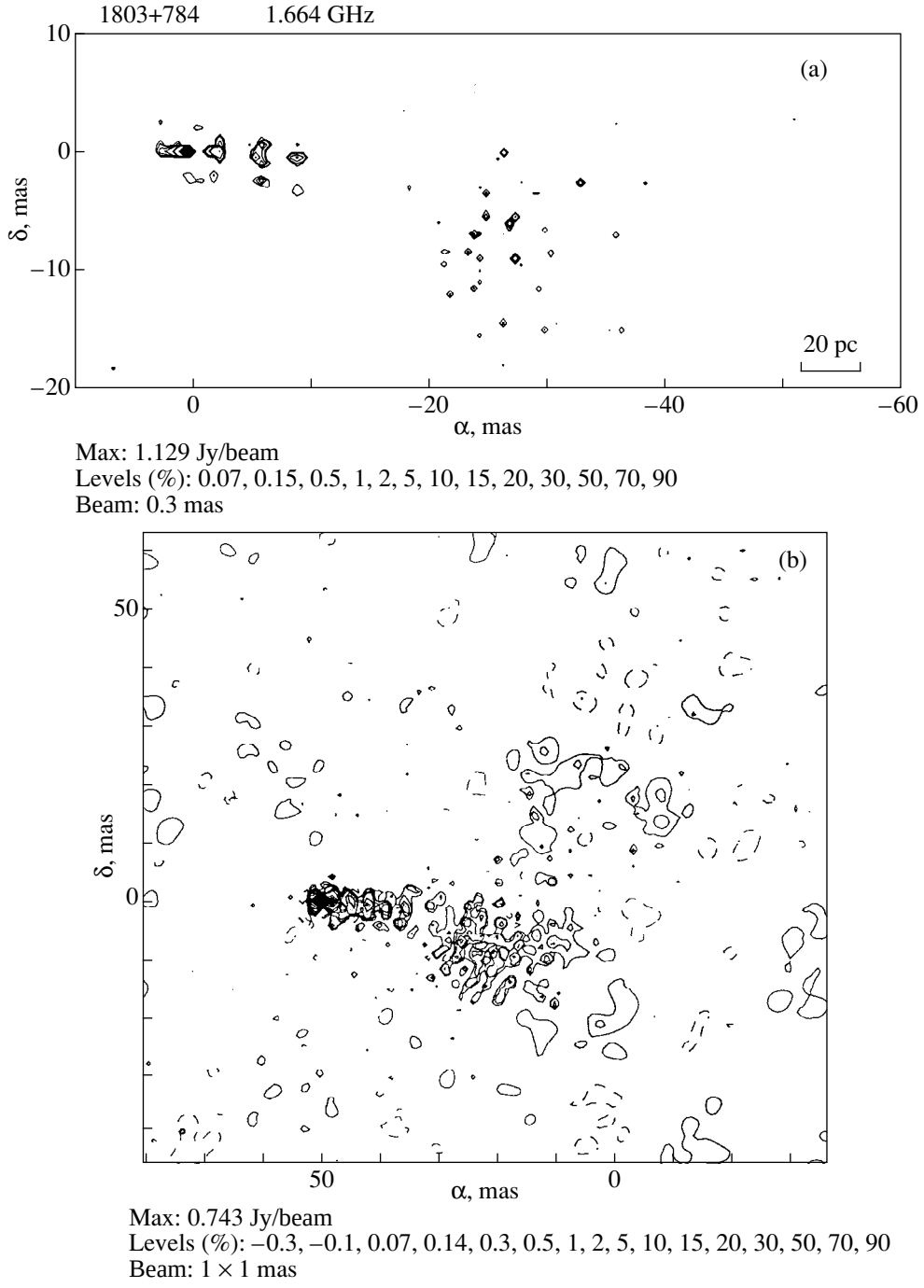

Fig. 5. Brightness distribution of 1803+784 with angular resolutions of (a) 0.3, (b) 1, (c) 2, (d) 3.8, (e) 6, and (f) 0.3 × 3 mas.

to "limit" the angular resolution, the point sizes were taken to be 0.3 mas. The brightnesses of the point sources were chosen in such a way that the rms deviation of the Fourier response of their collection differed minimally from the measured correlated fluxes and phases. Figure 5a shows an image of the object under study with an angular resolution of 0.3 mas. This image corresponds to the observational data. The peak brightness is 1.129 Jy/beam. Smoothing a "point" image with a Gaussian beam reduces the angular resolution, but increases the accuracy of determining extended structures. Figure 5b shows the brightness distribution smoothed with a 1-mas beam; in Figs. 5c–5e, it is smoothed with 2-, 3.8-, and 6-mas beams, respectively. Extended structures with brightness $B = 0.7 \times 1.38$ mJy/beam, or 32 db, are distinguishable in the maps. A comparison of maps with different resolutions extends the dynamic range to 56 db.

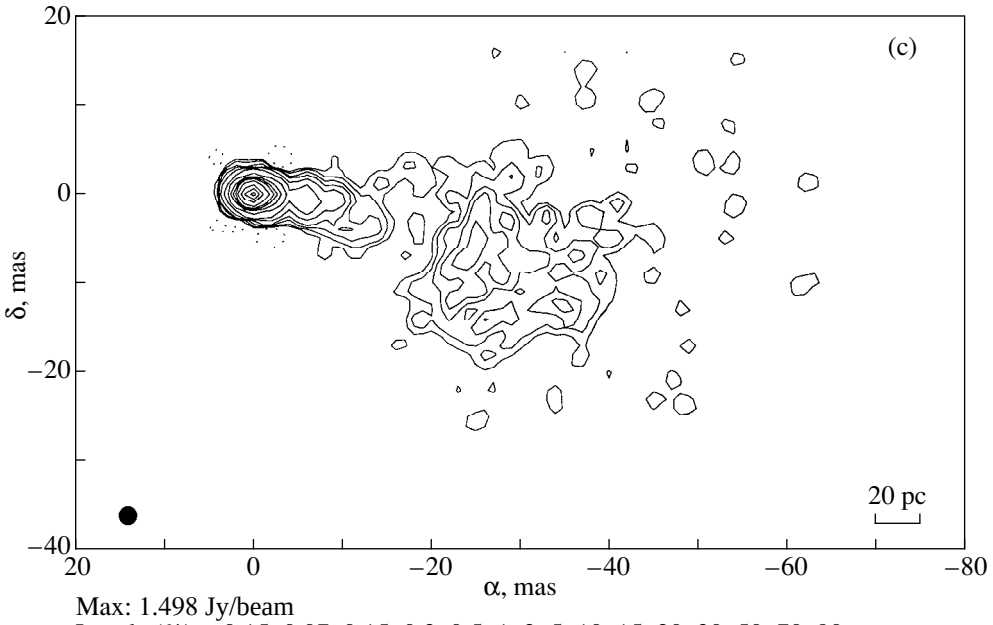

Max: 1.498 Jy/beam
Levels (%): –0.15, 0.07, 0.15, 0.3, 0.5, 1, 2, 5, 10, 15, 20, 30, 50, 70, 90
Beam: 2 mas

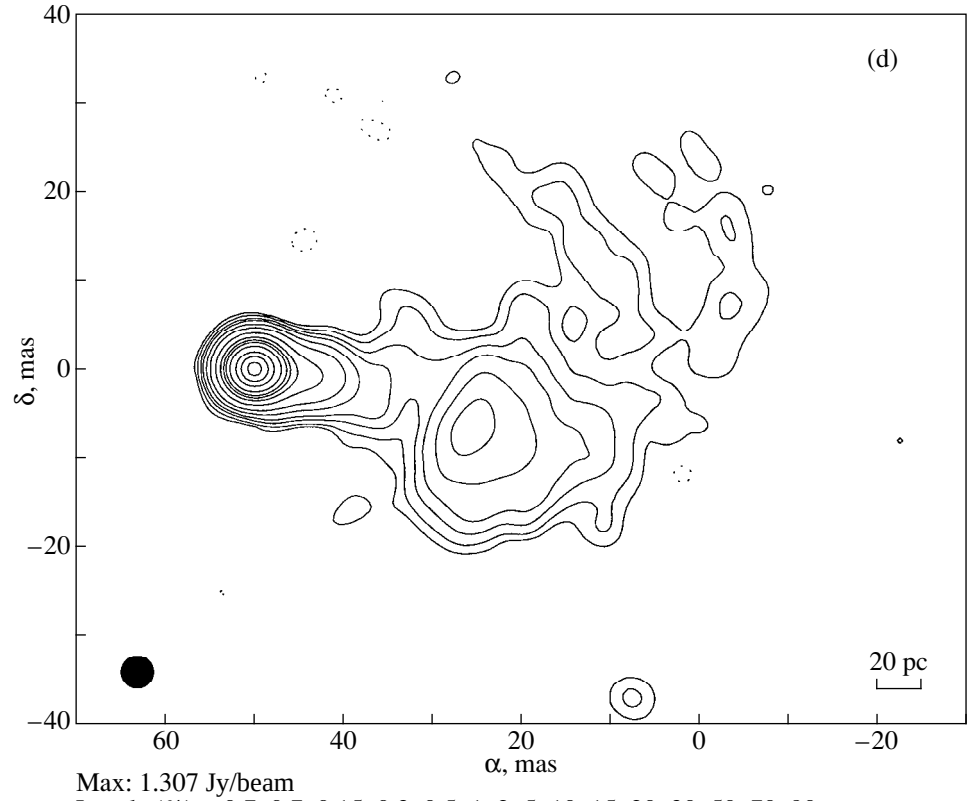

Max: 1.307 Jy/beam
Levels (%): –0.7, 0.7, 0.15, 0.3, 0.5, 1, 2, 5, 10, 15, 20, 30, 50, 70, 90
Beam: 3.80 mas

Fig. 5. (Contd.)

RESULTS AND INTERPRETATION OF OBSERVATIONAL DATA

1803+784 is a BL Lac object, but it is more similar in properties to the well-known quasar 3C 345 (Lawrence *et al.* 1986). Its redshift is $z = 0.68$ (Krichbaum and Witzel 1989). The photometric distance to the object is given by $D_L = c[z + 0.5(1 - q_0)z^2]$ Mpc, and the angular size as a function of its physical size l is

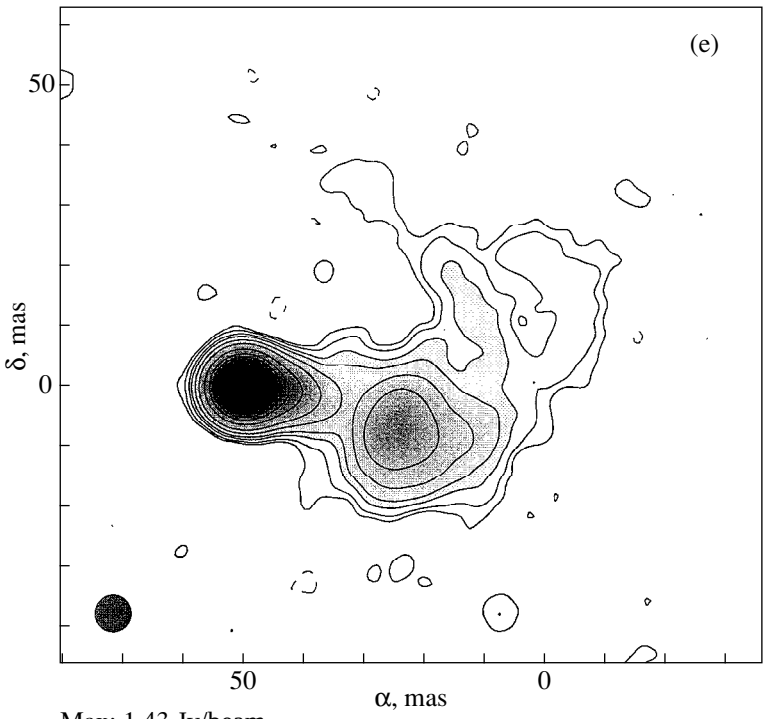

Max: 1.43 Jy/beam
Levels (%): –0.1, 0.07, 0.14, 0.3, 0.5, 1, 2, 5, 10, 15, 20, 30, 50, 70, 90
Beam: 6 × 6 mas

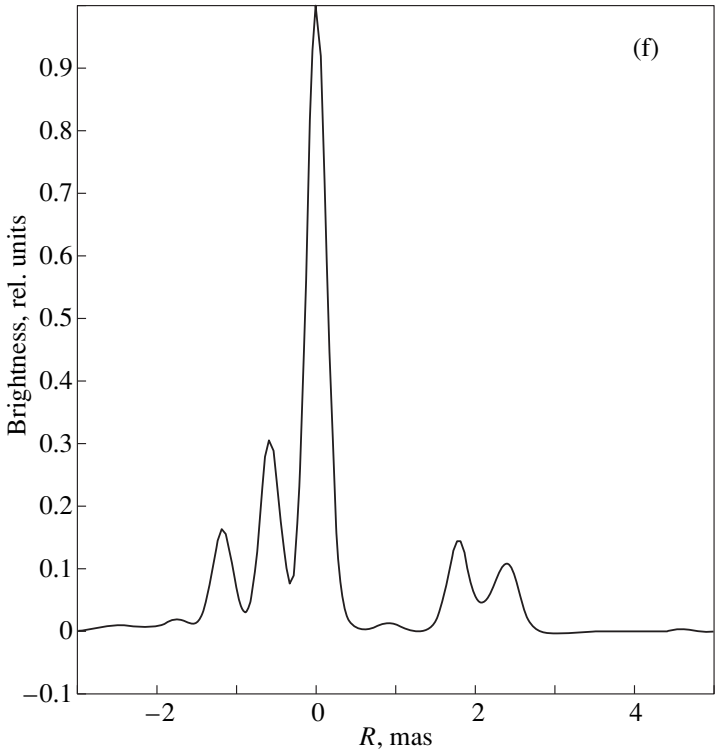

Fig. 5. (Contd.)

$$Q = \frac{l(1+z)^2}{D_L} \text{ rad}.$$

For the Hubble constant $H_0 = 100$ km s^{-1} Mpc^{-1} and the deceleration parameter $q_0 = 0.5$, the distance to 1803+784 is $D_L = 2700$ Mpc, and ~5 pc corresponds to an angular distance of 1 mas.

The core and the jet are distinguishable in the object's structure at millimeter wavelengths. The jet exhibits separate bright components, which show up

Table 3. Optical depths of the cocoon wall

Distance R, mas	0	0.79	1.35	1.92	2.54
A/A_{max}	0.008	0.02	0.17	0.31	1.0
$\tau = \ln A/A_{max}$	4.79	3.9	1.77	1.17	0.0
$\tau + 0.5$	5.29	4.4	2.27	1.67	0.5
τ_{calc}	5.5	3.92	2.80	1.66	0.42

most clearly at high frequencies (Schalinski *et al.* 1987; Krichbaum and Witzel 1989; Charlot 1990). Compact components are occasionally ejected from the core. Their apparent velocities reach $v = (7 \pm 5)$ (Krichbaum and Witzel 1989). The ejection direction was $X = -111°$ at $f = 43$ GHz in 1989.19 and lay in the range from –68° (1988.16) to –90° (1990.87–1991.86) at a frequency of 22 GHz. The distribution of compact components and their trajectories correspond to a divergent conical helix traceable to distances of ~8 mas (Fig. 6) (Krichbaum and Witzel 1990; Krichbaum *et al.* 1994; Britzen *et al.* 1994). The helix diameter linearly increases, reaching 0.9–1.4 mas at a distance of 2.3 mas from the core. The helix cone angle is 22°–34°. Extrapolating these data to the cone base, we can determine the injector position. It is located at (0.4–0.5) mas from the bright compact component in Fig. 6. The helix pitch T increases exponentially and is 1.08 mas at $R = 8$ mas, corresponding to $T = 0.236(R_0 + R)^{0.7}$. The axis at the helix cone base is directed at –90°, and the cone angle is 34° (Krichbaum *et al.* 1992). The observed change in the ejection direction of the components and their helical trajectories can be explained by precession of the injector axis around the $X = -90°$ direction, with the precession angle being ~30°.

Observations at 43 GHz revealed compact components in the jet at 0.3, 0.5, 1.3, and 1.6 mas from the core (epoch 1990). To within the measurement errors, the compact sources at distances of 0.4, 0.8, 1.3, and 1.9 mas at 22 GHz correspond to them. In addition, there are two components at 2.4 and 2.6 mas from the core. At 18 cm, compact regions are seen at 4.5 and 25 mas from the injector. The brightness temperatures of the components are modest and rapidly decrease with increasing distance from the core, suggesting that they are optically thin (Schalinski *et al.* 1987; Krichbaum and Witzel 1989; Charlot 1990).

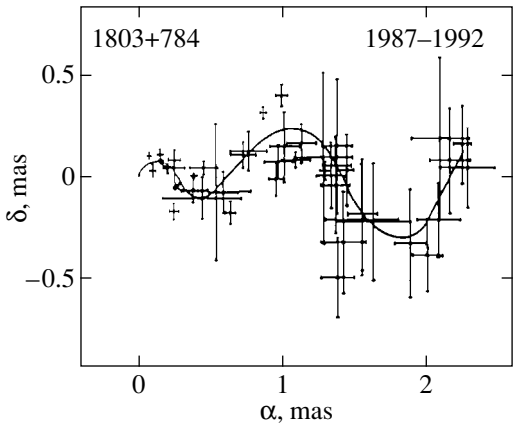

Fig. 6. Trajectories of the components (Krichbaum *et al.* 1994).

The jet extends to 30 mas, or 150 pc, at decimeter wavelengths ($\lambda = 13, 18$ cm) and is oriented at an angle of –100° (Krichbaum *et al.* 1992; Schalinski *et al.* 1992). According to our 18-cm data (Fig. 5a), individual structures are concentrated within a cone with an angle of ~23°. This structure can be represented as a relativistic plasma flow. The flow is split in two parts. Its near part immediately adjacent to the injector is ~18 mas (or 85 pc) in extent, while its far part lies in the range from 22 to 43 mas and is 205 pc in extent. The jet splitting in two components separated by ~20 mas in the –100° direction was also noted by Waak *et al.* (1987). The observed break of the jet may result from a reduction in injector activity. The jet axis is curved. As we see from Figs. 5a and 5b, the jet is oriented at ~ –90° within up to 5 mas from the injector and changes to –100° further out at 10 mas. This is probably because the injector orientation changes due to long-period precession of its rotation axis.

The 18-cm emission from the injector region is heavily attenuated by an absorbing screen. A brightness peak is observed outside this screen, which is followed by a decline. At distances of 5 and 25–30 mas, the components are not bright, because they are optically thin, and their brightness temperatures are $T_b = 3 \times 10^{11}$ and 0.8×10^{11} K, respectively.

A certain relationship of the jet structural features at 18 cm (Figs. 5a and 5b) with the results of high-frequency measurements shows up. The jet cone essentially matches in angle (~23°) and orientation (~ –90°) the conical helix. Compact knots of relativistic plasma move along the magnetic flux tube. This, in turn, suggests a helical jet structure, in any case, in its initial part. A "steady" flow of relativistic plasma must move along the same magnetic flux tube as do individual clouds, forming the helical jet structure. The VLBI angular resolution and dynamic range at 18 cm turned out to be insufficient to determine the hyperfine helical structure of the jet. However, such a structure shows up at 6 cm (Gabuzda *et al.* 1999).

Let us consider the jet structure in the injector region. Figure 5f shows the brightness distribution along the jet axis obtained by smoothing the point image in Fig. 5a with a 0.3×3.0-mas knife-edge beam perpendicular to the jet axis. Relative peak brightnesses of the point sources A/A_{max} along the jet and their positions ΔR are given in Table 3. The brightness increases with distance from the injector virtually exponentially. The relativistic plasma flow must be optically thick in the jet region under consideration, and, accordingly, its brightness temperature is close to the Compton limit. At the same time, the observed increase in brightness

with distance from the injector can be explained by transparency variations in the ambient ionized medium.

The central regions of AGNs, including the object 1803+784, are surrounded by a fairly dense ionized medium observable in emission lines, and its electron temperature is $T_e \approx 10^4$ K. The electron density in the narrow emission line region is $N_e = 10^{(4-6)}$ cm^{-3}. The region for 3C 345, a typical quasar, reaches 30 pc in size. Dense clouds of ionized gas with $N_e \approx 10^{10}$ cm^{-3} emitting broad lines are embedded in this region (Netzer 1987). Dense clouds fill 10–20% of the space under consideration.

The $e^{-\tau}$ absorption of an ionized medium is determined by its optical depth τ (Kaplan and Pikel'ner 1979):

$$\tau = 0.08 T_e^{-1.35} (1+z)^{-2.1} f^{-2.1} \int N_e^2(l)\, dl,$$

where f is the frequency in GHz, $T_e = 2 \times 10^4$ is the gas electron temperature in K, l is the layer thickness in pc, and $N_e(l)$ is the electron density distribution in cm^{-3}. The optical depth at $\lambda = 18$ cm is

$$\tau = 1.56 \times 10^{-8} ME,$$

where $ME = \int N_e^2\, dl$ cm^{-6} pc is the emission measure.

Calculated optical depths of the absorbing screen $\tau = \ln(A_R/A_{max})$ are given in Table 3. At maximum emission $R_0 = 2.75$ mas, the peak brightness corresponds to a brightness temperature close to the Compton limit. We take the absorption at this point to be 1.5, which corresponds to optical depth $\tau_{R_0} = 0.5$. Optical depths corrected for this "initial" absorption are given in the next row of Table 3. Our data can be represented as a linear dependence (dashed line in Fig. 7) or $\tau = 5.5[1 - \Delta R/R_0]$.

In practice, the optical depth decreases more smoothly, as indicated by the solid line in Fig. 7:

$$\tau = 6(1 - R/R_0)^{-3},$$

where $R_0 = 3$ mas. Let us consider the absorption in the immediate vicinity of the injector, $\Delta R \approx 0.5$ mas. The screen optical depth in the linear approximation is $\tau_{0(18)} = 4.5$, corresponding to an absorption of ~20 db at 18 cm. At higher frequencies, for example, at 6 cm, the optical depth is $\tau_{0(6)} = 0.45$, and the absorption is a mere 1.5, while at 22 GHz, the screen becomes virtually completely transparent, $\tau_{0(1.3)} \approx 0.03$.

LOW-FREQUENCY RADIO VARIABILITY

The object 1803+784 is a variable source; its radio flux density at 13 cm varies by ~30%. The variability time scale in the wavelength range 13–20 cm is $t \approx 1.5$–2 years (Aller *et al.* 1994; Naundorf *et al.* 1994). Such large flux variations in such a short time can be determined only by the brightest compact part of the source. This source corresponds to the jet part extending outside the screen edge, where its transparency is fairly

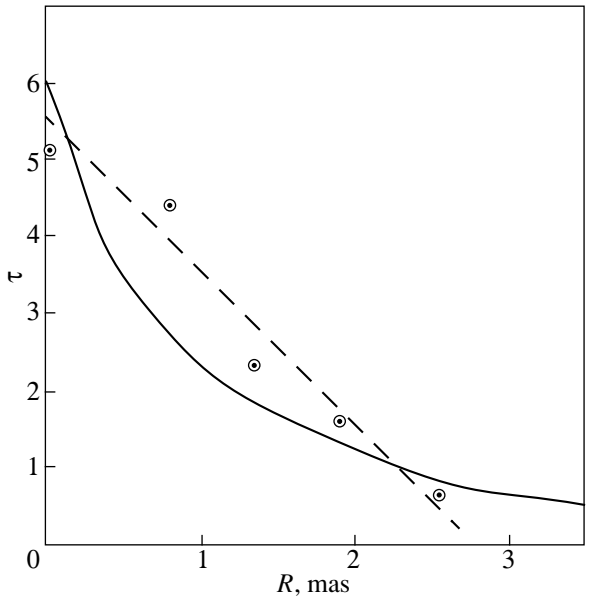

Fig. 7. Variations of the absorbing-screen optical depth along the jet axis. The linear and exponential decreases are indicated by the dashed and solid line, respectively.

enough (Figs. 5a and 5f). Variations in ultraviolet radiation change the screen transparency and, accordingly, the visibility of the bright low-frequency region. The bright compact region is at $R \approx 3$ mas from the injector.

Let us estimate the screen parameters. We optimize the parameters of the screen in terms of the observed variability and assume its optical depth in the region of maximum emission to be $\tau \approx 0.7$, corresponding to an absorption of ~2 at 18 cm. Based on this optical depth, we find the emission measure to be $ME \approx 10^8$ cm^{-6} pc. In order to produce the observed changes in screen transparency by 30%, it will suffice to change the optical depth by $\Delta\tau \approx 0.3$ (±20%). The variability time scale of the radio emission is $t = 1.5$–2.0 years, or ~1 year in the source's frame. It depends not only on the time scale of variations in ionizing radiation, but also on the recombination time. The recombination time is $t_{rec} \approx 10^5/N_e$; hence, the electron density in the screen is $N_e \approx 10^5$ cm^{-3}. Given the screen absorption and the electron density, the screen thickness is $l \le 10^{-2}$ pc. A similar value is obtained from the mean free path of ultraviolet photons. Such a small screen thickness does not limit the time scale of the low-frequency variability, $l/c < t$. This screen is the cocoon wall enveloping the jet.

Rapid radio variability is observed at high frequencies ($\lambda = 3.6$–6 cm). The variability time scale is about 12 days at $\lambda = 6$ cm and 4 days at $\lambda = 3.6$ cm (Aller *et al.* 1994; Naundorf *et al.* 1994). The high-frequency radio emission is determined by the injector region. This region is blocked by the dense clouds responsible for broad emission lines. The electron density in them reaches $N_e \approx 10^{10}$ cm^{-3}. The rapid high-frequency variability may be associated with these embedded clouds.

At the same time, the observed rapid high-frequency radio variability for a transparent screen can be produced by the interaction of the relativistic plasma flow with the cocoon wall—plasma emission mechanisms. In this case, the emission of not only relativistic electrons but also of relativistic ions (coherent emission) can be observed. Under these extreme injector operation conditions, the masing mechanism—an enhancement of all types of generated emissions in the injector—is also possible (Kaplan and Pikel'ner 1979; Bandford 1991).

THE AMBIENT MEDIUM–SCREEN

As was noted above, the central regions of AGNs are surrounded by an ionized medium visible in emission lines. The ultraviolet radiation from the injector ionizes the ambient gas. The medium is inhomogeneous. The broad-line emission region consists of dense clouds of ionized gas distributed in a medium of lower density. Dense clouds generally constitute only a small part of the total volume. The medium for the object 1803+784 is ~8 mas in extent. The observed Balmer-line width varies in the range from several days to several years for different objects (Pronik 1972).

According to black-body models (Shakura and Sunyaev 1973; Begelman *et al.* 1984; Ustyugova *et al.* 2000; Bisnovatyĭ-Kogan *et al.* 1969), matter is concentrated in the azimuthal plane; it falls to the accretion disk, accelerated, and is ejected at a relativistic velocity along the rotation axis in the form of relativistic plasma. The generated magnetic field self-focuses the flow into a narrow jet. Precession of the rotation axis produces a helical structure of the magnetic flux tube and, accordingly, a jet structure in the form of a divergent conical helix, which determines the trajectories of plasmoids in the object 1803+784.

The flow of relativistic particles draws the ambient medium apart to form a thin cocoon wall (Begelman *et al.* 1984). The observed curvature of the jet axis is determined by long-period precession of the jet rotation axis. In this case, the injector itself is a compact source of synchrotron radiation (core). Peculiarities of the core emission reflect the injector operation mode and the high-frequency radio variability, while the cocoon-wall transparency determines the visibility of the low-frequency emission. Depending on the observing direction, transparency of the medium concentrated in the azimuthal plane can also have an effect.

The cocoon-wall thickness and the electron density are determined by an equilibrium between the thermal and relativistic plasma pressures. The pressure in the jet is proportional to the density squared, $P_j \sim \rho^2$, and decreases with increasing distance from the injector as $\sim R^{-2}$ (Begelman *et al.* 1984). In this case, $N_e \sim R^{-2}$ and the wall thickness is $l \sim R$. The total number of electrons in the wall on the line of sight $N_e l$ changes more rapidly than R^{-1}, but more slowly than R^{-2}. The wall transparency is determined by the emission measure $ME = N_e^2 l$, which changes as $\sim R^{-3}$.

POLARIZATION OF RADIO EMISSION

VLA studies of 1803+784 with a modest angular resolution of ~1″ at six frequencies in the wavelength range 18–21 cm show that its emission is linearly polarized and oriented at $X = 51°$. Its orientation with respect to the jet is $\Delta X = 40°$. The rotation measure is $RM = -62 \pm 1$ rad m^{-2}, and the degree of polarization is 3.9% and does not vary within the entire band analyzed. This suggests that the observed rotation measure is determined by the external medium. If thermal electrons were distributed in the emitting relativistic plasma, then the degree of polarization would change by a factor of 5 for the above *RM* (Wrobel *et al.* 1988). Besides, the presence of thermal electrons would lead to catastrophic losses of synchrotron radiation (Razin 1958). The external medium can be the Galactic interstellar medium, whose effect determines the rotation of the polarization plane, but changes its level only slightly. Simultaneous observations of nearby sources ($l = 75°$–$115°$ and $b = (20°$–$50°)$) indicate that the rotation measure *RM* for 1803+784 ($l = 78°$, $b = 30°$) is opposite in sign to *RM* for the nearby objects 1823+568 ($RM = +33$ rad m^{-2}) and 1928+738, 1807+698, 1749+701 ($RM = +31$ rad m^{-2}) (Wrobel *et al.* 1988). Similar (in magnitude and sign) *RM* for the surrounding objects suggest that the mean $RM \approx 32$ rad m^{-2} corresponds to the rotation measure in the Galaxy. In this case, the rotation measure in the object 1803+784 itself is $RM = -94$ rad m^{-2}.

High-angular-resolution polarization VLBI observations at $\lambda = 18$ cm revealed two regions in the jet with orthogonal polarization planes, $\Delta X = 90°$. The separation between the components is ~4 mas. The polarization plane of the bright compact region (core) is oriented at $X = 0°$ (S.E. Aaron, personal communication). In this case, the results of VLA measurements (the polarization plane is oriented at $X = 51°$) correspond to a vectorial sum of the polarizations of both regions, and the core-to-jet polarization ratio is 0.8. According to our 18-cm data, the emission is determined by a compact region—the nearby part of the jet at $R \approx 3$ mas. Accordingly, the VLA total (including the interstellar medium) rotation measure, $RM = -62$ rad m^{-2}, essentially refers to this region of the source. The rotation of the polarization plane is $X = RM\lambda^2$; it is $X = -2$ rad ($-114°$) at 18 cm. Thus, the orientation of the polarization plane for the compact source itself corrected for rotation is $X = -114°$, i.e., virtually coincides with the jet orientation. The observed change of the polarization plane in the distant region by 90° can be explained by a change in rotation measure by $\Delta RM = \Delta X\lambda^{-2}$, or 48.7 rad m^{-2}. Thus, $RM = -62$ (-94) rad m^{-2} at the location of the brightest component and $RM = -13.3$ (-45.3) rad m^{-2} at

~4 mas from it. The core lies at 2.7 mas from the injector; in this case, $RM \approx -460\ R^{-1.8}$ rad m^{-2}.

Studies at $\lambda = 3.6$ cm show that the core emission has a polarization of 15–20%, and that the polarization plane is oriented at $X = 90°$ (Gabuzda and Cawthorne 1992). The bright compact component at 3.6 cm lies in the immediate vicinity of the injector, whose angular distance is assumed to be $R \approx 0.5$ mas. Extrapolating the above dependence $RM \approx -460\ R^{-1.8}$ rad m^{-2} to this distance yields $RM = -1600$ rad m^{-2} and $X \approx -2$ rad at 3.6 cm. The orientation of the polarization plane corrected for rotation is $X = -150°$ and essentially coincides with the jet direction.

As we see from the above data, the components' polarization P and its position angle X varies with distance R from the injector and with wavelength (Table 4). These variations can be attributed both to variations in screen rotation measure and in source optical depth. The polarization parameters of a synchrotron radiation source with an energy distribution of relativistic electrons with spectral index γ depend on optical depth. The degree of polarization of an optically thick source is $P(\gamma) = 3/(6\gamma + 13)$, and its plane is parallel to the magnetic field. $P = 10\%$ for typical sources. For optically thin sources, $P(\gamma) = (3\gamma + 3)/(3\gamma + 7)$. The degree of polarization for typical sources is $P = 70\%$, and its plane is perpendicular to the magnetic field (Kellermann 1974).

The optical depth of the compact components under consideration decreases with increasing frequency and distance from the injector. Accordingly, the degree of polarization must increase. The core polarization at 3.6 cm is $P = 20\%$; i.e., its optical depth is fairly small. This is also suggested by the observed orientation of the polarization plane, which is virtually parallel to the magnetic field. The magnetic field is assumed to be parallel to the jet. The bright compact component is optically thick at low frequencies ($\lambda = 18$ cm), and the degree of polarization decreases to 3.9%, with its plane being parallel to the jet (magnetic field).

Let us consider the possible effect of rotation measure on the measured degree of polarization. The polarization is $P = P_0 \sin(2X\Delta f/f)/2X\Delta f/f$, where $X = RM\lambda^2$ (in rad). The degree of polarization depends on relative band $\Delta f/f$ of the received signal and on rotation measure RM. For $RM = -62$ rad m^{-2} and $\Delta f \approx 30$ MHz at 18 cm, the polarization decreases by no more than 1%. Let us estimate the magnetic-field strength. The rotation measure is $RM = 8.1 \times 10^5 \int N_e B_\parallel dl$ rad m^{-2}. According to our previous estimates, the electron density is $N_e = 10^5$ cm^{-3}, and the cocoon wall thickness is $l = 0.01$ pc in the compact-component region at 18 cm. Accordingly, the magnetic-field strength is $B_\parallel \approx 0.5$ μG. The magnetic field, electron density, and screen thickness vary with distance from the injector as $B_\parallel \sim R^{-2}$, $N_e \sim R^{-2}$, and $l \sim R$, respectively. Thus, the rotation measure is $RM \sim R^{-3}$.

Table 4. Polarization parameters for the components

λ, cm / Parameter	Optical	3.6	6.0				13	20
R, mas	0	0.5	0.4	0.9	1.8	2.3	2.5	3.0
$-X$, deg	84	90	50	63	103	110	7.5	129
P, %	35	20	3	20	5	8	5	3.9
RM, rad m^{-2}	–	–	–85				–61	–62
References	[11]	[9]	[10]				[1]	[42]

CONCLUSION

We have investigated the fine structure of the AGN object 1803+784 at 18 cm with a high angular resolution over a wide dynamic range. A bright compact component and a jet were identified.

The object's central part is surrounded by an ionized medium concentrated in the azimuthal plane. The core and the jet were shown to be enveloped by a thin layer of thermal plasma like a cocoon.

The core is an injector of relativistic particles. Its radio emission at 18 cm is heavily attenuated by absorption in the screen, which exceeds 25 db. The emission measure is $ME = 10^8$ cm^{-6} pc. The screen transparency increases with frequency as $\sim f^{-2.1}$ and with distance from the injector as $ME \sim R^{-3}$. The screen is virtually transparent at millimeter wavelengths.

The bright compact component at 18 cm lies at $R \approx 3$ mas from the core and is the nearby part of the jet extending outside the dense part of the absorbing screen. The source's effective size is ~1 mas, and its brightness temperature is $T_b \approx 10^{12}$ K.

The thermal electron density in the screen near the emission peak reaches $N_e \approx 10^5$ cm^{-3}, and the wall thickness is ~10^{-3} pc. Ultraviolet radiation changes the screen transparency, causing low-frequency radio variability.

The polarization plane is parallel to the jet (magnetic field). The rotation measure in the cocoon wall varies as $RM \sim R^{-3}$. The longitudinal magnetic field in the screen wall at $R \sim 3$ mas from the injector is ~0.1 μG.

The compact components move along a trajectory in the shape of a conical divergent helix. The jet is a flow of particles distributed within a cone whose angle matches the angle of the conical helical trajectory, suggesting a helical jet structure. The jet helical structure and the jet-axis curvature are determined by rapid and long-period precession of the rotation axis, respectively.

ACKNOWLEDGMENTS

One of us (L.I.M.) wishes to thank the Max-Planck-Institut für Radioastronomie, the Joint Institute for Radio Astronomy, the RFBR, NWO, and INTAS Foundations for support. We are also grateful to K.M. Zakharin for help in preparing the article.

REFERENCES

1. M. E. Aller, H. D. Aller, and P. A. Hughes, in *Proceedings of a Workshop on Compact Extragalactic Radio Sources, Socorro, 1994*, Ed. by J. A. Zensus and K. I. Kellermann, p. 185.
2. G. Bandford, in *Extragalactic Radio Sources—from Beams to Jets*, Ed. by J. Roland, H. Sol, and G. Pelletier (Cambridge Univ. Press, Cambridge, 1991), p. 85.
3. M. C. Begelman, R. D. Blanford, and M. J. Rees, Rev. Mod. Phys. **56**, 255 (1984).
4. G. S. Bisnovatyĭ-Kogan, B. M. Komberg, and A. M. Fridman, Astron. Zh. **46**, 465 (1969) [Sov. Astron. **13**, 369 (1969)].
5. S. Britzen, T. P. Krichbaum, W. Steffen, *et al.*, in *Proceedings of a Workshop on Compact Extragalactic Radio Sources, Socorro, 1994*, Ed. by J. A. Zensus and K. I. Kellermann, p. 251.
6. P. Charlot, Astron. Astrophys. **229**, 51 (1990).
7. T. J. Cornwell and P. N. Wilkinson, Mon. Not. R. Astron. Soc. **196**, 1067 (1981).
8. H. Falcke, M. A. Malkan, and P. L. Biermann, Astron. Astrophys. **298**, 375 (1995).
9. D. C. Gabuzda and T. V. Cawthorne, in *Proceedings of the Nuffield Radio Astronomy Laboratories' Conference on Sub-arcsecond Radio Astronomy*, Ed. by R. J. Davis and R. S. Booth (Cambridge Univ. Press, Cambridge, 1992), p. 211.
10. D. C. Gabuzda, A. B. Pushkarev, and T. V. Cawthorne, Mon. Not. R. Astron. Soc. **307**, 725 (1999).
11. C. Impey, in *Proceedings of a Workshop on Superluminal Radio Sources, 1986*, Ed. by J. A. Zensus and T. J. Pearson, p. 233.
12. S. A. Kaplan and S. B. Pikel'ner, *Physics of the Interstellar Medium* (Nauka, Moscow, 1979), p. 281.
13. K. I. Kellermann, in *Galaxy and Extra-Galaxy Radio Astronomy*, Ed. by G. L. Verschuur and K. I. Kellermann (Springer-Verlag, Berlin, 1974), p. 346.
14. K. I. Kellermann and I. I. K. Pauliny-Toth, Astrophys. J., Lett. Ed. **155**, L31 (1969).
15. K. I. Kellermann and I. I. K. Pauliny-Toth, Annu. Rev. Astron. Astrophys. **19**, 373 (1981).
16. K. I. Kellermann, R. S. Vermeulen, J. A. Zensus, and M. H. Cohen, Astron. J. **115**, 1295 (1998).
17. T. P. Krichbaum and A. Witzel, Japan 1989 Dec., Frontier VLBI, p. 297.
18. T. P. Krichbaum, A. Witzel, K. J. Standke, *et al.*, in *Proceedings of a Workshop on Compact Extragalactic Radio Sources, Socorro, 1986*, Ed. by J. A. Zensus and K. I. Kellermann, p. 260.
19. T. P. Krichbaum, A. Witzel, D. A. Graham, *et al.*, in *Sub-arcsecond Radio Astronomy*, Ed. by R. J. Davis and R. S. Booth (Cambridge Univ. Press, Cambridge, 1992), p. 181.
20. C. R. Lawrence, A. C. S. Readhead, T. J. Pearson, and S. C. Unwin, *Proceedings of a Workshop on Superluminal Radio Sources*, 1986, Ed. by J. A. Zensus and T. J. Pearson, p. 260.
21. A. P. Marscher, Astrophys. J. **228**, 27 (1979).
22. M. Massi, G. Comoretto, M. Rioja, and G. Tofani, Astron. Astrophys., Suppl. Ser. **116**, 167 (1996).
23. L. I. Matveyenko, Preprint Pr-479, IKI (Institute for Space Research, Russian Academy of Sciences, Moscow, 1978).
24. L. I. Matveyenko, K. I. Kellermann, I. K. Pauliny-Toth, *et al.*, Pis'ma Astron. Zh. **2**, 77 (1980) [Sov. Astron. Lett. **6**, 42 (1980)].
25. L. I. Matveyenko *et al.*, Pis'ma Astron. Zh. **18**, 931 (1992) [Sov. Astron. Lett. **18**, 379 (1992)].
26. L. I. Matveyenko, I. I. K. Pauliny-Toth, L. B. Baath, *et al.*, Astron. Astrophys. **312**, 738 (1996).
27. L. I. Matveyenko, in *Proceedings of a Workshop on QUASAT—a VLBI Observatory in Space, Gross Enzersdorf, Austria, 1984*, ESA, SP-211, p. 119.
28. *Astrophysics, Part C: Radio Observations V-1*, Ed. by M. L. Meeks (Academic, New York, 1976), p. 253.
29. C. E. Naundorf, R. Wegner, A. Witzel, and A. Zensus, in *Proceedings of a Workshop on Compact Extragalactic Radio Sources, Socorro, 1994*, Ed. by J. A. Zensus and K. I. Kellermann, p. 255.
30. H. Netzer, in *Astrophysical Jets and Their Engines, Ser. C: Mathematical and Physical Science*, Ed. by W. Kundt (A. Reidel, Dordrecht, 1987), p. 103.
31. I. I. Pronik, Astron. Zh. **49**, 768 (1972) [Sov. Astron. **16**, 628 (1972)].
32. F. T. Rantakuro, L. B. Baath, I. I. K. Pauliny-Toth, *et al.*, Astron. Astrophys. **259**, 8 (1992).
33. V. A. Razin, Astron. Zh. **35**, 241 (1958) [Sov. Astron. **2**, 216 (1958)].
34. M. M. Romanova, G. V. Ustyugova, A. V. Koldova, *et al.*, Astrophys. J. **500**, 703 (1998).
35. C. J. Schalinski, W. Alef, A. Witzel, *et al.*, Symp. Int. Astron. Union, No. 129, 359 (1987).
36. C. Schalinski, S. Britzen, A. Witzel, *et al.*, in *Sub-arcsecond Radio Astronomy*, Ed. by R. J. Davis and R. S. Booth (Cambridge Univ. Press, Cambridge, 1992), p. 199.
37. N. I. Shakura and R. A. Sunyaev, Astron. Astrophys. **24**, 337 (1973).
38. A. R. Thompson, J. M. Moran, and G. W. Swenson, Jr., *Interferometry and Synthesis in Radio Astronomy* (Wiley, New York, 1986; Mir, Moscow, 1989).
39. V. Tribble, Mon. Not. R. Astron. Soc. **250**, 726 (1991).
40. J. A. Waak, J. H. Spencer, R. S. Simon, and K. J. Johnston, in *The Impact of VLBI on Astrophysics and Geophysics*, Ed. by M. J. Reid and J. M. Moran, Symp. Int. Astron. Union, No. 129, 141 (1987).
41. A. Witzel, in *Proceedings of a Workshop on Superluminal Radio Sources, 1986*, Ed. by J. A. Zensus and T. J. Pearson, p. 85.
42. J. M. Wrobel, T. J. Pearson, M. H. Cohen, and A. C. S. Readhead, in *The Impact of VLBI on Astrophysics and Geophysics*, Ed. by M. J. Reid and J. M. Moran, Symp. Int. Astron. Union., No. 129, 165 (1987).

Translated by V. Astakhov

Astronomy Letters, Vol. 27, No. 1, 2001, pp. 15–24. Translated from Pis'ma v Astronomicheskiĭ Zhurnal, Vol. 27, No. 1, 2001, pp. 19–30.

A Chemically Decoupled Nucleus and Structure of the Nuclear Region in the S0 Galaxy NGC 4036¶

O. K. Sil'chenko[1] * and V. V. Vlasyuk[2]

[1] *Sternberg Astronomical Institute, Universitetskiĭ pr. 13, Moscow, 119899 Russia*
[2] *Special Astrophysical Observatory, Russian Academy of Sciences, Nizhniĭ Arkhyz, Stavropolskiĭ Kraĭ, 357147 Russia*

Received February 2, 2000

Abstract—We present the results of a comprehensive spectrophotometric study of the central region in the regular lenticular galaxy NGC 4036 with two spectrographs of the 6-m telescope. The unresolved nucleus of NGC 4036 is shown to be chemically decoupled: [Mg/Fe] = +0.3 at the very center, whereas in the immediate vicinity of its nucleus, this ratio abruptly drops to +0.1 and does not change further along the radius. A study of isophotal morphology in combination with a kinematic analysis has proven that the rotation of stars at the NGC 4036 center is axisymmetric. However, the major-axis turn within $R < 5''$ should be considered real. We interpret this turn as evidence for the existence of a tilted circumnucelar stellar disk with a radius of ~250 pc in NGC 4036. The NGC 4036 bulge may be triaxial, and the ionized gas at the galactic center is then concentrated toward the principal plane of the ellipsoidal potential. *© 2001 MAIK "Nauka/Interperiodica".*

Key words: *lenticular galaxies, circumnuclear stellar disks*

INTRODUCTION

Lenticular galaxies were judged by their evolutionary status and by the composition of their stellar population to be similar to ellipticals, i.e., old and devoid of any interstellar medium, as far back as twenty years ago. Now, as these galaxies are painstakingly studied, they prove to be increasingly complex systems. First of all, in contrast to ellipticals, more than 30% of them exhibit an appreciable amount of neutral hydrogen (Chamaraux *et al.* 1986). However, systematic searches for traces of star formation in the disks of lenticular galaxies with a sufficient amount of H I yielded negative results for most objects: no young stars capable of ionizing hydrogen were detected (Pogge and Eskridge 1987, 1993). Nevertheless, there is also ionized gas (or even it alone) in many lenticular galaxies. The ionized gas is generally concentrated in central regions and exhibits LINER excitation; it is thought to be either external in origin or have been ejected by bulge stars during their evolution (Bertola *et al.* 1992, 1995). Again, the presence of this gas is not accompanied by on-going star formation in the galactic nucleus; however, the stellar population of the nuclear regions in 50% of the lenticular galaxies was found to be younger than 5–7 Gyr (Sil'chenko 1993). Maybe this comparatively recent star formation is still associated with the acquirement of gas, for example, during the interaction with another galaxy. The structure of many lenticular galaxies turned out to be complex as well. A photometric study by Seifert and Scorza (1996) revealed two unrelated disks—outer extended and inner compact ones—in half of the lenticular galaxies from their sample (eight objects). Based on a detailed study, Van den Bosch and Emsellem (1998) diagnosed the same double-disk structure in the S0 galaxy NGC 4570. Can these two disks be formed at different evolutionary stages of the galaxy? In three objects (NGC 1023, 7280, and 7332), we managed to associate these photometrically identifiable circumnuclear stellar disks with regions distinguished by stellar-population properties, namely, by a heavy-element overabundance and a relatively young age, 2–5 Gyr (Sil'chenko 1999a; Afanas'ev and Sil'chenko 2000). At least, the circumnuclear compact stellar disks in these galaxies were formed during separate, relatively recent and fairly violent episodes of their evolution. Were these episodes related to the absorption of another galaxy? Do we see traces of mergers in lenticular galaxies, which, from a theoretical point of view, are most commonly attributed to the evolution of ellipticals, but which have not yet been reliably detected in regular galaxies?

NGC 4036 is a classical lenticular galaxy, which, being bright enough and nearby (its global parameters are given in Table 1), has repeatedly been investigated both photometrically and spectroscopically in various wavelength ranges. Kent (1984), Michard and Marchal (1993), and Cinzano *et al.* (1999) performed its CCD optical surface photometry. They all obtained roughly the same results: the galaxy has a regular radial brightness profile, which can be represented as the sum of an

¶ Based on observations with the 6-m Special Astrophysical Observatory telescope.

* E-mail address for contacts: olga@sai.msu.ru

Table 1. Global parameters of NGC 4036 (LEDA database)

Morphological type	S0–
R_{25}	13 kpc
B_T^0	11.05
M_B	–20.63
$V_r(\odot)$	1392 km s^{-1}
V_r(LG)	1519 km s^{-1}
Distance	21.7 Mpc (H_0 = 75 km s^{-1} Mpc^{-1})
Disk inclination	71°
PA_{phot}	79°

extended exponential disk and a bright, but fairly compact de Vaucouleurs bulge. The optical rotation curve measured along the major axis of NGC 4036 both for the ionized gas and for stars by Fisher (1997), Bertola *et al.* (1995), and Cinzano *et al.* (1999) is closely similar for both galactic components and is also classical in shape: it rises virtually like a rigid-body one up to $R \approx$ 1 kpc and then flattens out. The velocity dispersions of the gas and stars within $R \approx 0.5$ kpc of the center are also the same, which led Cinzano *et al.* (1999) to conclude that the ionized gas at the NGC 4036 center originates in bulge stars. A radio study (Huchtmeier 1982) did not reveal any substantial amount of H I in the galaxy [note that Cinzano *et al.* (1999) committed an error in the Introduction to their paper: they took the upper limit on the H I mass in NGC 4036 from the catalog by Roberts *et al.* (1991) as the measured gas mass]. Thus, if there is a lenticular galaxy without any outward signs of the past interaction or merging, this is NGC 4036. Fisher *et al.* (1996) investigated the stellar population at the NGC 4036 center by measuring absorption-line indices (equivalent widths) in the integrated spectrum along the major and minor axes. Here, a peculiarity was first hinted at: they casually noted that an enhanced magnesium-to-iron ratio was observed in the galactic nucleus, which more closely resembles the stellar population of ellipticals, whereas the Mg/Fe ratio in the bulge is nearly solar. A simple visual analysis of their data argued for a chemically decoupled nucleus in NGC 4036. Since we have been investigating the chemically decoupled nuclei in disk galaxies [see Sil'chenko *et al.* (1992) for the discovery of such nuclei] and their possible origin through merging or interaction for several years, we have decided to carry out an independent spectroscopic study of NGC 4036.

OBSERVATIONS AND DATA REDUCTION

The central part of NGC 4036 was observed with a multipupil field spectrograph (MPFS) at the prime focus of the 6-m Special Astrophysical Observatory (SAO) telescope [see Afanas'ev *et al.* (1990) for a description of the instrument] three times: twice near the Mg Ib absorption line and once near Hα. In addition, we obtained one profile with a narrow 34″-long slit in the green using a spectrophotometric system at the Nasmyth-1 focus. A log of our spectroscopic observations for NGC 4036 is given in Table 2.

The detectors for the MPFS were Russian-made 520×580 and 1040×1160 CCD arrays; the spectrophotometric system at the Nasmyth-1 focus was equipped with a Photometrics 1024×1024 CCD. During the MPFS observations, an array of microlenses, 8×12 for the small CCD (in the red) and 8×16 for the large CCD (in the green), formed a pupil matrix, which was fed to the entrance of a grating spectrograph. This configuration allows up to 128 spectra to be simultaneously taken, each corresponding to a $1\farcs3 \times 1\farcs3$ spatial element of the galaxy image. We separately took a comparison spectrum of a helium–neon–argon lamp for wavelength calibration and a dawn-sky spectrum to make corrections for vignetting and for different microlens transmission. We also separately exposed the sky background near the galaxy in the green spectral range, where the equivalent widths of absorption lines were supposed to be calculated; its spectra were then smoothed and subtracted from the object's spectra. Since the sky background was not subtracted when reducing the long-slit spectrum (the slit was too short to "go" outside the galaxy), it was used to calculate absorption-line indices only in the immediate vicinity of the nucleus, where the galaxy is much brighter than the sky background. We calculated the velocities of the stellar component here by cross correlation with the dawn-sky spectrum. The main stages of data reduction—dark-current subtraction, cosmic-ray hit removal, extraction of one-dimensional spectra from the matrix format, extracted-spectrum linearization, construction of two-dimensional surface-brightness distributions and velocity fields—were performed by using the software package developed at the SAO (Vlasyuk 1993).

Table 2. Spectroscopic observations of NGC 4036

Date	T(exp), min	Field of view	PA(top)	Range, Å	Resolution, Å	$FWHM_*$
May 7, 1997	60	$10\farcs6 \times 21\farcs1$	221°	4100–5700	3.2–3.7	$2\farcs5$
Jan. 19, 1998	60	10.4×15.6	250	6200–6850	2.8–3.6	2.6
Jan. 23, 1998	40	10.9×21.8	67	4100–5700	4.0–5.5	2.2
Jan. 22, 1998	30	1.5×34	322	4500–5750	3.0	2.3

We used the MPFS observations in the spectral range 4100–5700 Å, first, to investigate the radial dependence of absorption-line equivalent widths and, second, to construct the two-dimensional line-of-sight velocity field of stars at the galactic center. The first goal was achieved by adding up the spectra in concentric rings centered on the galactic nucleus with a width and radial step of 1″.3, i.e., equal to the spatial element size; in this way, we managed to maintain an approximately constant signal-to-noise ratio along the radius, which is unattainable, say, during long-slit observations. Subsequently, we calculated the Hβ, Mgb, Fe5270, and Fe5335 indices in the standard Lick system (Worthey *et al.* 1994). Detailed model calculations in terms of synthesis models for an old stellar population are available for the above strong absorption lines (Worthey *et al.* 1994; Vazdekis *et al.* 1996; Tantalo *et al.* 1998). To achieve the second goal, the spectrum of each spatial element after continuum subtraction and conversion to the velocity scale was cross correlated with the spectra of the K0–K2 III giant stars observed during the set with the same instruments as the galaxy. The observations in the red were used to construct the two-dimensional ionized-gas line-of-sight velocity field. To this end, we measured precise centroid positions of the [N II] λ6583 emission line; since NGC 4036 is a LINER, the Hα emission is weak in its circumnuclear region. In addition, we constructed a surface-brightness map in [N II] λ6583 and in the nearby continuum. The night-sky λλ5577, 6300, and 6864 Å lines were used to check the wavelength-scale construction and the measured-velocity zero point. We estimated the accuracy of individual line-of-sight velocity measurements for the stars and the gas to be 20 and 30 km s^{-1}, respectively, and the accuracy of determining the equivalent widths of absorption lines in azimuthally averaged spectra to be 0.2 Å.

We made use of data from the Hubble Space Telescope (HST) archive to morphologically investigate the central part of NGC 4036. The galaxy was imaged with the WFPC2 instrument on August 8, 1994, as part of the Sargent Program "Searches for Active Galactic Nuclei of Very Low Luminosity." We used an F547M medium-band filter, which covered the spectral range from 5150 to 5800 Å; the exposure time was 300 s. The scale in the PC1 format with the galactic nucleus at its center was 0″.045 per pixel, and the spatial resolution was 0″.1. A 36″ × 36″ central part of the galaxy was exposed with this scale and resolution. The image morphology was analyzed with the FITELL code written by one of us (V.V.).

A CHEMICALLY DECOUPLED NUCLEUS IN NGC 4036

As we already mentioned in the Introduction, NGC 4036 belongs to those few lenticular galaxies whose circumnuclear stellar population has been studied by measuring absorption-line indices in the widely known Lick system. Fisher *et al.* (1996) carried out such a study in the one-dimensional case by observing NGC 4036 with a long slit along its major and minor axes. Jablonka *et al.* (1996) published similar "zero-dimensional" data: they integrated a 2″.5 × 10″.5 central region of the galaxy. We performed two-dimensional spectroscopy of NGC 4036 in the green twice and calculated an azimuthally averaged dependence of the Hβ, Mgb, Fe5270, and Fe5335 indices on distance to its center; we also have a one-dimensional profile of the galaxy with a long slit at position angle 142°, i.e., at 63° to the major axis. Figure 1 compares all our data with those of Fisher *et al.* (1996).

The first thing that catches the eye when looking at Fig. 1 is reasonably good agreement between all five observational sequences for the metal-line indices. This is a great stroke of luck, which could not be expected in advance: the Lick system of indices is believed to be fairly capricious and sensitive to the spectral resolution of observations. Meanwhile, our MPFS data with a resolution of 4–5 Å were reduced to the Lick system (resolution of ~8 Å) using the observations of standard

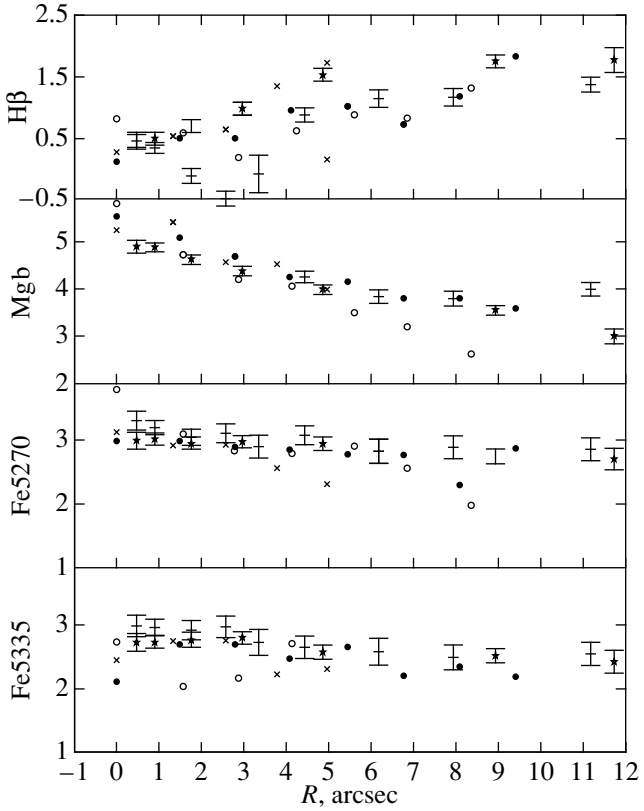

Fig. 1. Radial variations in Hβ, Mgb, Fe5270, and Fe5335 absorption-line indices, as inferred from our MPFS data in 1997 (dots) and 1998 (circles), from our long-slit data at Nasmyth-1 (crosses), and from the data of Fisher *et al.* (1996) obtained with a long slit along the major (pluses) and minor (asterisks) axes of NGC 4036. The measurements were corrected for stellar velocity dispersion in the galaxy.

Table 3. Mean absorption-line indices in the NGC 4036 nucleus

Hβ	0.40 ± 0.21
Mgb	5.56 ± 0.17
Fe5270	3.32 ± 0.26
Fe5335	2.44 ± 0.18

stars by Worthey *et al.* (1994), as were the data of Fisher *et al.* (1996), whereas no observations with the spectrophotometric system at Nasmyth-1 with 3 Å resolution are available. The absence of a systematic difference between the measured Mgb, Fe5270, and Fe5335 indices in the above papers proves that spectroscopic observations at Nasmyth-1 with such a spectral resolution and with stellar velocity dispersions in the galaxy of the order of 200 km s^{-1} yield the metal-line indices precisely in the Lick system and require no additional calibration. Yet another practical conclusion following from Fig. 1 is that the indices for the NGC 4036 nucleus can be estimated by directly averaging our three independent measurements. Mean estimates of the indices for the NGC 4036 nucleus with their errors corrected for a stellar velocity dispersion of 190 km s^{-1} [the mean between those given by Fisher (1997) and Chinzano *et al.* (1999)] are listed in Table 3.

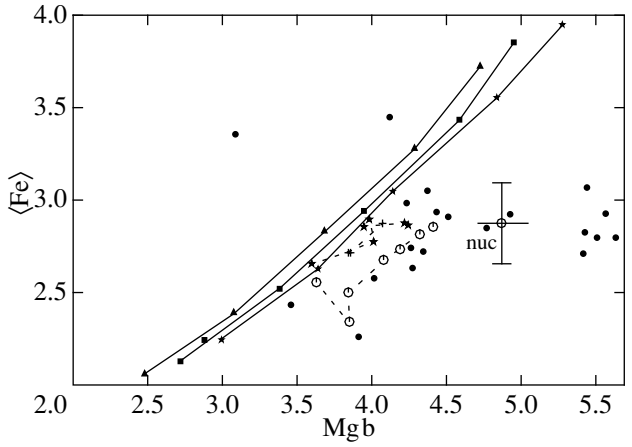

Fig. 2. (⟨Fe⟩, Mgb) diagram: a comparison of models and observational data. The models of Worthey (1994) (solid lines) were computed by synthesizing a homogeneous old stellar population for ages of 8 Gyr (triangles), 12 Gyr (squares), and 17 Gyr (small asterisks); metallicity decreases along each model sequence, from top to bottom, from +0.5 to –0.5 dex. The symbols connected by dashed lines represent observational data for the circumnuclear region of NGC 4036: our May 1997 data (large circles connected in order of increasing distance from the center) and the data of Fisher *et al.* (1996) for the major (pluses) and minor (large asterisks) axes. We estimated the position of the NGC 4036 nucleus in this diagram (marked by nuc) by averaging the 1997 and 1998 MPFS data and the Nasmyth-1 data. The magnesium index was corrected for the [N I] λ5200 emission. The dots represent the central regions of moderate-luminosity (M_B = –19...–20) ellipticals, as deduced from the data of Trager *et al.* (1998).

Curious physical conclusions can be reached by examining the dependence Hβ(*r*). In contrast to similar radial metal-line profiles, the profiles of Fisher *et al.* (1996) for Hβ along the major and minor axes differ markedly (the azimuthally averaged dependences lie between them). The most natural explanation is that the ionized gas concentrated into a fairly thin disk, i.e., visible predominantly along the major axis, floods the absorption more heavily precisely in this profile. If the deviation of the Hβ profile along the major axis from that along the minor one is taken to be a measure of the Balmer-emission intensity, then we conclude that the hydrogen emission, together with, possibly, star-forming regions, exhibits a flat ring-shaped distribution with a ~2″.5 radius. This is the same Hα ring as that found by Pogge and Eskridge (1993) at the centers of the lenticular galaxies NGC 4138 and 7013; however, they could not find it in NGC 4036, because the hydrogen emission here is lost in the intense Balmer absorption. At $R \geq 5''$, the difference between the Hβ-index profiles along the major and minor axes vanishes.

Unfortunately, the fact that the Hβ absorption line is flooded with emission prevents us from using a comparison of Hβ and Mgb or Hβ and ⟨Fe⟩ ≡ (Fe5270+Fe5335)/2 to separate the age and metallicity effects and to accurately determine each of the parameters. However, the (⟨Fe⟩, Mgb) diagram (Fig. 2) shows the NGC 4036 nucleus to be chemically decoupled. In this diagram, all models with a solar magnesium-to-iron ratio, irrespective of their common metallicity and star-formation history, are located within a narrow sequence, while any deviations from this sequence can be interpreted only as a nonsolar Mg/Fe ratio. Before transferring the data from Fig. 1 to the (⟨Fe⟩, Mgb) diagram (Fig. 2), we corrected the measured magnesium index for the [N I] λ5200 emission, which is rather strong at the NGC 4036 center. As Goudfrooij and Emsellem (1996) showed, the [N I] λ5200 emission line falls within the wavelength range where the continuum for the magnesium index is measured, and the presence of emission thus artificially increases its value; the correction that they recommend to apply to the magnesium index is approximately equal to 1.13EW([N I]). The data for NGC 4036 within a 5″ radius in Fig. 2 were corrected for the [N I] emission according to these recommendations. We can now directly estimate Mg/Fe for the stellar population. We see from Fig. 2 that the NGC 4036 nucleus is distinguished by an enhanced magnesium-to-iron ratio. This peculiarity is most likely characteristic of the stellar populations in ellipticals (Worthey *et al.* 1992), and we plotted the data from Trager *et al.* (1998) for the central regions of medium-luminosity ellipticals (M_B = –19…–20) in Fig. 2 for comparison: the NGC 4036 nucleus fell just in the middle of this cloud of data points. Based on the model of Tantalo *et al.* (1998), we estimated [Mg/Fe] for the NGC 4036 nucleus to be +0.3; Jablonka *et al.* (1996) obtained [Mg/Fe] ≈ +0.4 from their integrated

measurements through a $10''.5 \times 2''.5$ aperture. We believe this estimate to refer primarily to the nucleus as being considerably brighter than the nearby portions of the bulge. What distinguished NGC 4036 from most ellipticals is that the Mg/Fe ratio abruptly changes when passing from the nucleus to the bulge. As Worthey *et al.* (1992) showed, the elemental abundances in ellipticals change radially in such a way that the galaxy displaces in the ($\langle$Fe$\rangle$, Mgb) diagram almost parallel to the model sequence [Mg/Fe] = 0; i.e., Mg/Fe remains radially constant. At the same time, the Mg/Fe ratio in NGC 4036 (Fig. 2) clearly drops when passing from the nucleus to the bulge: [Mg/Fe] $\approx$ +0.1 as inferred from our data, while it is nearly solar as inferred from the data of Fisher *et al.* (1996). Since theoreticians of the chemical evolution of galaxies associate the Mg/Fe ratio primarily with the duration of the epoch of main star formation in stellar systems, we can state that the histories of star formation in the nucleus and bulge of the lenticular galaxy NGC 4036 were different.

STRUCTURE OF THE CENTRAL REGION IN NGC 4036

The galaxy NGC 4036 has a rich history of photometric studies. First Barbon *et al.* (1978) analyzed a two-dimensional photographic *B*-band image of the galaxy in detail and found it to consist of a bulge and an extended disk, which begins to dominate even at $R \approx 20''$ (2.1 kpc). They measured the following morphological parameters: the galaxy inclination, $i = 71°$, and the position angle of the isophotal major axis, $PA_0 = 79°$ (we included their data in Table 1). CCD observations followed next: Kent (1984, 1985) measured the radial variations in morphological parameters in outer regions and separated the disk and the bulge in the red filter *r*. Michard and Marchal (1993) measured the variations in morphological parameters with radius in its complete range at a moderate spatial resolution of $2''.6$–$2''.8$ and found the *B* and *V* isophotes at $R < 10''$ to be moderately box-shaped. Finally, Cinzano *et al.* (1999) again performed complete *V*-band surface photometry of NGC 4036 with the 2.3-m Bok ground-based telescope (KPNO) with a spatial resolution of $1''.7$ and on the basis of HST data with $0''.1$ resolution through an F547M filter, which we also use below (see the next section). All these published data remarkably agree with each other, suggesting that the peculiarities of the central structure of NGC 4036 have been firmly established; nevertheless, they have avoided a detailed discussion so far. We rely primarily on the most recent study by Cinzano *et al.* (1999); previous studies are consistent with it, but have a lower spatial resolution.

First of all, Cinzano *et al.* (1999) note an appreciable turn of the isophotal major axis from PA = 98° at $R = 1''$ to PA = 67° at $R = 5''$: the ellipses, as it were, oscillate about the location of the line of nodes for the global disk $PA_0 = 79°$. An equilibrium orientation is reached at $R \approx 10''$ and does not change any longer further out. According to ground-based observations, the isophotal ellipticity does not tend to zero as the center is approached, as is usually the case in galaxies with big bulges; it freezes at ~0.12. As regards the HST data with their excellent resolution, they reveal a local maximum $1 - b/a \approx 0.3$ at $R \approx 2''$. Cinzano *et al.* (1999) propose to explain such a behavior of the isophotes at the NGC 4036 center in two possible ways: either this is an intricate dust distribution which seems to them to be more likely, or this is a manifestation of a "slight triaxiality" of the inner bulge regions. Given that the fourth coefficient a_4 of the cosine of an azimuthal Fourier decomposition of the brightness at $R = 1''$ is approximately equal to $+0.01a$, we can offer a third plausible explanation: there is a tilted circumnuclear stellar disk at the NGC 4036 center; in that case, however, the nature of the deviation of the isophotal major axis from the line of nodes at $R = 3''$–$5''$ is yet to be elucidated. One of these three hypotheses can be chosen only by simultaneously analyzing photometry and kinematics (see the next section).

It is also curious to compare the ionized-gas distribution at the NGC 4036 center with the distribution of stars. Based on the intensity profile of the [OII] λ3727 emission line (the slit was placed along the major axis), Cinzano *et al.* (1999) assure that the emission-line intensity profile within $R < 6''$ follows de Vaucoulers' law. Since the velocity dispersion of gas clouds within $R < 5''$ also increases sharply, it is immediately concluded that the gas at the very center of NGC 4036 closely follows the distribution and kinematics of stars and most likely has its origin in stellar winds from bulge red giants. The kinematics is discussed in the next section, while Fig. 3a shows a two-dimensional intensity distribution of the [N II] λ6583 emission line in comparison with the intensity in the neighboring continuum, which characterizes the distribution of old stars. The distributions are seen to be different: intensity isophotes of the [N II] emission line appear more elongated than do continuum isophotes. Figure 3b shows the radial variations in major-axis position angle and in isophotal ellipticity of both distributions calculated by using the FITELL code. In general, the quantitative morphological parameters deduced from MPFS images should have been treated with caution: the number of independent image elements is too small, while the point spread function is a moderately circular two-dimensional Gaussian. However, we can check the accuracy of PA and $1 - b/a$ calculated in our specific case by comparison, for example, with the results of Michard and Marchal (1993): their *B*-band observations were carried out at $2''.65$ seeing, almost as in our case. This comparison (Fig. 3b) indicates that our results pertaining to continuum isophotes are very close to reality: the ellipticities just match closely, while the radial variations in position angle are repeated with a small systematic shift. Based on Fig. 3b, we can there-

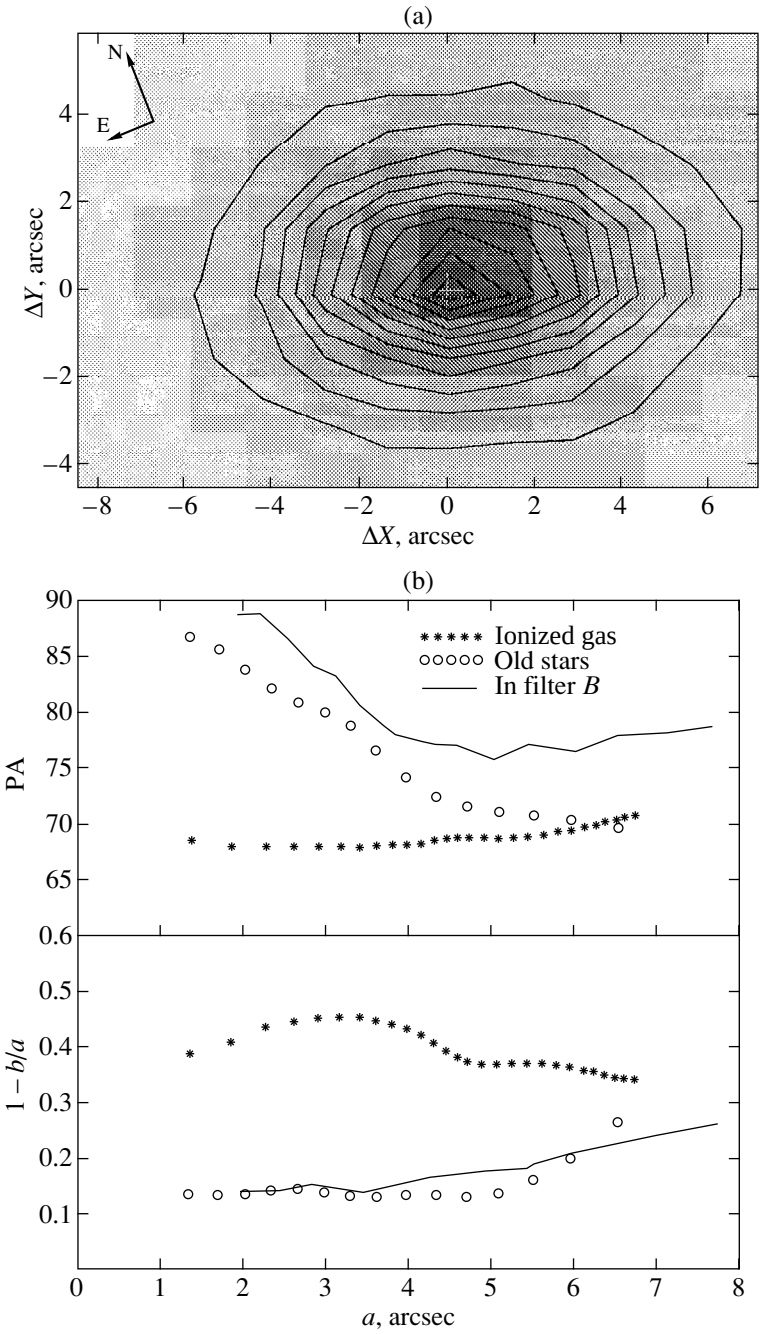

Fig. 3. Comparison of morphological parameters for the distribution of ionized gas and stars at the NGC 4036 center, as deduced from our MPFS data in the spectral range 6200–6900 Å: (a) surface-brightness isophotes for the continuum at 6500 Å (filled) and for the [N II] λ6583 Å emission line (contour); and (b) radial variations in the position angle of the major axis of isophotes and in their ellipticity, as inferred from our MPFS data in continuum (circles) and in the [N II] emission line (asterisks), as well as from the *B*-band data of Michard and Marchal (1993) at a seeing similar to ours.

fore assert with confidence that Cinzano *et al.* (1999) are wrong, and that the ionized-gas distribution at the NGC 4036 center does not closely follow the distribution of stars at all. The major axes of the emission-line and continuum isophotes at $R = 1''$–$2''$ differ in position angle by almost 20°: the gas distribution up to the very center maintains an isophotal position angle PA ≈ 70°, to which the distribution of stars comes only at $R \approx 5''$. This result is also indirectly confirmed by the image from the HST archive. Figure 4 shows a map of the residual brightness through the F547M filter after the subtraction of a model image with regular elliptical isophotes whose parameters were calculated from the original image by means of the FITELL code. We see

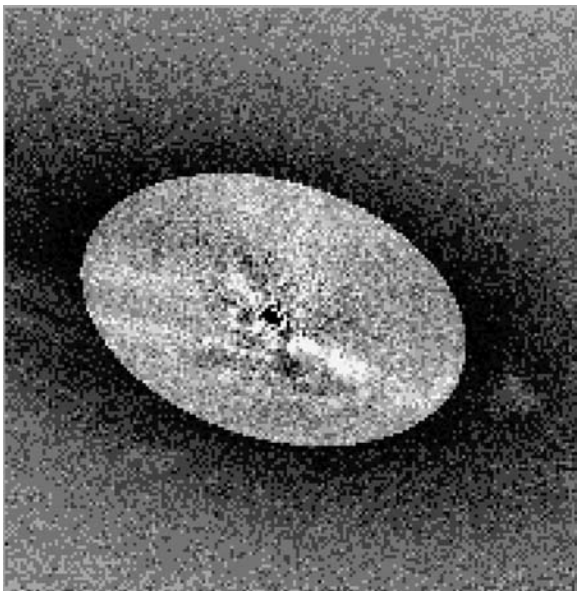

Fig. 4. A map of residual brightness through the F547M (WPFC2 HST) filter after subtracting a model with elliptical isophotes. North is at the top (vertical position angle $+7\overset{\circ}{.}5$), and east is on the left; the imaged region is $34'' \times 34''$ in size. Since the model was not subtracted at the very center, it is painted black, and the light ellipse bounds the region in which the model was subtracted.

than the thin straight dust lane extends from the center to a distance of several arcsec just at PA ≈ 70°. In addition, the ellipticity of emission-line isophotes exceeds considerably the ellipticity of continuum isophotes, although it does not reach 0.6 typical of an infinitely thin disk tilted at 70° to the plane of the sky (as the global disk of NGC 4036). Thus, the gas at the NGC 4036 center is associated neither with the bulge nor with the global disk of the galaxy. Precisely what structure we see in the [N II] λ6583 emission can be determined by invoking kinematic data.

KINEMATICS OF THE GAS AND STARS IN THE CENTRAL REGION OF NGC 4036

The two-dimensional velocity fields of the stars and ionized gas constructed from our MPFS data are shown in Fig. 5. Basically, the two fields look very similar (at this spatial resolution), and both exhibit regular quasi-rigid rotation with approximately the same angular velocities. The lines of equal gas velocity show a faint hint of *z* distortion, which is usually characteristic of gas rotation in a triaxial potential. A local extremum at 7″ from the center fell with the measured portion of the stellar velocity field; otherwise, a more classical

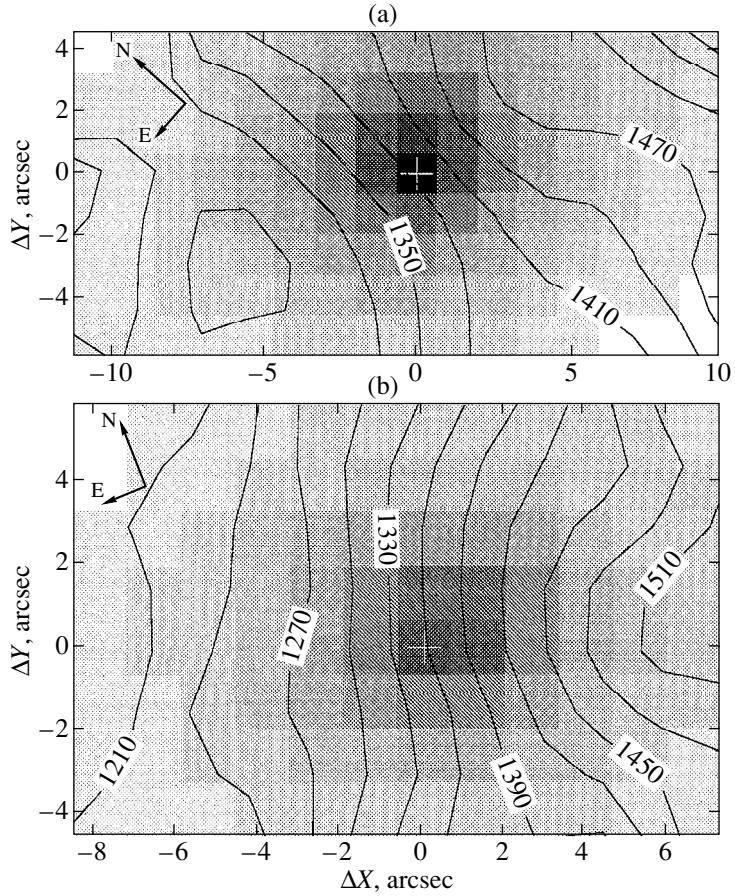

Fig. 5. Two-dimensional line-of sight velocity fields for (a) the stars and (b) ionized gas at the NGC 4036 center, as constructed from our MPFS data.

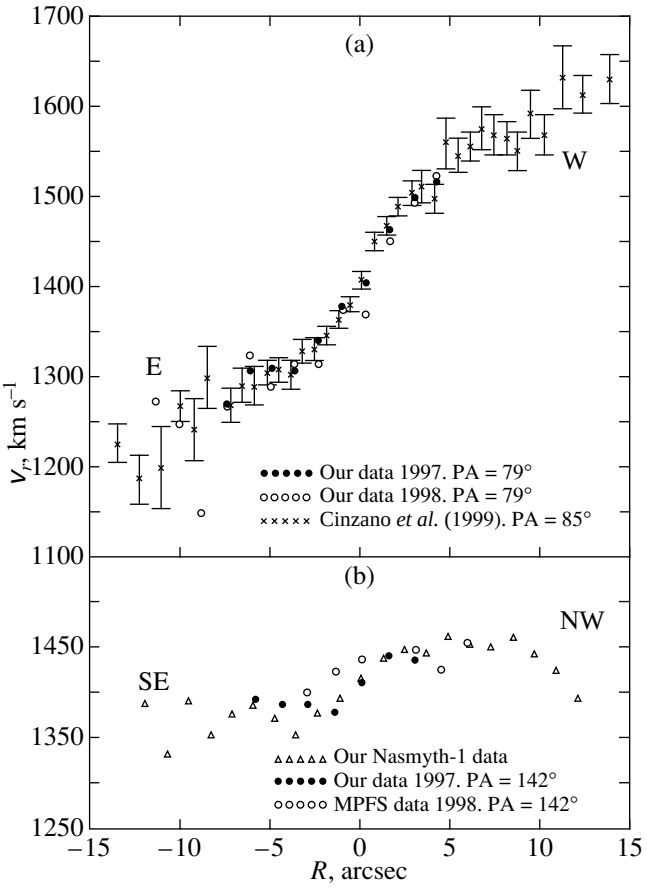

Fig. 6. Comparison of one-dimensional line-of-sight velocity profiles for the stellar component at the NGC 4036 center: (a) along the major axis; and (b) at 63° to the major axis.

appearance of the velocity field for circular rotation is difficult to imagine.

The quality of our gas and stellar line-of-sight velocity fields for the NGC 4036 center can be checked by comparing our data with published ones. However, the two-dimensional velocity fields have been obtained for NGC 4036 for the first time: only one-dimensional profiles constructed from long-slit observations can be found in the literature. We modeled such profiles using our data by superimposing narrow, 2″-wide masks oriented along the major axis on two-dimensional velocity fields. The model profiles are compared with the observational data of Cinzano *et al.* (1999) in Figs. 6 (stars) and 7 (ionized gas). Apart from a comparison of the velocity profiles along the major axis, Fig. 6 compares the line-of-sight velocity profiles of stars at 63° to the major axis: the model one and that constructed from our observations with the spectrophotometric system at Nasmyth-1. A joint analysis of the two parts of Fig. 6 indicates that the 1997 kinematic data are better than the 1998 data for stars; the May 1997 model profiles closely coincided with the slit ones. As regards the MPFS kinematic data for the ionized gas, they generally follow the profile of Cinzano *et al.* (1999), although they do not closely follow fine features such as the "steps" at $R = \pm 3''$–$5''$ or the counterrotating portion at the center. Clearly, this is because the spatial resolution of our 1998 observations was approximately a factor of 2 lower than that for the observations of Cinzano *et al.* (1999). On the other hand, the two-dimensional line-of-sight velocity distributions allow us to diagnose the pattern of rotation and the axial symmetry of the potential, which cannot be done using a single profile along the major axis.

Under conditions of axisymmetric rotation, the azimuthal variations in apparent central line-of-sight velocity gradient obey a cosine law as long as we remain within the region of rigid rotation:

$$dv_r/dr = \omega \sin i \cos(\mathrm{PA} - \mathrm{PA}_0),$$

where ω is the angular velocity of the galactic center, i is the inclination of the galaxy's disk rotation axis to the line of sight, and PA_0 is the position angle of the line of nodes. In NGC 4036, the rotation is strictly rigid up to $R = 4''$ and virtually rigid up to $R \approx 8''$ (Fig. 6). Therefore, using our two-dimensional velocity fields (Fig. 5), we determined the positions of maxima in the azimuthal dependences of central line-of-sight velocity gradients, which we call below the orientation of the dynamical major axis, both for stars and for the gas, at several distances from the center in the range $R = 1\farcs5$–$5\farcs5$. To this end, we fitted cosine curves to the observed dependences of gradients dv_r/dr measured in three R ranges by least squares. The coincidence of the photometric and dynamical major axes proves that the rotation is axisymmetric, while the photometric and dynamical axes in a triaxial potential turn in opposite directions from the line of nodes of the rotation plane (Monnet *et al.* 1992). Figure 8 compares the orientations of the dynamical and photometric major axes in the central part of NGC 4036; whereas the HST data show the true orientation of the potential shape at a given radius, the data of Michard and Marchal (1993) exhibit a smoothing of the true dependence PA(R) for observations at seeing $\mathrm{FWHM}_* = 2\farcs6$. We see that the change in dynamical major axis, both for stars and, in general, for the gas, qualitatively corresponds to the change in photometric major axis with radius. Since the accuracy of determining the cosinusoid phases dv_r/dr(PA) is 3°–5°, the deviation of the dynamical major axes of ionized-gas rotation from the line of nodes of the global galactic disk may actually turn out to be insignificant. However, a turn of the dynamical major axis through 20° appears quite reliable, and it is consistent with the behavior of the photometric major axis as inferred from the data of Michard and Marchal (1993). We therefore conclude that the rotation of stars at the NGC 4036 center appears axisymmetric at each individual radius, but it definitely does not take place in the galaxy's principal plane within $R < 2\farcs5$. If we use high-resolution photometry, i.e., the HST data, then

two discrete structures show up. One is seen at $R = 1''$–$3''$, is elongated at PA ≈ 90°, and is probably a circumnuclear stellar disk. The other is seen at $R = 4''$–$6''$ and is elongated at PA ≈ 70°; its nature is less clear.

DISCUSSION

What does happen at the NGC 4036 center in the first place? Objecting to Cinzano *et al.* (1999), we can now say with confidence that the turn of the isophotal major axis through 30° within 5″ of the center is not merely the semblance due to a clumpy dust distribution, because the dynamical major axis of stars also exhibits a similar turn. Taking into account the coincidence of the photometric and dynamical major axes of the stellar component within $R \le 2''$, the positive parameter a_4, and the local ellipticity maximum at $R = 1''$–$2''.5$, we conclude that a tilted compact stellar disk with a radius of 250 pc most likely exists at the very center of NGC 4036. The nature of the structural component that manifests itself in morphology at $R = 3''$–$6''$ is less clear. On the one hand, this may also be a tilted (in the opposite direction) stellar disk. However, the isophotal ellipticity at this location is rather low. On the other hand, there are such puzzling features in NGC 4036 as the straight narrow dust lane at PA = 250°(70°), which extends from the nucleus westward (Fig. 4), and ionized-gas counterrotation within ±1″ of the nucleus (Fig. 7), which is seen in the kinematic profiles along the major axis obtained by Fisher (1997) and, independently, by Cinzano *et al.* (1999) (it did not manifest itself in our data because of insufficient spatial resolution). The dust lane at PA = 250° with no extension on the other side of the nucleus lies in the galaxy's half that recedes from us as it rotates and closely resembles a shock front in the gas striking the bar edge. The change in the sense of rotation of the gas, which is a dissipative component, as the galaxy center is approached would also be expected most likely in a triaxial potential, where there are intense radial flows and the tangential gas velocity is suppressed by the shock wave. It may well be that the compact bulge of NGC 4036, which, as follows from the decomposition of the radial brightness profile by Kent (1985) and Cinzano *et al.* (1999), dominates over the disk only within $R < 7''$, is actually triaxial, with the projected major axis at PA ≈ 70°. The constant isophotal orientation of the [N II] emission surface-brightness distribution, PA ≈ 70° (Fig. 3b), can then be explained by the fact that the gas "settled" to the principal plane of the triaxial bulge.

We have repeatedly pointed out a discrepancy between the sizes of chemically and structurally decoupled regions at the centers of early-type disk galaxies. There are simultaneously an unresolved chemically decoupled nucleus and much more extended (up to a radius of 100–800 pc) circumnuclear stellar disks in M 31 (Sil'chenko *et al.* 1998), NGC 4216 and 4501 (Sil'chenko *et al.* 1999), and the S0 galaxies NGC 1023

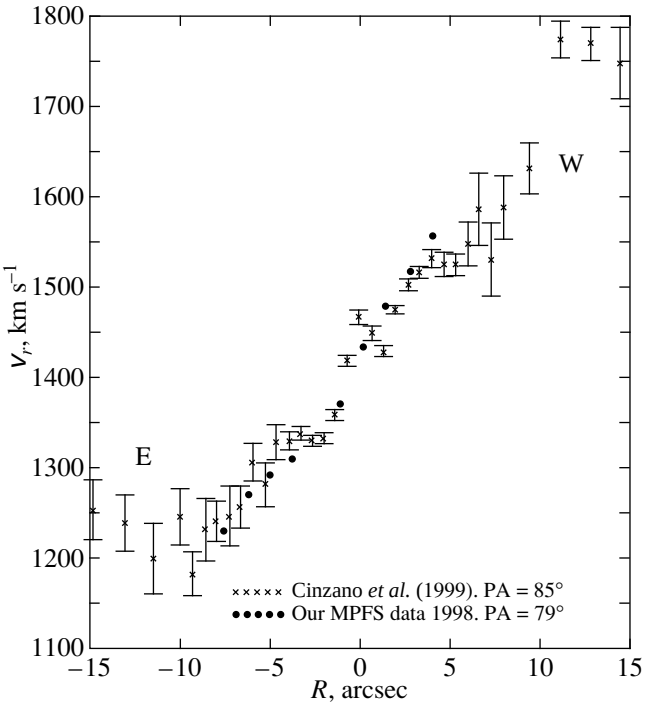

Fig. 7. Comparison of one-dimensional line-of-sight velocity profiles for the ionized gas at the NGC 4036 center; the slit is aligned with the major axis.

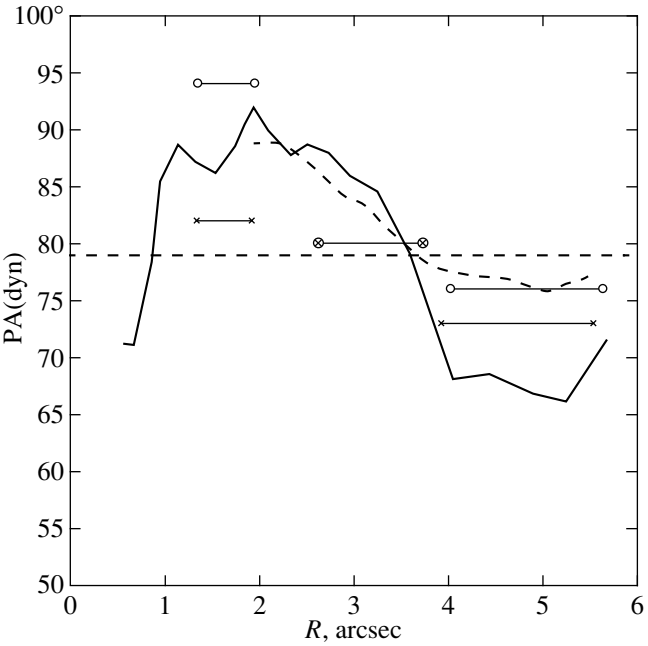

Fig. 8. Comparison of the orientations of the photometric major axis [the solid line and the line with short dashes represent the HST data and the data of Michard and Marchal (1993), respectively] and the dynamical major axis for the stars (the circles represent our 1997 MPFS data) and ionized gas (crosses). The horizontal line with long dashes specifies the orientation of the line of nodes for the global galactic disk.

and 7332 (Sil'chenko 1999a). In some cases, for example, in NGC 1023 (Sil'chenko 1999a) or NGC 7331 (Sil'chenko 1999b), we managed to firmly establish a difference in the ages of these subsystems: the mean ages of stars in the nucleus is 2 to 3 Gyr older than that in the circumnuclear disk; the nuclei exhibit a magnesium overabundance, while the Mg/Fe ratio in the disks is solar. All of this fits in a scenario where a secondary starburst in the nucleus and in the circumnuclear disk began quasi-simultaneously, but it ended much earlier in the nucleus and lasted for another 2 to 3 Gyr in a ring zone around the nucleus. Although the age of the stellar population at the NGC 4036 center has not yet been reliably determined, the abrupt change in Mg/Fe between the nucleus and its immediate vicinity, including the circumnuclear stellar disk, argues precisely for this scenario for this galaxy as well.

ACKNOWLEDGMENTS

We wish to thank A.N. Burenkov and S.N. Dodonov from the SAO, as well as A.V. Moiseev, a postgraduate at the SAO, for help with the 6-m telescope observations. The observational data used here were obtained with the 6-m telescope financed by the Ministry of Science of the Russian Federation (register number 01-43) and with the NASA/ESA Hubble Space Telescope operated by the Association of Universities for Studies in Astronomy under contract with the NASA (NAS 5-26 555). We used data from the HST archive. We also used the LEDA database, provided by the LEDA team at the CRAL Lyon Observatory (France). This study was supported by the Russian Foundation for Basic Research (project no. 98-02-16196), the President's grant of the Russian Federation for support of Doctors of Science (no. 98-15-96029), and a grant of the Russian State Science and Technology Program "Astronomy. Fundamental Space Research" (Astronomy Section) 1.2.4.1.

REFERENCES

1. V. L. Afanasiev and O. K. Sil'chenko, Astron. J. **119**, 126 (2000).
2. V. L. Afanas'ev, V. V. Vlasyuk, S. N. Dodonov, and O. K. Sil'chenko, Preprint No. 54 (Special Astrophysical Observatory, 1990).
3. R. Barbon, L. Benacchio, and M. Capaccioli, Astron. Astrophys. **65**, 165 (1978).
4. F. Bertola, L. M. Buson, and W. W. Zeilinger, Astrophys. J. Lett. **401**, L79 (1992).
5. F. Bertola, P. Cinzano, E. M. Corsini, *et al.*, Astrophys. J. Lett. **448**, L13 (1995).
6. P. Chamaraux, C. Balkowski, and P. Fontanelli, Astron. Astrophys. **165**, 15 (1986).
7. P. Cinzano, H.-W. Rix, M. Sarzi, *et al.*, Mon. Not. R. Astron. Soc. **307**, 433 (1999).
8. D. Fisher, Astron. J. **113**, 950 (1997).
9. D. Fisher, M. Franx, and G. Illingworth, Astrophys. J. **459**, 110 (1996).
10. P. Goudfrooij and E. Emsellem, Astron. Astrophys. **306**, L45 (1996).
11. W. K. Huchtmeier, Astron. Astrophys. **110**, 121 (1982).
12. P. Jablonka, P. Martin, and N. Arimoto, Astron. J. **112**, 1415 (1996).
13. S. M. Kent, Astrophys. J., Suppl. Ser. **56**, 105 (1984).
14. S. M. Kent, Astrophys. J., Suppl. Ser. **59**, 115 (1985).
15. R. Michard and J. Marchal, Astron. Astrophys., Suppl. Ser. **98**, 29 (1993).
16. G. Monnet, R. Bacon, and E. Emsellem, Astron. Astrophys. **253**, 366 (1992).
17. R. W. Pogge and P. B. Eskridge, Astron. J. **93**, 291 (1987).
18. R. W. Pogge and P. B. Eskridge, Astron. J. **106**, 1405 (1993).
19. M. S. Roberts, D. E. Hogg, J. N. Bregman, *et al.*, Astrophys. J. Suppl. Ser. **75**, 751 (1991).
20. W. Seifert and C. Scorza, Astron. Astrophys. **310**, 75 (1996).
21. O. K. Sil'chenko, Pis'ma Astron. Zh. **19**, 693 (1993) [Astron. Lett. **19**, 279 (1993)].
22. O. K. Sil'chenko, Astron. J. **117**, 2725 (1999a).
23. O. K. Sil'chenko, Astron. J. **118**, 186 (1999b).
24. O. K. Sil'chenko, V. L. Afanas'ev, and V. V. Vlasyuk, Astron. Zh. **69**, 1121 (1992) [Sov. Astron. **36**, 577 (1992)].
25. O. K. Sil'chenko, A. N. Burenkov, and V. V. Vlasyuk, Astron. Astrophys. **337**, 349 (1998).
26. O. K. Sil'chenko, A. N. Burenkov, and V. V. Vlasyuk, Astron. J. **117**, 826 (1999).
27. R. Tantalo, C. Chiosi, and A. Bressan, Astron. Astrophys. **333**, 419 (1998).
28. S. C. Trager, G. Worthey, S. M. Faber, *et al.*, Astrophys. J., Suppl. Ser. **116**, 1 (1998).
29. F. C. van den Bosch and E. Emsellem, Mon. Not. R. Astron. Soc. **298**, 267 (1998).
30. A. Vazdekis, E. Casuso, R. F. Peletier, and J. E. Beckman, Astrophys. J., Suppl. Ser. **106**, 307 (1996).
31. V. V. Vlasyuk, Izv. Spets. Astrofiz. Obs. **36**, 107 (1993).
32. G. Worthey, Astrophys. J., Suppl. Ser. **95**, 107 (1994).
33. G. Worthey, S. M. Faber, and J. J. González, Astrophys. J. **398**, 69 (1992).
34. G. Worthey, S. M. Faber, J. J. González, and D. Burstein, Astrophys. J., Suppl. Ser. **94**, 687 (1994).

Translated by V. Astakhov

Astronomy Letters, Vol. 27, No. 1, 2001, pp. 25–28. Translated from Pis'ma v Astronomicheskiĭ Zhurnal, Vol. 27, No. 1, 2001, pp. 31–35.

Infrared Photometry of the X-ray Binary XTE J1118+480 in April 2000

O. G. Taranova* and V. I. Shenavrin

Sternberg Astronomical Institute, Universitetskiĭ pr. 13, Moscow, 119899 Russia

Received May 3, 2000; in final form, July 10, 2000

Abstract—We present the IR photometry of the X-ray binary XTE J1118+480 performed during seven nights in April and two nights in May–June 2000. A significant IR excess has been detected in the object, which may be due to the thermal radiation from a dust envelope/cloud. The observed energy distribution in the range 1.25–3.5 μm can be interpreted in terms of the sum of the fluxes from an accretion disk with a temperature of ~20 000 K and a dust envelope with grains heated to ~900 K. The distance to the X-ray binary estimated from the total flux from the dust envelope is no less than 0.6–3 kpc. The mean optical depth of the dust envelope for the accretion-disk radiation is about 0.06. © *2001 MAIK "Nauka/Interperiodica".*

Key words: *infrared astronomy, X-ray sources, dust envelopes*

INTRODUCTION

During the RXTE All-Sky Monitor experiment, Remillard *et al.* (2000) detected X-ray emission from a new source, XTE J1118+480; its X-ray flux was ~39 mCrab in late March 2000. Rapid (~10 s) flares with fluxes a factor of 5 higher than 25 mCrab were observed, suggesting, in the authors' opinion, that the X-ray nova is Galactic in origin. It has a power-law spectrum up to 30 keV, with a photon index of ~1.8 (as for Cyg X-1 in quiescence). Reports on observations of the X-ray nova with ground-based and space (Hubble, ASCA) telescopes and the results of their preliminary analysis are published in current issues of the IAU Circular. Uemura *et al.* (2000) reported a possible optical counterpart, an $18\overset{m}{.}8$ star in red light. In March, Garcia *et al.* (2000) performed optical spectroscopy and concluded that its spectrum was typical of an X-ray nova during outburst. They estimated the interstellar reddening from the Na D equivalent width to be close to $E(B–V) \sim 0\overset{m}{.}024$. Cook *et al.* (2000) obtained its *V* light curve during five nights, detected periodic brightness variations with a period of $\sim 0\overset{d}{.}1706$, and assumed that the X-ray source was a component of a close binary system with an orbital period of $\sim 0\overset{d}{.}1706$. In early April 2000, Mauche *et al.* (2000) first obtained an *EUV* (70–120 Å) spectrum for the black-hole candidate of the X-ray binary XTE J1118+480; the source flux was $\sim 4 \times 10^{-13}$ erg s^{-1} cm^{-2} Å^{-1} at a wavelength of ~9 nm. Haswell *et al.* (2000a, 2000b) reported Hubble Space Telescope observations of the X-ray nova in the range 115–800 nm for almost 2.5 hours. The flux at a wavelength of 150 nm was $\sim 4 \times 10^{-13}$ erg s^{-1} cm^{-2} Å^{-1}, with a dependence flatter than $F(\nu) \propto \nu^{1/3}$ in the range 115–800 nm. Analyzing their results and optical observations of XTE J1118+480, the authors concluded that the mass of the primary component did not exceed $3M_\odot$. Based on their optical photometry during 27 nights, Patterson (2000) with his colleagues confirmed and refined the period of ~0.17 day and concluded that there were no other periods (except the short-period flickering on a time scales less than 10 s).

On the initiative of S.Yu. Shugarov, we started IR photometry of the object on April 12, 2000.

OBSERVATIONS

We performed our *JHKL* photometry of the X-ray source XTE J1118+480 with an InSb photometer at the Cassegrain focus of the 1.25 m telescope at the Crimean Station of the Sternberg Astronomical Institute. The star BS 6602 (Johnson *et al.* 1966) served as the photometric standard. Weather conditions permitted us to obtain seven IR brightness estimates for the object from April 12 until the end of the month (Taranova and Shenavrin 2000); they are listed in Table 1, together with their standard errors. The third row from bottom gives the object's mean *JHKL* magnitudes. The IR photometry in May and June 2000 is added in the last two rows of the table.

DISCUSSION

Observations of X-ray sources in binary systems show that optical radiation comes either from the

* E-mail address for contacts: taranova@sai.msu.ru

Table 1. *JHKL* photometry for the X-ray binary XTE J1118+480.
The standard is BS 4335 (J = 1.16, H = 0.58, K = 0.43, L = 0.32).

Date, 2000	JD	J	$\sigma(J)$	H	$\sigma(H)$	K	$\sigma(K)$	L	$\sigma(L)$
Apr. 12–13	2451647.280	12.56	0.34			10.79	0.09		
Apr. 12–13	2451647.284	12.35	0.27						
Apr. 14–15	2451649.456	12.11	0.24	11.97	0.24	10.93	0.12	9.11	0.41
Apr. 15–16	2451650.317	12.47	0.23	11.83	0.12	10.80	0.07	9.29	0.13
Apr. 24–25	2451659.321					10.98	0.17		
Apr. 25–26	2451660.283	11.94	0.36	11.73	0.14	10.89	0.11	8.74	0.23
Apr. 26–27	2451661.326	12.51	0.24	11.84	0.16	11.01	0.12		
Mean		12.37	0.10	11.90	0.07	10.83	0.05	9.2	0.1
May 19–20	2451684.310	12.39	0.12	11.52	0.13	10.94	0.15		
June 11–12	2451707.318	12.42	0.27			11.12	0.12		

binary's normal component or from an accretion disk around the relativistic star (black hole). If the detected 0.1708-day period for the X-ray binary XTE J1118+480 is orbital, then the X-ray source is similar in this parameter to the X-ray binary Cyg X-3. The latter, in turn, is a low-mass system whose optical component is an optically invisible star. Besides, as was noted above, no star brighter than $18\overset{m}{.}8$ in red light has been detected near XTE J1118+480.

Let us now see what the X-ray binary is in the near IR 1.25–3.5 μm. First, it follows from the data in Table 1 that the system exhibits a significant IR excess, as suggested by its color indices, $(H–K) \sim 1^m$ and $(K–L) \sim 1\overset{m}{.}7$: they are much greater than the maximum possible values for normal stars with $(H–K) < 0\overset{m}{.}45$ and $(K–L) < 0\overset{m}{.}4$ (Koornneef 1983).

Thermal emission from the circumstellar dust and nonthermal free–free gas emission are the most likely sources of excess IR radiation. The $H–K$ color index can serve as a criterion for selecting the source of IR excess radiation in hot stars (Allen and Swings 1972). If $(H–K) \geq 1$, then dust emission is most likely. For $(H–K) < 1$, the second alternative is most likely. If this criterion is applied to the object under study, then we see from the data in Table 1 that the mean value of the above color index is close to unity, and the choice between the sources of IR excess radiation based on this criterion is uncertain. If the observed $K–L$ color index is taken into account, then the dust component is the most likely source of IR excess radiation at $\lambda > 1.6$ μm. This conclusion can be drawn from the following considerations. For free–free gas emission, the $H–K$ and $K–L$ color indices are almost the same over a wide range of temperatures. For example, at a gas temperature of 10^4 K, their values are, respectively, $0\overset{m}{.}9$ and 1^m; at a temperature of ~5000 K, both indices are $\sim 1\overset{m}{.}2$, with the $J–H$ color index exceeding $0\overset{m}{.}7$. The observed $K–L$ is $2\overset{m}{.}5$–$2\overset{m}{.}6$, while $(J–H) < 0\overset{m}{.}7$ (Table 1). Consequently, the observed $(J–H)$, $(H–K)$, and $(K–L)$ color indices most likely point to a dust nature of the observed IR excess, and the thermal emission from the dust envelope/cloud is the most probable source of IR excess radiation for $\lambda > 1.6$ μm. Since the series of IR observations is small, the nonthermal gas emission cannot be completely ruled out.

Here, we dwell on the thermal origin of the observed IR excesses and estimate parameters of the sources with 1.25–3.5-μm radiation. The observed scatter in $J–H$ (Table 1) does not allow us to use this parameter to reliably classify the source with 1.25–1.65-μm radiation. According to the data from Koornneef (1983), the observed $J–H$ correspond to a fairly large spread in normal stars, from K0 to K5. Besides, the dust-envelope emission can show up even at 1.65 μm (H). In view of the above discussion, we will use the blackbody (BB) approximation to estimate parameters of the KL excess radiation. In that case, the mean color index is $J–H = 0\overset{m}{.}50 \pm 0\overset{m}{.}13$, and this color index corresponds to a BB temperature of ~4000 K. Clearly, the BB approximation enables us to estimate a lower limit on the excess IR radiation flux. Subtracting the BB radiation with a 4000 K temperature from the observed IR fluxes and attributing all the J radiation to it, we find that the $K–L$ color index in the excess radiation is $\sim 2\overset{m}{.}4$, its observed mean value is $\sim 2\overset{m}{.}7$ (Table 1), and these two values lead to almost the same estimates of the BB temperature, ~800–900 K. The total flux from the cool (~900 K) blackbody source (dust envelope) is

$$F_{\rm tot}^{\rm dust} = (1/\alpha)\Sigma[F_{\rm obs}(\lambda)\Delta\lambda] \approx 7 \times 10^{-11} \text{ erg s}^{-1} \text{ cm}^{-2},$$

where $\alpha \approx 0.25$ is the fraction of the 1.25–3.5-μm radiation in the total emission of a ~900 K blackbody.

The observed 1.25–1.56-μm (~4000 K) radiation from the X-ray nova XTE J1118+480 is most likely a mixture of the emissions from the hotter source and the dust envelope. To estimate parameters of the hot

source, we use *V* photometry (Cook *et al.* 2000). Fitting the 0.55–1.65-μm spectral energy distribution of XTE J1118+480 by $F(\lambda) \propto \lambda^{\beta}$ (β is the spectral index) yields $\beta \approx -2.3$ (or $\alpha \sim 1/3$ for $F(\nu) \propto \nu^{\alpha}$); this value surprisingly matches the spectral index derived from Hubble Space Telescope data in the range 115–800 nm (see above). Figure 1 shows the spectral energy distribution of the X-ray source XTE J1118+480 constructed from our photometry (open circles) and the average *V* photometric data (asterisks) from Cook *et al.* (2000). Dashed line *1* represents the $F(\lambda) \propto \lambda^{-2.3}$ relation normalized to the mean *J* flux. We extrapolated this relation to a wavelength of 0.15 μm (150 nm) and plotted the flux from Haswell *et al.* (2000a, 2000b) for it (asterisks). Thus, at 1.25–1.65 μm, we most likely see the same source that was observed by Haswell *et al.* (2000a, 2000b) in the range 0.115–0.8 μm (115–800 nm) and who associated it with a viscous accretion disk. If we now subtract the contribution of the accretion disk from the observed IR fluxes, then the energy distribution of the excess 1.65–3.5-μm radiation can be fitted by blackbody emission at a temperature of ~900 K (dotted line *2* in Fig. 1). The solid line in Fig. 1 represents a sum of the emissions from the above two sources in the range 1.25–3.5 μm. Thus, the mean spectral energy distribution of the X-ray nova XTE J1118+480 observed in April 2000 at 1.25–3.5 μm (with allowance for *V* photometry) can be represented (with errors no larger than 20% in flux) as a sum of the emissions from a source with $F(\lambda) \propto \lambda^{-2.3}$ and a blackbody at a temperature of ~900 K. Note that the 2.2–3.5-μm excess (and, consequently, the above estimates) depend only slightly on the classification of the first source (either a blackbody at ~4000 K or an accretion disk). Given the $F(\lambda) \propto \lambda^{-2.3}$ relation in the range 0.15–1.65 μm, the accretion-disk temperature is no less than $T_{ad} = 2 \times 10^4$ K.

The observed total flux from the hot source (accretion disk) emitting at 0.15–3.5 μm calculated by using the mean observed fluxes in this range is $F_{tot}^{ad} \geq \Sigma[F_{obs}(\lambda)\Delta\lambda] \approx 1.1 \times 10^{-9}$ erg s^{-1} cm^{-2}.

If a spherically symmetric dust envelope with neutrally absorbing grains heated to approximately 900 K surrounds the accretion disk and is in radiative equilibrium with it, then the radii of the heating source (R_{ad}) and the envelope (R_{dust}) are related by $(R_{dust}/R_{ad}) \approx 0.5(T_{ad}/T_{dust})^2 \approx 0.5\ (2 \times 10^4/900)^2 \approx 500$.

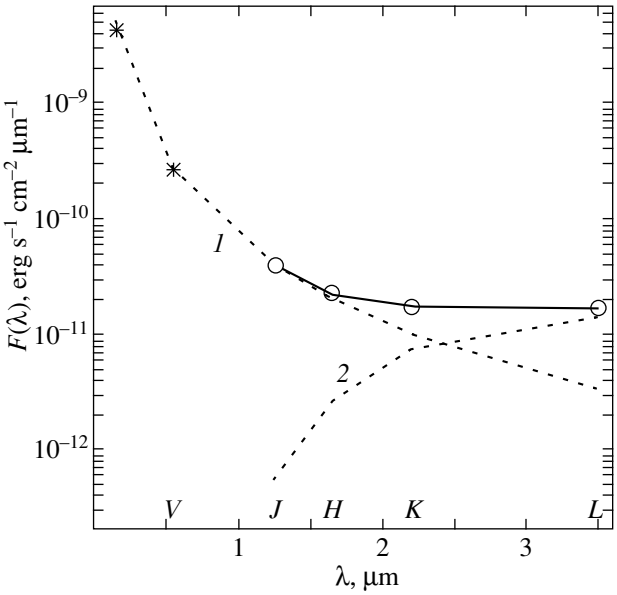

Fig. 1. Spectral energy distribution for the optical component of the X-ray binary XTE J1118+480. The open circles and asterisks represent, respectively, our averaged *JHKL* observations and the data from Cook *et al.* (2000) and Haswell *et al.* (2000a, 2000b). For an explanation of curves *1* and *2*, see the text.

The mean optical depth of the dust envelope for the accretion-disk radiation is $\tau \sim -\ln[(F_{tot}^{ad} - F_{tot}^{dust})/F_{tot}^{ad}] \sim 0.06$.

The angular size of such a dust envelope with neutrally absorbing grains is $\theta_{dust} = R_{dust}/r = [F_{tot}^{dust}/\sigma T_{source}^4 0.06]^{0.5}$.

The angular size of the accretion disk is $\theta_{ad} = R_{ad}/r = [F_{tot}^{ad}/\sigma T_{ad}^4]^{0.5} \sim 1.1 \times 10^{-11}$ rad, and the ratio of the radii of the dust envelope and the accretion disk that follows from a comparison of their angular sizes is ~500, i.e., matches the above estimate.

Our estimate of the total flux from the dust envelope enables us to roughly estimate the distance to the X-ray nova. Since the radii of circumstellar dust envelopes are generally no less than $(1–5) \times 10^{13}$ cm, we may write $r \geq R_{dust}/\theta_{dust} \approx (1–5) \times 10^{13}/5.6 \times 10^{-9} \approx (1.8–8.9) \times 10^{21}$ cm ≈ (0.6–3) kpc.

Table 2 lists some of the parameters for the sources of the X-ray nova XTE J1118+480 visible in the range 1.25–3.5 μm estimated above, as well as the sources'

Table 2. Parameters for the sources of the X-ray binary XTE J1118+480 emitting at 1.25–3.5 μm

Source	F_{tot}, 10^{-11} erg s^{-1} cm^{-2}	T, K	θ, 10^{-11} rad	r = 2 kpc	
				$L/L_\odot$	$R/R_\odot$
Accretion disk	110	≥20000	~11	~140	~3–14
Dust envelope (τ ~ 0.06)	7	~900	~560	~90	~140–720

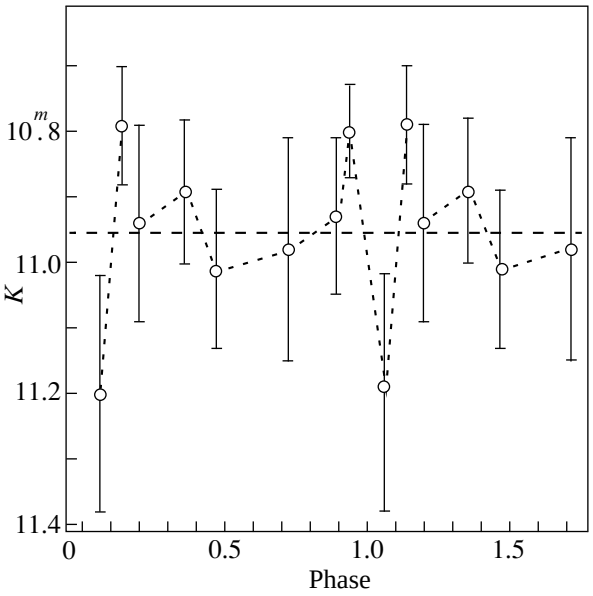

Fig. 2. *K* photometry folded with a 0.1706-day period. The initial epoch is JD 2 451 600. The horizontal line represents the mean *K* magnitude. The vertical bars indicate the standard errors.

luminosities and sizes (for the distance to the binary of $r = 2$ kpc).

Figure 2 shows our *K*-band (2.2 μm) observations folded with an optical period of $0^d.1706$ and the initial epoch JD 2 451 600. The vertical bars indicate standard errors, and the dashed line represents the mean observed *K* magnitude. We see from the Fig. 2 that the *K*-brightness variations with the 0.17-day period are within the photometric error limits.

CONCLUSION

Our analysis of the *JHKL* photometry for the X-ray binary XTE J1118+480 leads us to the following preliminary conclusions:

—The binary's 1.65- to 3.5-μm radiation exhibits a significant IR excess, which may be due to the thermal radiation from a dust envelope/cloud.

—The source observed at 1.25–1.65 μm is most likely the same as that at 0.115–0.8 μm (115–800 nm)—an accretion disk (Haswell *et al.* 2000a, 2000b).

—The distance to the X-ray binary estimated from the observed total flux from the dust envelope is ~(0.6–3) kpc.

—The mean optical depth of the dust envelope for the accretion-disk radiation is ~0.06.

ACKNOWLEDGMENTS

This study was supported in part by the Russian Foundation for Basic Research (project no. 00-02-16 272) and the State Science and Technology Program "Astronomy." We are grateful to the referees for helpful remarks.

REFERENCES

1. D. A. Allen and J. P. Swings, Astrophys. J., Lett. Ed. **10**, L83 (1972).
2. L. Cook, J. Patterson, D. Buczynski, and R. Fried, IAU Circ., No. 7397 (2000).
3. M. García, W. Brown, M. Pahre, and J. McClintock, IAU Circ., No. 7392 (2000).
4. C. A. Haswell, D. Skillman, J. Patterson, *et al.*, IAU Circ., No. 7407 (2000a).
5. C. A. Haswell, D. Skillman, J. Patterson, *et al.*, IAU Circ., No. 7427 (2000b).
6. H. L. Johnson, R. I. Mitchel, B. Iriarte, and W. Z. Wisniewski, Commun. Lunar Planet. Lab. **4**, 99 (1966).
7. J. Koornneef, Astron. Astrophys. **128**, 84 (1983).
8. C. Mauche, R. Hynes, P. Charles, and C. Haswell, IAU Circ., No. 7401 (2000).
9. R. Remillard, E. Morgan, D. Smith, and E. Smith, IAU Circ., No. 7389 (2000).
10. O. G. Taranova and V. I. Shenavrin, IAU Circ., No. 7407 (2000).
11. M. Uemura, T. Kato, and H. Yamaoka, IAU Circ., No. 7390 (2000).

Translated by N. Samus'

Astronomy Letters, Vol. 27, No. 1, 2001, pp. 29–33. Translated from Pis'ma v Astronomicheskiĭ Zhurnal, Vol. 27, No. 1, 2001, pp. 36–41.

Flare Activity and an Optical Superflare of the X-ray Object 1RXS J220111+281849

V. M. Batyrshinova and M. A. Ibragimov*

Ulugbek Astronomical Institute, Academy of Sciences of Uzbekistan, Astronomicheskaya ul. 33, Tashkent, 700052 Uzbekistan

Received January 18, 2000; in final form, June 16, 2000

Abstract—A *UBVR* monitoring of the X-ray source 1RXS J220111+281849 was performed during August 2–21, 1999. Seven moderately intense ultraviolet flares with 1–3^m amplitudes were detected. The object exhibits both rapid and slow flares. An unusual superintense flare with an $11\overset{m}{.}0$ amplitude in *U* was detected on August 18, 1999. Light curves of the flares are presented, and their physical parameters are briefly analyzed.
© 2001 MAIK "Nauka/Interperiodica".

Key words: *X-ray and gamma-ray sources*

INTRODUCTION

The X-ray object 1RXS J220111+281849 was discovered during ROSAT observations (Bade *et al.* 1998). It was identified with a 12^m M4 star whose distance is 9 pc.

The first CCD optical *R* observations of the object were carried by Greimel and Robb (1998). They detected periodic light variations with a $0\overset{m}{.}02$ amplitude and a $0\overset{d}{.}448$ period. The star's flare activity was established from the same observations: six *R*-band flares with amplitudes no larger than $0\overset{m}{.}3$ were detected during four nights. Surprisingly, some flares recurred with a $0\overset{d}{.}442$ period, which, as noted by the authors, was intriguingly close to the photometric period. In order to test the hypothesis of a periodic nature of flares, Greimel and Robb proposed to perform an international monitoring of this star in August 1999.

A monitoring with the participation of six observatories from South Korea, Uzbekistan, Armenia, Denmark, and Canada was carried out on August 16–20, 1999. Spectroscopic and photometric results of the monitoring are currently being analyzed and prepared for publication. Here, we report the most interesting photometric results that we obtained during August 2–21, 1999.

OBSERVATIONS

The observations were carried out during 14 nights from August 2 through 21, 1999, at the Maidanak Observatory of the Astronomical Institute (Academy of Sciences of Uzbekistan). We used a single-channel pulse-counting *UBVR* photometer attached to the 0.6-m Zeiss telescope (Shevchenko 1989). The integration time was 10 s. The comparison star was GSC 2215–1776, and the check star was GSC 2215–1761 = SAO 90180 (the GSC numbers were taken from Jenkner *et al.* 1990). The magnitudes and colors of these stars that we determined by referencing to three standard stars, BD+43°3781 and N269 from SA113 and N473 from SA114 (Landolt 1992), are listed in the table. The referencing was made during June 24–August 9, 1999, by using the above instrumentation. Column 2 of the table

Magnitudes and colors of the comparison star GCS 2215–1776 and the check star GSC 2215–1761

	N	Min	Max	Mean	RMS
GSC 2215–1776					
U	45	$11\overset{m}{.}933$	$11\overset{m}{.}792$	$11\overset{m}{.}856$	$0\overset{m}{.}032$
B	46	11.580	11.475	11.532	0.020
V	46	10.853	10.798	10.823	0.012
R	46	10.263	10.205	10.237	0.014
U–B	45	0.384	0.280	0.324	0.025
B–V	46	0.741	0.668	0.709	0.014
V–R	46	0.607	0.552	0.586	0.011
GSC 2215–1761					
U	44	$11\overset{m}{.}237$	$11\overset{m}{.}080$	$11\overset{m}{.}141$	$0\overset{m}{.}033$
B	45	10.300	10.190	10.246	0.022
V	45	9.209	9.154	9.178	0.014
R	45	8.372	8.299	8.335	0.015
U–B	44	0.940	0.856	0.895	0.021
B–V	45	1.096	1.035	1.068	0.013
V–R	45	0.869	0.823	0.843	0.009

* E-mail address for contacts: mansur@astrin.uzsci.net

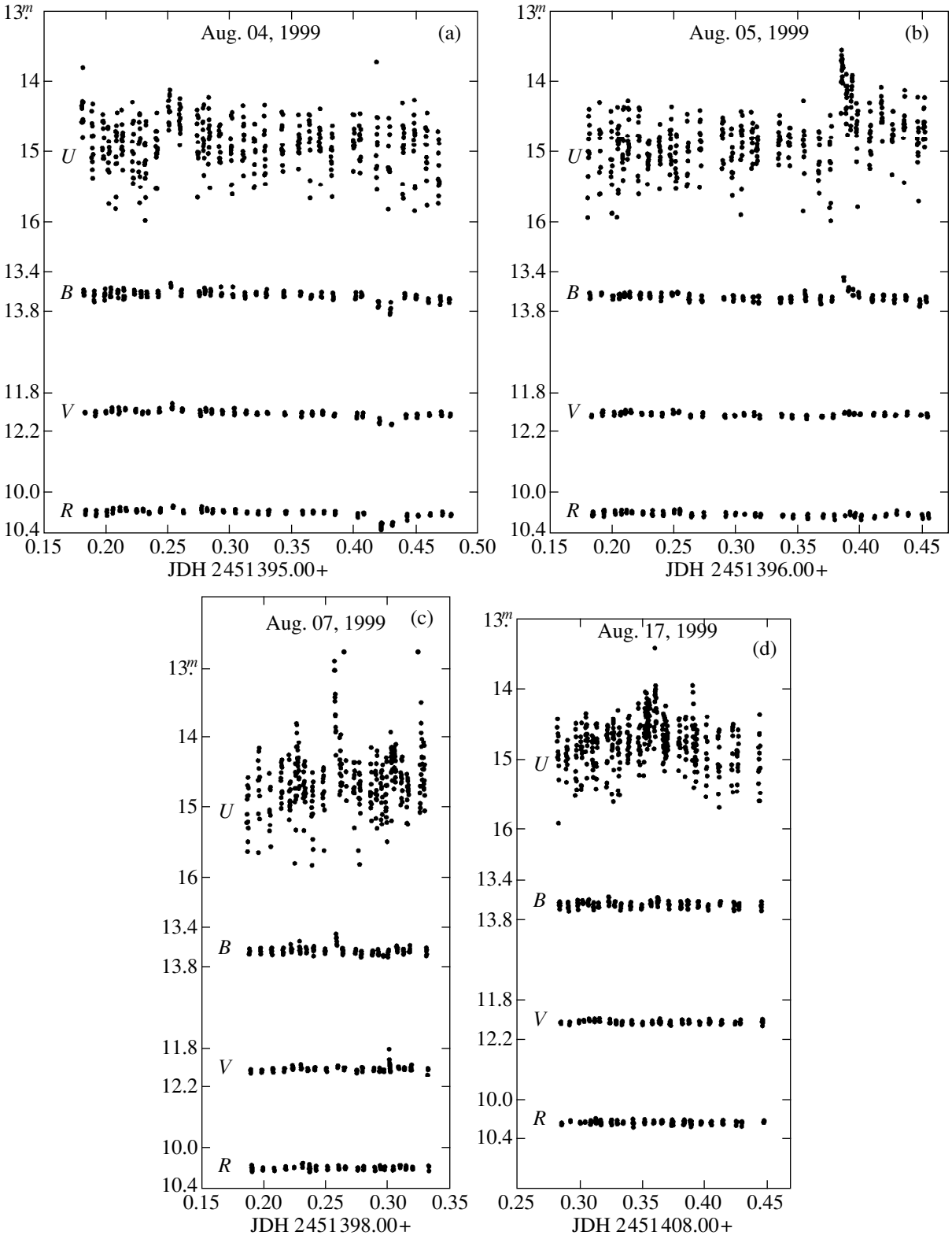

Fig. 1. *UBVR* light curves of 1RXS J220111+281849 for six dates in August 1999.

gives the number of measurements in each band; columns 3 to 5 list minimum, maximum, and mean magnitudes and colors, respectively. Rms deviations of the means are given in the last column.

When observing the object, we commonly used the following sequence of measurements: two minutes in *U*, one minute in each of the *B* and *V* bands, and 50 s in *R*. Every hour or one and a half hour, we measured

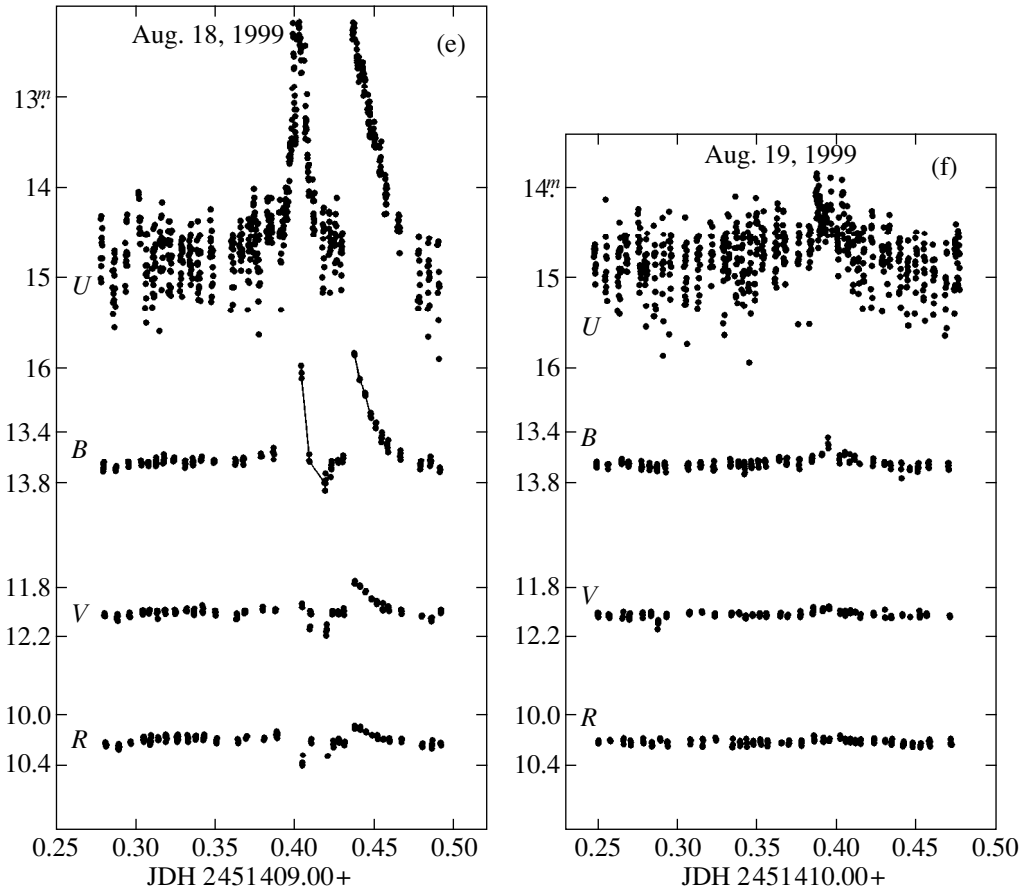

Fig. 1. (Contd.)

the comparison and check stars. The frequency of sky-background measurement varied in the range 10–30 min, depending on the Moon's phase. We did not measure the extinction and used August-averaged extinction values. When constructing the light curves, we plotted each 10-s measurement as a separate observation. According to our observations, the magnitude difference between U ($14\overset{m}{.}8$) and R ($10\overset{m}{.}2$) for this M4 star is $4\overset{m}{.}6$, implying that the red flux exceeds the ultraviolet flux by almost a factor of 70. Since the mean energy of an optical photon (several eV) does not change considerably from the ultraviolet to the red, the star can be assumed to supply two orders of magnitude more optical photons in the red than it does in the ultraviolet. This fact has a major effect on the 3σ range of scatter in data points for the star's light curves in different bands. According to Poisson statistics, the expected scatter in U is an order of magnitude larger than that in R. We estimated the scatter to be $0\overset{m}{.}9$ for U, $0\overset{m}{.}1$ for B, and $0\overset{m}{.}04$–$0\overset{m}{.}06$ for V and R. These estimates were made in the star's quiescent (out-of-flare) state. In doing so, we disregarded the natural photometric variability of the star, which, according to the R-band estimates of Greimel and Robb (1998) and our BVR estimates, does not exceed $0\overset{m}{.}02$. The out-of-flare U variability defies estimation, and, based on our observations, we can only conclude that, if exists, it does not exceed $0\overset{m}{.}3$.

On August 2–21, we carried out two separate series of observations: the preparatory and main ones. The preparatory series spanned eight nights on August 2–9. The main series, which was performed as part of the star's international monitoring, spanned six nights on August 16–21.

DISCUSSION

Parameters of Typical Flares

The star exhibited a noticeable activity (mainly in U) during both series of observations. Flares were difficult to detect, because the star was faint in U ($14\overset{m}{.}8 \pm 0\overset{m}{.}3$). Seven reliable and about ten presumed flares were detected during 14 observing nights in U. Flares whose amplitudes exceeded the 3σ range of Poisson scatter in data points were reckoned to be reliable. In order to demonstrate the optical behavior of the X-ray source,

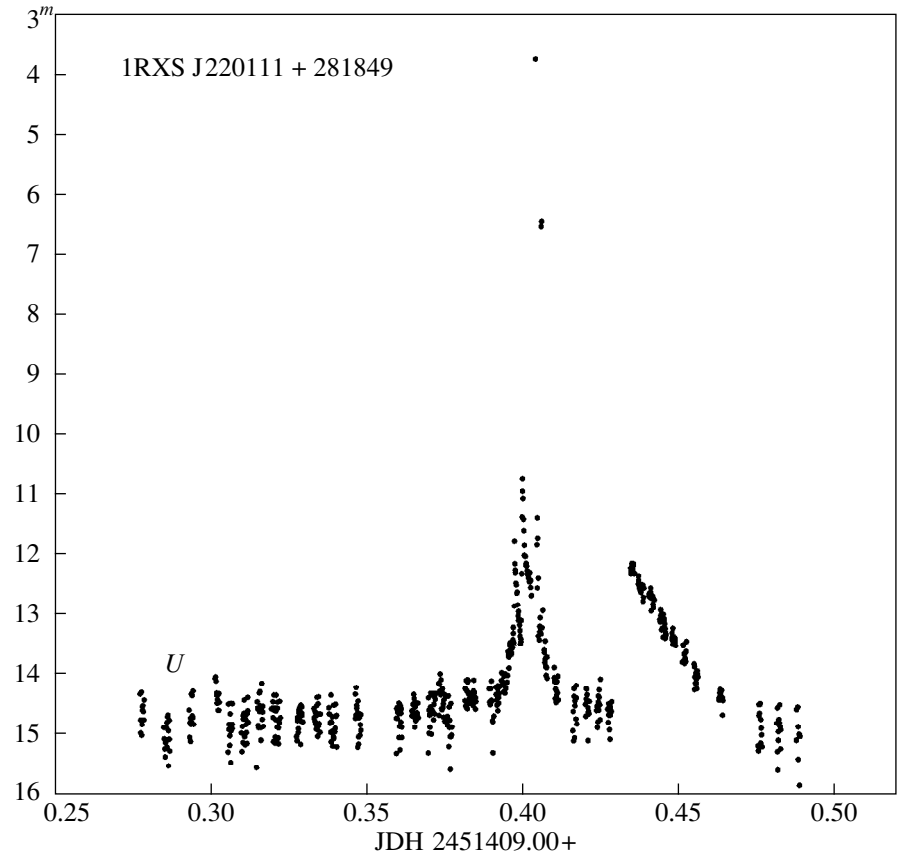

Fig. 2. *U* light curve of 1RXS J220111+281849 on August 18, 1999 with two slow and two rapid large-amplitude flares.

we chose six observing nights (three nights in each of the two series) and presented them in Figs. 1a–1f.

A comparison of the light curves in Fig. 1 suggests that the star's flare activity is highly varied. The star undergoes both rapid and slow flares (for the flare classification, see, e.g., Gershberg 1970). The duration of the rapid flares on August 4, 5, and 7 ranges from 10 s (the August 4 flare by $1\overset{m}{.}1$) to 1–3 min (the August 5 and 7 flares). The duration of the detected slow flares is 28–45 min (the August 17, 18, and 19 flares). An analysis of the star's flare activity for periodicity based on our observations yielded no results: our 14-day-long data revealed no periodicity in the recurrence of flares in August 1999. We only note that the three slow flares we observed on August 17–19 occurred approximately at the same Julian intervals (about 23 h). However, these data are not enough to be a compelling argument for the periodic nature of flares on this star hypothesized by Greimel and Robb (1998).

The color behavior during flares is typical of flare red dwarfs (Gershberg 1970). The flares on August 5, 18, and 19 suggest a reduction in the flare amplitude at long wavelengths. The August 4 and 18 observations reveal a decline in *R* brightness by $0\overset{m}{.}1$–$0\overset{m}{.}2$ during a *U* flare.

The detected flares also differ in amplitude. According to our observations, the most typical amplitudes are 1–3^m in *U*. The star exhibited two *U* flares with $11\overset{m}{.}0$ and $8\overset{m}{.}3$ amplitudes on August 18, 1999.

The Optical Superflare on August 18, 1999

The most remarkable event during the star's international monitoring was its optical superflare, which we observed on August 18 at the Maidanak Observatory. Figures 1e and 2 show the star's light curves on this date. We had to truncate the *U* light curve in Fig. 1e on the magnitude scale to show the curves on the same scale. The *U* light curve in Fig 2 is shown in full.

Two slow flares with durations of 129 and 43 min and 2–3^m amplitudes are seen on the light curve. The first slow flare is composite in pattern and is a superposition of four shorter flares. The second slow flare is a monotonic fading after a single brightening.

Two separate, very intense flares were detected during the first slow flare. The amplitudes of the first and second flares reached a record $11\overset{m}{.}0$ and $8\overset{m}{.}3$, respectively. The maximum of the second strong flare is separated from the maximum of the first one by 2.5 min.

The peak state of the first and second flares lasted 10 and 20 s, respectively. The total duration of the strong flares is difficult to measure, because their light curves are superimposed on each other and because neighboring flares are superimposed on them.

Despite the short duration (10 s), the energy of the 11^m flare is unique among the observed flares and is of the order of 10^{35} erg. This value exceeds the mean energy of typical strong flares in flare stars of the solar neighborhood by several hundred times. The equivalent intensities for most of the observed strong flares are known to be no larger than several hours (see, e.g., Gurzadyan 1985). The equivalent intensity of the described flare is of the order of 10^6 s, or more than 10 days.

CONCLUSION

The photometric *UBVR* monitoring of the X-ray source 1RXS J220111+281849 during 14 nights on August 2–21, 1999, has confirmed its flare activity. The star exhibits both rapid and slow flares, which are characteristic of flare stars in the solar neighborhood. We have detected seven flares with amplitudes larger than 1^m in *U* and about ten lower-amplitude flares. The color behavior during the flares is typical of flare stars in the solar neighborhood. In two cases, we observed a decline in *R* brightness by $0\overset{m}{.}1$–$0\overset{m}{.}2$ during a *U* flare. Our observations revealed no presumed periodicity in the star's flare activity.

A record (in intensity) *U* flare with an $11\overset{m}{.}0$ amplitude was detected on August 18. The flare energy was of the order of 10^{35} erg, and its equivalent intensity was more than 10 days.

Our observations represent the first fairly complete photometric study of the optical behavior of this interesting X-ray source. There is no doubt that this object deserves a closer attention of flare-star researchers.

ACKNOWLEDGMENTS

We wish to thank Russell Robb (University of Victoria, Canada), the organizer and head of the object monitoring program, for help in preparing and conducting the monitoring and for useful discussions.

REFERENCES

1. N. Bade, D. Engels, W. Voges, *et al.*, Astron. Astrophys., Suppl. Ser. **127**, 145 (1998).
2. R. E. Gershberg, *Flares on Red Dwarf Stars* (Nauka, Moscow, 1970).
3. R. Greimel and R. M. Robb, Inf. Bull. Var. Stars, No. 4652 (1998).
4. G. A. Gurzadyan, *Stellar Flares: Physics. Cosmogony* (Nauka, Moscow, 1985).
5. H. Jenkner, B. Lasker, C. Sturch, *et al.*, Astron. J. **99**, 2082 (1990).
6. A. U. Landolt, Astron. J. **104**, 340 (1992).
7. V. S. Shevchenko, *Herbig Ae/Be Stars* (Fan, Tashkent, 1989).

Translated by V. Astakhov

Astronomy Letters, Vol. 27, No. 1, 2001, pp. 34–38. Translated from Pis'ma v Astronomicheskiĭ Zhurnal, Vol. 27, No. 1, 2001, pp. 42–46.

The Hβ and Hγ Lines in the Spectrum of V1057 Cyg

B. N. Rustamov*

Shemakha Astrophysical Observatory, Academy of Sciences of Azerbaĭjan, Shemakha, 373243 Azerbaĭjan

Received August 18, 1999; in final form, April 25, 2000

Abstract—We present the equivalent widths of the Hβ and Hγ absorption lines in the spectrum of V1057 Cyg measured from 1978–1990 spectrograms. The mean equivalent widths of these lines decreased approximately twofold during 1978–1985 and somewhat increased during 1987–1990. Using published *UBV* photometry, we show that there has been a correlation between the Hβ equivalent width and the $\langle U–B\rangle$ color since 1983, with $\langle W_\lambda(\mathrm{H}\beta)\rangle$ increasing with decreasing $\langle U–B\rangle$. Based on our spectroscopic and photometric observations in 1978–1990, we assume that V1057 Cyg has passed to a qualitatively new stage of its development after 1985.

Key words: *stars—variable and peculiar*

INTRODUCTION

The fact that V1057 Cyg had belonged to T Tauri stars before its brightness rise has ultimately confirmed that FU Ori stars (fuors) are genetically related to young stars. Therefore, studies of fuors with unusual physical properties are of great interest in investigating the early stages of stellar evolution. V1057 Cyg differs from other members of this group of objects by dynamic variations in its photometric and spectroscopic parameters. Spectroscopic observations of two fuors, FU Ori and V1057 Cyg, have been systematically carried out at the Shemakha Astrophysical Observatory (Academy of Sciences of Azerbaijan) since 1978 as part of a general program of research on T Tauri stars. Some of the results of these observations ware published previously (Rustamov 1980, 1986, 1989).

Here, we study the Hβ and Hγ lines in the spectra of V1057 Cyg taken from 1978 until 1990.

Before its brightness rise, V1057 Cyg was known as a faint variable star with m_{phg} within $15\overset{m}{.}5$–$16\overset{m}{.}5$ (Wenzel 1963), with a T Tau-type emission-line spectrum (Herbig 1958) and H_α emission (Haro 1971). Immediately after its optical flare, the H_α line had a P Cyg profile with a strong emission component; the latter noticeably weakened by the end of 1972 (Haro 1971; Gahm and Welin 1972; Herbig 1977), and the stellar emission component completely disappeared by 1974 (Kolotilov 1975). After the flare, the H_α absorption was blueshifted, suggesting its origin in an expanding circumstellar envelope. The H_α radial velocity decreased from –560 km s^{-1} in early 1971 to –200 to –300 km s^{-1}, on the average, in 1975 (Herbig 1977); in 1976–1982, it was, on average, –200 to –300 km s^{-1} (Kolotilov 1983).

OBSERVATIONS

Our 3690–5100 Å spectra of V1057 Cyg were obtained at the Cassegrain focus of the 2-m Shemakha Observatory telescope using a 2×2 prism spectrograph with a dispersion of 93 Å mm^{-1} near Hγ. During 1978–1990, we took 71 spectrograms. On each night, the spectra of V1057 Cyg and comparison star "c" (Meinunger and Wenzel 1971) were photographed on the same Kodak 103aO plate and developed in an MWP-2 developer together with the image scale of a step attenuator photographed with the ISP-5 laboratory spectrograph. The exposure time for spectra widened to 0.2 mm changed from 1 hour in 1978 to 9 hours in 1990, depending on the star's brightness and seeing. The star's *B* brightness declined in this time from $12\overset{m}{.}6$ to $13\overset{m}{.}4$ (Kolotilov 1990; Herbst *et al.* 1994). All spectrograms were traced in darkenings near Hβ and Hγ using the Lirepho microphotometer with a magnification of about 100. To transform darkenings to intensities, characteristic curves were constructed for each observing night.

RESULTS

The characteristic curves were used to construct the line profiles in units of continuum intensity. Figure 1 shows sample profiles of the Hβ absorption line in the spectrum of V1057 Cyg. Based on all the available spectrograms, we measured the following parameters of the Hβ and Hγ absorption profiles: equivalent width W_λ, FWHM $\Delta\lambda_{1/2}$, and line depth *R*. The entire period of our observations can be divided into nine observing sea-

* E-mail address for contacts: shao@lan.al.az

sons. Season-averaged values of the measured parameters are given in Table 1, where *n* is the number of spectrograms being averaged. Table 1 also lists the mean spectral types of V1057 Cyg determined from its absorption spectrum in the blue spectral range using our criteria developed for the spectrograph in question (Rustamov 1987).

Our spectrograms do not show any systematic changes in Hβ an Hγ radial velocities; on average, they are –150 and –90 km s^{-1} for Hβ and Hγ, respectively.

Based on published photometry (Kolotilov 1990) and on an electronic database (Herbst *et al.* 1994), we compiled Table 2, which lists mean magnitudes $\langle B\rangle$ and colors $\langle B–V\rangle$ and $\langle U–B\rangle$ for the period of our spectroscopic observations. The number of averaged measurements is given in parentheses.

Figure 2 shows temporal variations in the Hβ absorption equivalent width and $\langle U–B\rangle$ color of V1057 Cyg during 1978–1990. The temporal variations in Hγ equivalent width are synchronous with those of Hβ (see Table 1).

DISCUSSION

During 1978–1985, the equivalent widths of the Hβ and Hγ lines decreased approximately by a factor of 2. No observations were performed in 1986, while in 1987, the Hβ equivalent width increased compared to 1985, and its growth had continued until 1990. The variations in Hβ and Hγ equivalent widths were mainly caused by variations in line depths (see Table 1 and Fig. 2).

As we see from Fig. 2, the variations in Hβ absorption equivalent width have correlated with the $\langle U–B\rangle$ color index since 1983; i.e., $\langle W_\lambda(\mathrm{H}\beta)\rangle$ increases with UV excess (with decreasing $\langle U–B\rangle$). The correlation between $\langle W_\lambda(\mathrm{H}\beta)\rangle$ and $\langle U–B\rangle$ variations indicates that $\langle W_\lambda(\mathrm{H}\beta)\rangle$ began to increase in 1986.

The published data on Balmer line profiles in the spectrum of V1057 Cyg for 1978–1990 refer mainly to the H_α line (see, e.g., Ulrich and Knapp 1979; Kolotilov 1983; Bastian and Mundt 1985; Crosswell *et al.* 1987), whereas Welty *et al.* (1992) and Hartmann and Calvet (1995) also provided Hβ profiles. The H_α line in the spectrum of V1057 Cyg shows a P Cyg profile with a very weak, broad emission component in the red wing and a blueshifted absorption component.

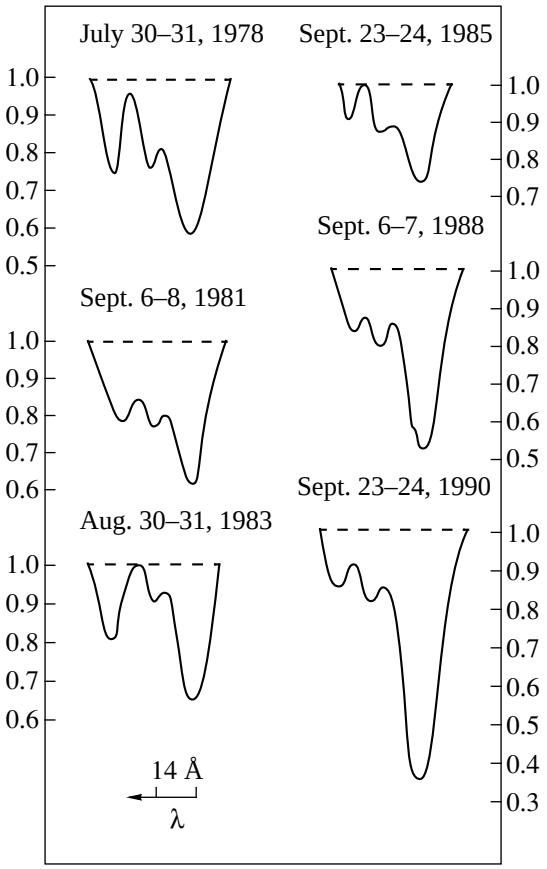

Fig. 1. Profiles of the Hβ absorption line in the spectrum of V1057 Cyg. The profiles are in units of continuum intensity. The scale along the *x* axis is the same for all profiles and is indicated by a horizontal bar.

Table 1. Behavior of the Hβ and Hγ lines in the spectrum of V1057 Cyg

Season	Hβ				Hγ				Sp
	W_λ, Å	$\Delta\lambda_{1/2}$, Å	*R*	*n*	W_λ, Å	$\Delta\lambda_{1/2}$, Å	*R*	*n*	
July–August 1978	6.6 ± 0.28	12.8 ± 0.4	0.52 ± 0.02	28	4.5 ± 0.2	7.8 ± 0.3	0.58 ± 0.01	21	G2
June 1979	6.2 ± 0.74	13.4 ± 0.5	0.48 ± 0.04	3	4.3 ± 0.1	6.8 ± 0.3	0.65 ± 0.02	3	G3
August–November 1981	5.6 ± 0.4	15.3 ± 0.8	0.37 ± 0.02	25	3.1 ± 0.2	6.4 ± 0.2	0.47 ± 0.01	22	G5
August–November 1983	4.2 ± 0.5	12.5 ± 1.5	0.35 ± 0.02	7	2.1 ± 0.2	6.4 ± 0.5	0.34 ± 0.03	7	G0
September 1985	3.3 ± 0.3	12.5 ± 0.3	0.27 ± 0.01	2	1.9 ± 0.4	5.1 ± 0.0	0.37 ± 0.05	2	G2
September 1987	5.6	15.3	0.35	1					
September 1988	6.3 ± 0.7	14.2 ± 0.3	0.45 ± 0.03	2	4.1 ± 0.2	8.6 ± 0.3	0.47 ± 0.02	2	G7
August 1989	8.3	13.2	0.63	1	5.5	8.3	0.7	1	G5
September 1990	9.3 ± 0.3	13.9 ± 0.0	0.65 ± 0.01	2	4.5 ± 0.4	9.7 ± 0.4	0.47 ± 0.01	2	G5

Note: FWHM $\Delta\lambda_{1/2}$ of the instrumental profile is approximately 5 Å and 3 Å for Hβ and Hγ, respectively.

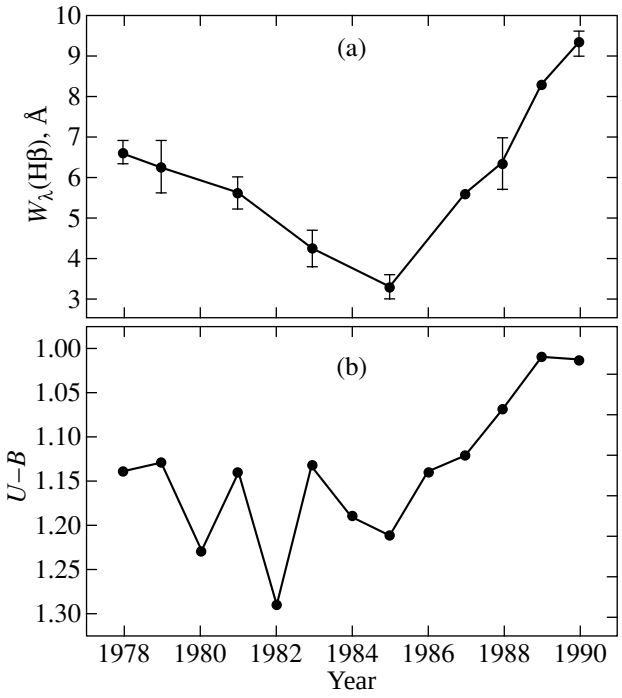

Fig. 2. Time variations in Hβ absorption equivalent width (a) and in *U–B* color index (b) for V1057 Cyg in 1978–1990.

Although the general appearance of the H_α profile in 1978–1984 is, on the whole, preserved, the H_α absorption exhibits significant variability (Ulrich and Knapp 1979; Bastian and Mundt 1985; Crosswell *et al.* 1987). In November 1985, Crosswell *et al.* (1987) observed a relatively strong and narrow emission in the H_α red wing compared to 1981–1982 (Bastian and Mundt 1985). In 1988, Welty *et al.* (1992) observed a very broad H_α absorption in the spectrum of V1057 Cyg whose violet edge reached –800 km s^{-1}, with the emission in the red wing being enhanced. Concurrently, an emission was also observed in the Hβ red wing.

During 1978–1985, V1057 Cyg faded by $0\overset{m}{.}8$ in *B*. In 1985–1990, the *B* brightness and the $\langle B–V\rangle$ color index were essentially constant, while $\langle U–B\rangle$, which increased after the flare, has generally decreased since 1985 (see Table 2).

Analyzing long-term IR photometry for 1976–1988, Kolotilov (1990) described the infrared behavior of V1057 Cyg in detail. In particular, he established the following: (1) the 1–25-μm brightness of V1057 Cyg declined after the fuor flare, but this process seized in 1984; and (2) the fluxes in the 3.5-, 5-, and 10-μm bands have dropped appreciably after 1984.

From June through December 1984, Ibragimov and Shevchenko (1987) observed a local brightness rise in V1057 Cyg with a $0\overset{m}{.}1$ amplitude and a duration of 100–150 days.

Thus, the above observational results apparently indicate that, approximately in 1984–1985, V1057 Cyg passed to a qualitatively new physical state, because the trend of variations in spectroscopic and photometric parameters has changed sharply since that time. As was noted above, the variations in Hβ absorption has correlated well with the $\langle U–B\rangle$ variations since 1983.

In recent years, the fuor phenomenon has been predominantly interpreted in terms of the disk accretion theory. This theory assumes the presence of protostellar accretion disks around these objects (see, e.g., Kenyon *et al.* 1988; Welty *et al.* 1992). Fuor flares can be explained by a significant increase in accretion rate from ~10^{-7} $M_\odot$ yr^{-1} to ~10^{-4} $M_\odot$ yr^{-1}. According to the theory, the UV excess arises from the boundary layer between the accretion disk and the star, where the accreting-gas energy is generated. The P Cyg profiles, suggesting mass outflow, originate in the hot region immediately behind the accretion shock front (in the inner part of the disk). The variability of mass outflow and of the UV excess is attributable to unsteady accretion (Lin and Papaloizou 1985; Clarke *et al.* 1989). Various kinds of variability can result from nonradiative processes produced by magnetohydrodynamic interactions between the boundary layer and the star's outer layers.

The correlation between $\langle W_\lambda(H\beta)\rangle$ and $\langle U–B\rangle$ for the fuor V1057 Cyg appears to be in qualitatively good agreement with this model.

Note that, for the YY Ori star S CrA, Mundt (Bertout and Yorke 1982) obtained a similar result for the equivalent widths of redshifted absorption components in the Balmer lines. For interpreting the phenomena characteristic of YY Ori stars, the disk accretion model can be considered to be universally accepted (Herbst *et al.* 1994).

Without going into details, we note that, although this theory describes well many peculiarities of fuors, there are still a number of serious objections (Simon and Joyce 1988; Petrov and Herbig 1992).

The earlier observations by Simon *et al.* (1972, 1975) revealed that the near-infrared energy distribution in V1057 Cyg agreed well with a model that assumed a substantial contribution of free–free emission from the gas envelope. However, this model was rejected as being in conflict with optical observations because of the absence of an UV excess.

Rodriguez and Hartmann (1992) detected free–free emission in the 3-cm radio spectrum of V1057 Cyg, suggesting strong ionization of the outflowing matter.

As was noted above, the UV excess in V1057 Cyg has increased since 1985. It is probably due to the hydrogen emission during free–free transitions. Two possible sources of the IR excess in T Tauri stars are discussed: thermal dust radiation (see, e.g., Mendoza 1968; Cohen 1973) and hot-gas emission during free–bound and free–free transitions (Rydgren *et al.* 1976).

Table 2. Photometric behavior of V1057 Cyg in 1978–1990

Year of observations	$\langle B \rangle$	$\langle B–V \rangle$	$\langle U–B \rangle$	Data source
1978	12.56 (19)	1.67 (19)	1.14 (19)	Kolotilov (1990)
1979	12.70 (19)	1.72 (19)	1.13 (17)	Kolotilov (1990)
1980	12.88 (14)	1.75 (14)	1.23 (14)	Kolotilov (1990)
1981	13.05 (13)	1.79 (13)	1.14 (13)	Kolotilov (1990)
1982	13.26 (22)	1.82 (22)	1.29 (22)	Kolotilov (1990)
1983	13.24 (31)	1.76 (31)	1.16 (30)	Kolotilov (1990)
	13.14 (19)	1.72 (19)	1.13 (19)	Herbst *et al*. (1994)
1984	13.31 (21)	1.77 (21)	1.18 (21)	Kolotilov (1990)
	13.25 (68)	1.74 (68)	1.19 (68)	Herbst *et al*. (1994)
1985	13.35 (17)	1.76 (17)	1.11 (17)	Kolotilov (1990)
	13.36 (17)	1.75 (17)	1.21 (17)	Herbst *et al*. (1994)
1986	13.39 (18)	1.79 (18)	1.04 (15)	Kolotilov (1990)
	13.35 (103)	1.75 (103)	1.14 (103)	Herbst *et al*. (1994)
1987	13.34 (5)	1.78 (5)	1.12 (5)	Kolotilov (1990)
	13.31 (114)	1.75 (114)	1.12 (114)	Herbst *et al*. (1994)
1988	13.28 (7)	1.75 (7)	0.92 (5)	Kolotilov (1990)
	13.31 (139)	1.76 (139)	1.07 (139)	Herbst *et al*. (1994)
1989	13.32 (139)	1.75 (139)	1.01 (139)	Herbst *et al*. (1994)
1990	13.34 (128)	1.76 (128)	1.01 (128)	Herbst *et al*. (1994)

In 1983, Kolotilov (1990) found humps on the IR light curve of V1057 Cyg in the *L* and *M* bands. Since there is an anticorrelation between the visual and infrared light variations, he explains this fact by the appearance of a dust envelope around the star. In the case of a hot gas envelope, we would have obtained a correlation.

The ambiguous behavior of the IR excess in V1057 Cyg at different wavelengths noted by different authors (see, e.g., Herbig 1977) partly stems from the fact that different mechanisms dominate at different wavelengths. Rydgren (1982) points out that the radiation models for a hot gas and an optically thick or thin dust are not alternative. Both these mechanisms are involved in the radiation of Herbig Ae/Be stars, with different mechanisms dominating at different wavelengths. Note that the behavior of the $\langle U–B \rangle$ color index for V1057 Cyg in 1978–1985 was also ambiguous (Fig. 1).

Apart from the equilibrium photospheric component, the gas component apparently begins to show up in the color variations in 1983–1984, which is responsible for the enhancement of the variable H_α emission (Crosswell *et al.* 1987). The relative weakness of the H_α emission suggests that the volume of its formation is small.

A possible source that determines instability of the gas–dust envelope and that does not affect the photometric variability of V1057 Cyg is an active region on the stellar surface.

REFERENCES

1. U. Bastian and R. Mundt, Astron. Astrophys. **144**, 57 (1985).
2. C. Bertout and H. W. Yorke, in *Protostars and Planets*, Ed. by T. Gehrels (Univ. of Arisona Press, Tucson, 1978; Mir, Moscow, 1982).
3. C. J. Clarke, D. N. C. Lin, and J. C. B. Papaloizou, Mon. Not. R. Astron. Soc. **236**, 495 (1989).
4. V. Cohen, Mon. Not. R. Astron. Soc. **164**, 395 (1973).
5. K. Crosswell, L. W. Hartmann, and E. H. Avrett, Astrophys. J. **312**, 227 (1987).
6. G. Gahm and G. Welin, Inf. Bull. Var. Stars, No. 741, 1 (1972).
7. G. Haro, Inf. Bull. Var. Stars, No. 565, 1 (1971).
8. L. Hartmann and N. Calvet, Astron. J. **109**, 1846 (1995).
9. G. H. Herbig, Astrophys. J. **128**, 259 (1958).
10. G. H. Herbig, Astrophys. J. **217**, 693 (1977).
11. W. Herbst, D. K. Herbst, E. J. Grossman, and D. Weinstein, Astron. J. **108**, 1906 (1994).
12. M. A. Ibragimov and V. S. Shevchenko, Astrofizika **27**, 5 (1987).
13. S. J. Kenyon, L. Hartmann, and R. Hewett, Astrophys. J. **325**, 231 (1988).
14. E. A. Kolotilov, Astron. Tsirk., No. 873, 4 (1975).
15. E. A. Kolotilov, Pis'ma Astron. Zh. **9**, 622 (1983) [Sov. Astron. Lett. **9**, 324 (1983)].
16. E. A. Kolotilov, Pis'ma Astron. Zh. **16**, 24 (1990) [Sov. Astron. Lett. **16**, 12 (1990)].
17. D. N. C. Lin and J. Papaloizou, in *Protostars and Planets*, Ed. by D. C. Black and M. S. Matthews (Univ. Ariz. Press, Tucson, 1985), Vol. II, p. 981.

18. L. Meinunger and W. Wenzel, Mitt. Ver. Sterne, No. 9, 170 (1971).
19. V. E. E. Mendoza, Astrophys. J. **151**, 977 (1968).
20. P. P. Petrov and G. H. Herbig, Astrophys. J. **392**, 209 (1992).
21. L. F. Rodríguez and L. Hartmann, Rev. Mex. Astron. Astrofis. **24**, 135 (1992).
22. B. N. Rustamov, in *Flare Stars, FU Ori Stars, and Herbig–Haro Objects*, Ed. by L. V. Mirzoyan (Akad. Nauk Arm. SSR, Yerevan, 1980), p. 211.
23. B. N. Rustamov, in *Flare Stars and Related Objects*, Ed. by L. V. Mirzoyan (Akad. Nauk Arm. SSR, Yerevan, 1986), p. 254.
24. B. N. Rustamov, Kinematika Fiz. Nebesnykh Tel **3** (2), 15 (1987).
25. B. N. Rustamov, Astron. Tsirk., No. 1540, 15 (1989).
26. A. E. Rydgren, in *Protostars and Planets*, Ed. by T. Gehrels (Univ. of Arisona Press, Tucson, 1978; Mir, Moscow, 1982).
27. A. E. Rydgren, S. E. Strom, and K. M. Strom, Astrophys. J., Suppl. Ser. **30**, 307 (1976).
28. T. Simon, Publ. Astron. Soc. Pac. **87**, 317 (1975).
29. T. Simon and R. R. Joyce, Publ. Astron. Soc. Pac. **100**, 1549 (1988).
30. T. Simon, N. D. Morrison, S. C. Wolf, and D. Morrison, Astron. Astrophys. **20**, 99 (1972).
31. R. K. Ulrich and G. R. Knapp, Astrophys. J. Lett. **230**, L99 (1979).
32. A. D. Welty, S. E. Strom, S. Edwards, *et al.*, Astrophys. J. **397**, 260 (1992).
33. W. Wenzel, Mitt. Ver. Sterne, No. 730 (1963).

Translated by N. Samus'

Astronomy Letters, Vol. 27, No. 1, 2001, pp. 39–50. Translated from Pis'ma v Astronomicheskiĭ Zhurnal, Vol. 27, No. 1, 2001, pp. 47–60.

Long-Term Cyclicity of the Herbig Ae Star BF Ori: Giant Protocomets and Accretion from a Protoplanetary Disk

V. S. Shevchenko† and O. V. Ezhkova*

Astronomical Institute, Academy of Sciences of Uzbekistan, Astronomicheskaya ul. 33, Tashkent, 700052 Uzbekistan

Received May 11, 1999; in final form, March 30, 2000

Abstract—Having analyzed the light curve for the Herbig Ae star BF Ori, we justify the hypothesis of a giant protocomet, GPC I BF Ori, with a period of 6.3 years and semimajor axis $a = 10 \pm 3$ AU. Passing through periastron, such a giant protocomet partially breaks up. During each passage through periastron, the protocomet and the fragments that follow it supply dust to circumstellar space for a certain period of time. This hypothesis can account for the entire complex of observable phenomena of cyclic Algol-like activity in Herbig Ae/Be and T Tauri stars. Conditions in a protoplanetary disk after cocoon breakup are discussed. We adduce arguments for the absence of a dust disk and for the weak effect of objects other than comets on cyclic large-scale variability.

Key words: *stars—variable and peculiar; Solar system—planets, comets, asteroids, heliosphere*

INTRODUCTION

Our long-term program of photometric and spectroscopic studies of Herbig Ae/Be, T Tau, and FU Ori stars, as well as related objects, has revealed periodic, cyclic, and quasi-cyclic phenomena with periods from several years to several days (Shevchenko 1989; Shevchenko *et al.* 1993a, 1993b, 1993c, 1994). An analysis of such phenomena has made it possible to develop a model of a star at the initial stage of its evolution, when the star, planets, and other bodies continue to form in the circumstellar disk.

We gave enough examples where long-term cyclicity with characteristic Algol-like fadings was clearly seen both in Herbig Ae/Be stars and in some bright T Tau stars (Shevchenko 1989; Shevchenko *et al.* 1994; Herbst and Shevchenko 1999). The same mechanism of long-term cyclicity is likely to exist in such cases. Using BF Ori as an example, we made an attempt to show that the model of unsteady and quasi-cyclic accretion from a flat protoplanetary disk onto a star was realistic. Large, proto-Jupiter-type bodies with elliptical orbits, which we called giant protocomets (GPCs), play a major role in this kind of accretion.

We do not focus on the various models that, in general, describe one or more observational manifestations without touching on the remaining ones (see, e.g., Hillenbrand *et al.* 1992; Hartmann and Calvet 1995; Sa *et al.* 1986). Such models are both a basis and a good complement to more fundamental ones. Let us dwell on a comparison of those models which describe well virtually all observational phenomena in the visible and in the near infrared.

Having analyzed photometric, polarimetric, and spectroscopic observations of the same objects, Grinin (1988), Grinin *et al.* (1988), Voshchinnikov and Grinin (1991), Grinin and Rostopchina (1996), and Rostopchina *et al.* (1997) did not note any long-term cyclic phenomena, but constructed a phenomenological model of a circumstellar envelope filled with protocometary bodies, which produced Algol-like fadings as they rotated around the star. These authors provided a well-grounded and computationally confirmed model of the physical processes during eclipses that accounted for the increase in polarization at minimum light, the virtual absence of spectroscopic variations, and the so-called bluing effect (the bluing of $(U–B)$, $(B–V)$, and, in some cases, $(V–R)$ at minimum light). We believe the explanation of all the observational phenomena associated with Algol-like fadings from a physical point of view offered by Grinin and his co-authors to be most plausible and do not revert to this issue below. Nevertheless, in their first publications, they did not discuss the long-term cyclic fadings detected by Shevchenko (1989). The GPC hypothesis was outlined in the above paper and, subsequently, in Shevchenko *et al.* (1993a, 1993b, 1993c).

Grinin *et al.* (1998) confirmed the existence of cyclic photometric variability in UX Ori stars and interpreted the long-period cyclicity as the large-scale transparency variations in circumstellar gas–dust disks attributable to external perturbations from the secondary component or large protoplanets.

* E-mail address for contacts: ezhik@astrin.uzsci.net

† Deceased.

Grinin *et al.* (1988) were the first to describe the phenomena. They presented a two-component dust model that consisted of opaque gas–dust clouds embedded in an optically thin envelope containing small dust grains. In this case, when the star is completely obscured by a dust cloud, the observer will record a weak blue emission reflected from the gas–dust disk and emerging from the scattering envelope. If the sizes of dust envelopes around young stars are 10–100 AU, then the emission scattered by circumstellar dust is a permanent factor, and its intensity does not depend on whether the star is hidden from the observer by a dust cloud or not. Therefore, the scattered emission performs yet another important function—it is a natural amplitude limiter of Algol-like minima.

When analyzing the degree of polarization and the variations in polarization angle, Grinin *et al.* (1988) concluded that grain orientation in the dust cloud shielding the star contributed to light polarization. The dust cloud producing an eclipse of the star is a nonsymmetric (cometary) structure with nonspherical aligned particles in its tail. The high degree of polarization at minimum light and the two-component structure of the Hα emission line suggest that the star's rotating gas–dust envelope is seen edge-on, and that its symmetry axis is close to the plane of the sky and parallel to the local interstellar field.

Our model, first described by Shevchenko (1989), includes three components:

(1) *A central body*, which is generally a compact structure similar in parameters to zero-age main-sequence (ZAMS) stars, or a body of an even smaller radius.

(2) An extended and flat *protoplanetary disk* of a fairly low temperature, which is initially a massive structure comparable in mass to the central star.

(3) *An extended envelope* with a lower surface temperature and low density is produced around the central body by accretion from the disk onto the star. Matter from the flat disk accretes onto the envelope, and the shock wave propagates within the envelop in such a way that a biconical ejection whose axis is perpendicular to the disk plane forms near the ptotostar's photosphere. In general, the envelope is optically thick in continuum and in lines, and only during strong accretion at the epoch of cocoon breakup does an optically thin (in continuum) envelope with strong emission lines form. These lines are blended with narrow absorption lines of the optically thick envelope (Shevchenko 1994, 1998).

A characteristic feature of our model is the presence in the disk of a large number of bodies similar in mass and radius to future Jupiter-like planets (Jupiter-like planets and brown dwarfs for massive stars) with elliptical orbits. When passing through periastron, the GPCs partially breaks up, temporarily form a dust envelope of low transparency around the star, and produce Algol-like eclipses.

If the largest GPC prevails in the disk of a particular star, then a periodicity or cyclicity with the period of GPC revolution around the central body must be observed in photometric fadings. We believe this to occur in the case of long-term cyclicity of BF Ori with a 6.3-year period.

PHOTOMETRIC OBSERVATIONS OF BF Ori

Grinin *et al.* (1998) collected photometric information and analyzed it when establishing the cyclicity of BF Ori. These authors used a set of 832 nights of photoelectric observations, with ~70 nights at the Maidanak Observatory. They did not analyze photographic observations. Although the photometric accuracy of photographic observations is low, they are of use, because the variability amplitude and scale are much larger than the accuracy of photographic photometry, while the cyclicity can be considered significant if the period exceeds the observing interval at least by more than a factor of 4. Photoelectric photometry does not satisfy this condition.

This paper was ready when the paper by Grinin *et al.* (1998) was published. Since our combined data set (photographic and photoelectric observations) was almost twice that analyzed by Grinin *et al.* (1998), we did not make any changes to our analysis and only performed an additional comparative analysis of the results from both papers, especially since the periods found in both studies were similar.

Below, we describe our combined set of photometric observations.

While studying stars in the Orion Nebula region, Parenago (1954) assigned BF Ori to the Orion population of young stars located at a distance of 400 pc. Having analyzed all the available magnitude estimates for BF Ori in 1864–1952, he obtained the following results: the photographic (m_{pg}) and visual (V) magnitudes of the star vary from 9.8 to 13.4 and from 9.7 to 12.6, respectively. Analyzing their photographic observations in 1957–1961, Rosino and Cian (1962) reported the range of magnitudes m_{pg} from 10.9 to 12.3. When describing the 1940–1960 light curve, Solov'ev and Erleskova (1963) pointed out that more rapid variations with a period of 15–20 days and an amplitude of the order of one magnitude were superimposed on slower variations with a period of ~1000 days and an amplitude of the order of 3^m in V. In addition, Nurmukhamedov (1973) made 166 magnitude estimates from plates of the Tashkent photolibrary for 1965–1969. We used these data to construct the combined light curve (Fig. 1a); the variability amplitude during this period was m_{pg} = 9.5–13.2. S.Yu. Shugarov's estimates for 1958–1978 made at our request from plates of the Moscow photolibrary (Shevchenko 1989), were also used to construct the combined light curve.

These estimates closely match the photoelectric results, suggesting that the pattern of variability has not changed since 1864 until now, i.e., in more than 100 years.

As far as we know, the first photoelectric observations of the BF Ori light curve were initiated at the Maidanak Observatory as part of a comprehensive program of research on Herbig Ae/Be stars and related objects, which was subsequently called the ROTOR program (Shevchenko 1983).

UBVR(*I*) observations of BF Ori as part of this program at Mount Maidanak have been continuing for 22 years. More than 700 photoelectric measurements in *B*, *V*, and *R* and a slightly smaller number of measurements in the remaining bands have been obtained over this period. The measurement accuracy is $\sigma(B, V, R) = \pm 0^m.01$. About 400 measurements were made by other authors. All the available photoelectric observations used for our analysis are collected in the table.

THE LIGHT CURVE OF BF ORI

The Herbig Ae star BF Ori is one of the most active early-type variables with a large variability amplitude. UX Ori, V517 Cyg, VV Ser, and WW Vul have a similar pattern of variability.

Figure 1a shows the combined light curve of BF Ori (m_{pg}, *B*). The observing period covers at least 17 cycles. The last nine and four cycles are well represented by photographic and photoelectric observations (Fig. 1b), respectively. The phase light curve with a period of 2300 days, or 6.3 years, is shown in Fig. 1c. The 6.3-year period is one of the most prominent features in the light curve of BF Ori. We used 300 photographic and 1080 photoelectric observations to construct and analyze the light curve.

The pattern of light variations can be divided into three levels:

(1) The star is at maximum light. The brightness in this state varies only slightly; the variability amplitude does not exceed $0^m.3$ in *V* and the colors are $(U–B) = (B–V) = (V–R) = 0^m.2$ (1979, 1989, 1994, 1997). The maximum *V* brightness during this period is $9^m.6$–$9^m.7$, while the minimum *V* brightness rarely falls below $10^m.3$. At this epoch, the brightness is generally near its maximum value ($9^m.6$ in *V*) for about two months (1979, 1989), and the degree of polarization at maximum light in *V* is *P* = 0.7–1.0% (Kardopolov and Ropaev 1987).

(2) The star is at minimum light (Fig. 2a). Sharp and deep Algol-like minima (1980, 1981, 1982, 1987, 1988, 1992, 1993) correspond to this epoch. The maximum rate of change in *V* brightness reaches 3^m in 20 days. Occasionally, quasi-cyclic variations with a period of about 50 days (the overall light curve for 1981 and 1988) appear during minimum light.

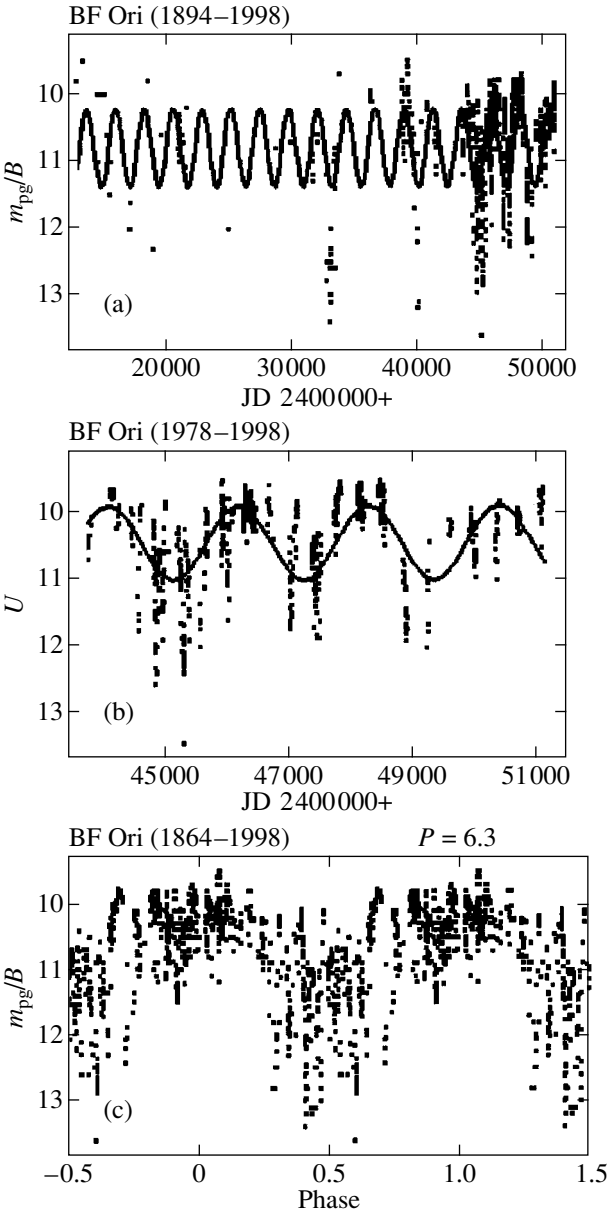

Fig. 1. Combined light curves of BF Ori (a) from photographic observations and *B*-band measurements and (b) from photoelectric *V*-band observations with a 5.75-year sinusoid superimposed and (c) the light curve from the entire data set folded with a 6.3-year period.

(3) The *V* brightness is intermediate between 10^m and 11^m, when quasi-cyclic variations with periods from 20 to 80 days (40 days, on the average) take place.

This cyclicity clearly shows up in some years. We used a periodogram analysis (Terebizh 1992) to determine the periods.

Figure 2a shows fragments of the light curve for BF Ori at the epochs when the variable is at minimum light (1981, 1982, 1987, 1988) or at intermediate brightness (1980, 1992). Each of the fragments in Fig. 2a generally includes one observing season (~7 months). Note that at similar phases of the 6.3-year period, the

Photoelectric observations

Year	N	V_{max}–V_{min}	$\langle U–B \rangle$	$\langle B–V \rangle$	$\langle V–R \rangle$	Author, reference
1978	13	10.08–10.72	0.39	0.35	0.34	ROTOR
1979	31	9.68–10.23	0.22	0.23	0.25	ROTOR; Rossiger (1983)
1980	22	9.91–11.79	0.35	0.34	0.36	ROTOR
1981	81	9.83–12.60	0.45	0.47	0.43	Rossiger (1983); Shaimieva and Shutemova (1985)
1982	64	10.25–13.47	0.42	0.44	0.33	ROTOR; Rossiger (1983); Herbst (1994)
1983	28	9.96–12.04	0.43	0.36	0.30	ROTOR; Herbst (1994)
1984	87	9.56–11.62	0.33	0.35	0.32	ROTOR; Herbst (1994)
1985	158	9.61–10.47	0.26	0.24	0.20	ROTOR; Herbst (1994)
1986	20	9.62–10.42	0.28	0.24	0.27	ROTOR; LTPV (1993)
1987	75	9.86–12.15	0.42	0.33	0.34	ROTOR; LTPV (1993); Herbst (1994)
1988	103	10.23–13.59	0.43	0.37	0.39	ROTOR; LTPV (1993)
1989	92	9.57–10.65	0.32	0.28	0.27	ROTOR; LTPV (1993)
1990	70	9.59–10.27	0.31	0.22	0.22	ROTOR; LTPV (1994)
1991	63	9.55–10.50	0.33	0.22	0.22	ROTOR; LTPV (1994)
1992	45	10.25–11.94	0.48	0.40	0.43	ROTOR; LTPV (1995)
1993	15	10.13–12.06	0.50	0.43	0.48	ROTOR; LTPV (1995)
1994	23	10.03–10.38	0.35	0.30	0.34	ROTOR; LTPV (1995)
1995	36	9.97–10.97	0.36	0.33	0.38	ROTOR
1996	20	9.87–11.02	0.34	0.29	0.32	ROTOR
1997	29	9.97–10.36	0.39	0.26	0.29	ROTOR
1998	18	9.66–10.55	0.32	0.23	0.25	ROTOR
1999	21	9.76–10.80	0.38	0.20	0.22	ROTOR

smaller scale cyclicity with a characteristic period of ~40 days (Fig. 2) is repeated with a similar variability amplitude.

Figure 2b shows similar (in duration) fragments of the light curve near maximum light (1985, 1986, 1991, 1992). Cyclicity with a similar or slightly shorter period is also seen here.

Figure 3 shows folded light curves for several seasons, which exhibit a quasi-period close to 40 days or its multiples. The 40–50-day cyclicity shows up more clearly near Algol-like minima and at intermediate brightness. The cyclicity is also noticeable near maxima (Fig. 2b), but with a lower significance of the period.

Figure 4 shows color variations in BF Ori during the entire observing season. ($U–B$), ($B–V$), and ($V–R$) colors are plotted against V magnitude in Fig. 4a. A reddening in the first half of the fading amplitude and a bluing in its second half are clearly seen in all diagrams. Two-color diagrams are shown in Fig. 4b. They reflect the complex processes of color variations, but correspond to the normal color of a star with an interstellar reddening in the upper part of the diagrams. The normal color reflects some additive temperature of the star and the envelope: spectroscopic studies (Shevchenko 1998) reveal a cool (T = 7000 K) envelope and at least a fragment of the photosphere of the central star (T = 10 000 K). The interstellar reddening is $A_V < 0.2$, just as for many stars in the Orion cluster (Shevchenko and Yakubov 1992).

Since the color variations are well described by the model of Grinin (1988), we restrict ourselves only to these comments. We also fully support the interpretation of the bluing and the increase in polarization at minima of UX Ori stars [Shevchenko (1989) proposed to call these objects BF Ori stars] justified by Grinin. This interpretation excellently accounts for all observational facts in this type of stars.

Below, we make an attempt to interpret the cyclic variations on the light curve.

LONG-TERM CYCLIC LIGHT VARIATIONS IN YOUNG STARS AND CHARACTERISTICS OF SOLAR-SYSTEM COMETS

Cyclic or periodic processes with periods from several hundreds of days to tens of years are observed mostly in extremely young stars of medium and relatively high luminosity with optically thick envelopes. According to our hypothesis, the cyclic processes with characteristic periods of several years are caused by the Keplerian rotation of GPCs, protoplanets, and giant protoasteroids—*giant planetesimals* (GPS) with eccentric orbits. Cyclic photometric fadings occur when these structures pass through periastron (or partially break up). The amplitude of the long-period processes

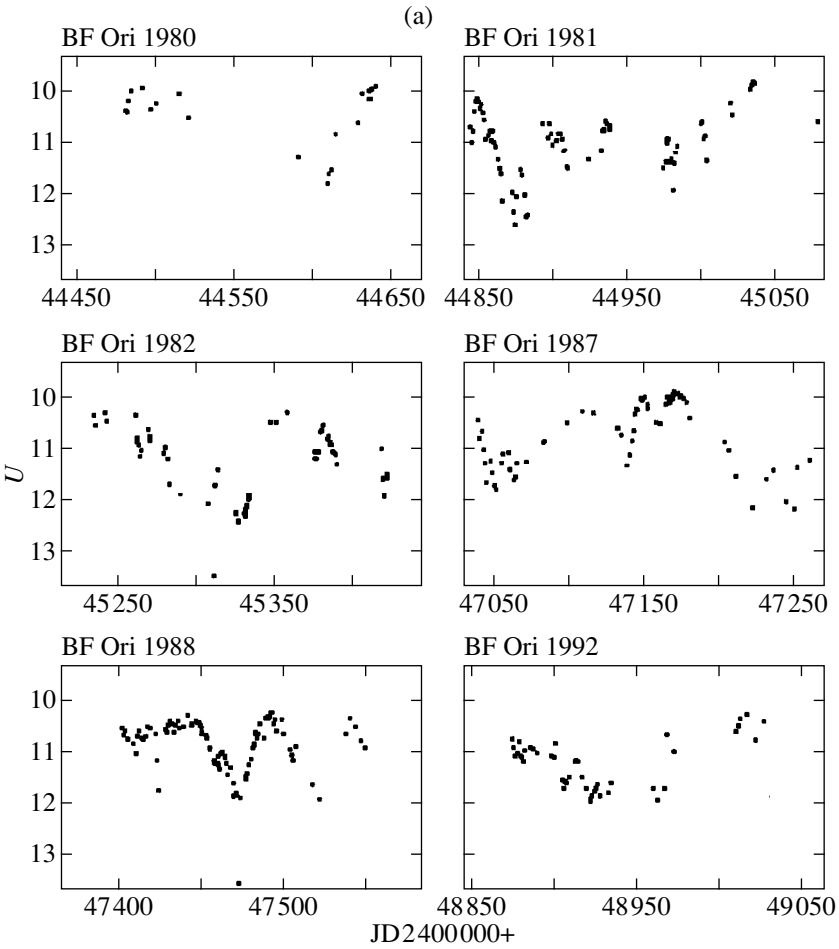

Fig. 2. Fragments of the light curve for BF Ori during different observing seasons: (a) photometric minima and (b) maxima of the star.

is most commonly large; it depends on the mass of matter in the GPC or GPS head and on the orbital inclination *i* to the line of sight.

Let us now consider some properties of comets in the Solar system as a projection of the once grandiose phenomena at the initial epoch of body formation in the Solar system to the present time, i.e., 4.5 Gyr later.

Currently available catalogs contain data on about 2000 periodic Solar-system comets detected since 2315 B.C. up until now. Some comets presently have enormous sizes, although their masses are negligible (cometary matter may be assumed to have partly accreted onto the Sun and partly dissipated into space in several million revolutions around the Sun). Thus, for example, the head of Comet 1811 I was larger than the Sun, while the tail of Comet 1882 II extended to 900 million km, and it passed at a mere 450 000 km from the solar surface with a velocity of 480 km s^{-1} at perihelion. At maximum, its brightness reached $-16\overset{m}{.}9$ (i.e., it was 4^m brighter than the full Moon). It was also noted that, when the passage of some comets through perihelion was repeated, their brightness and the tail size decreased. The revolution periods of some comets around the Sun decrease (Comets Encke, Halley, etc.). Comet Biela (1846 II) in 1845 split in two and gave rise to a meteor stream after 1852. Comet Shoemaker–Levy, which fell to Jupiter in 1996, split up into about 20 separate visible fragments before its fall, which were arranged in a "train" with approximately equal spaces between fragments and fell to the planet one after another. Actually, we witnessed the accretion of a small comet onto the planet with the accompanying energy release, surges of temperature excesses on the surface, and other characteristic phenomena. This process can be easily imagined as being thousands or millions of times more grandiose when Jupiter is replaced by a young star, while a small comet is replaced by a GPC.

Currently available data suggest that at the epoch when an extremely young, intermediate-mass star is surrounded by a cocoon, similar to those detected by the Hubble Space Teelscope in Orion (O'Dell and Wong 1996), the envelope (cocoon) actually corresponds (in order of magnitude) to the sizes of the dust

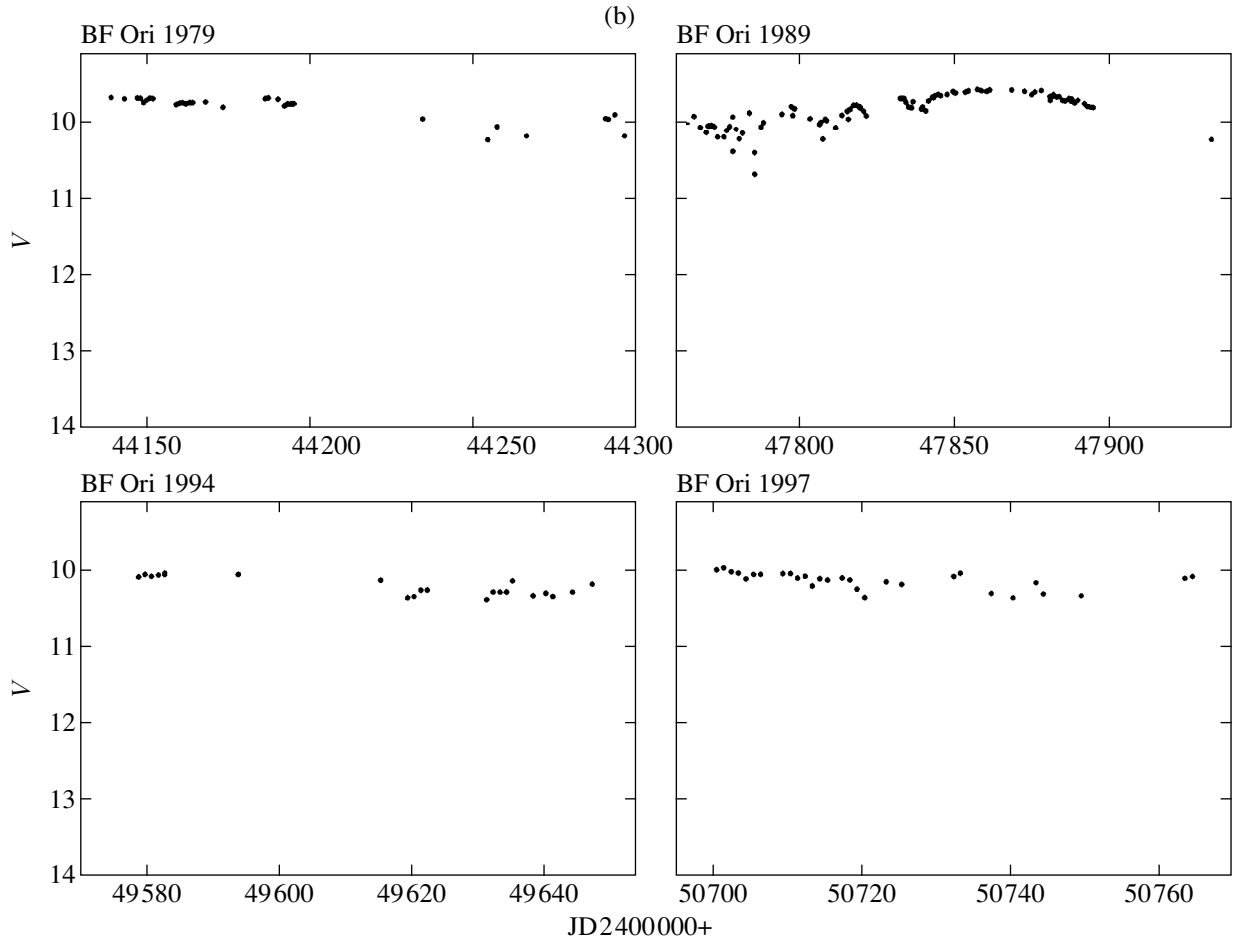

Fig. 2. (Contd.)

envelopes with protocometary bodies considered by Grinin (1988) and Voshchinnikov and Grinin (1991). However, at the epoch when the photosphere or envelope of such a star becomes observable, almost all of the circumstellar matter is concentrated in the protoplanetary disk, while the amount of matter in an elliptical envelope is much smaller. This, in particular, is evidenced by the fact that the circumstellar absorption near maximum light of extremely young stars in the RSF I Ori complex is low (Shevchenko 1989; Shevchenko and Yakubov 1992).

We would like to recall the results of our studies of the T Tau star GW Ori (Shevchenko *et al.* 1998), which may differ only slightly in mass from BF Ori, in connection with an interpretation of the BF Ori light curve. The most important results are as follows:

(1) The circumstellar absorption at maximum light is always low ($A_V < 0^m.5$) and does not differ in physical parameters from the interstellar one (total absorption $A_V = 1^m$).

(2) A single general smooth fading by $0^m.1$–$0^m.15$ in *V* was observed over five years, which was presumably caused by the arrival and accretion of a GPC with a revolution period $\gg$10 years and with an apoastron >10 AU. In this case, the Roche lobe of a 0.3 $M_\odot$ secondary star at a distance of 1 AU from the primary was also filled with dust during the entire period. This dust dispersed or accreted onto the secondary with a short delay (by one or two revolutions of the secondary around the primary star).

(3) Algol-like eclipses with an amplitude of about $0^m.3$–$0^m.4$ in *V* were observed at the epoch of the five-year-long fading by $0^m.1$ in *V*, which were unrelated to the secondary's revolution. They could be caused by the passage of fragments from a large GPC through the periastron of the central star if their Roche lobe is assumed to have also been filled with denser dust, as in the secondary of GW Ori.

(4) Since the orbital inclination of the dwarf is $i = 88°$ and since the dwarf's orbital plane most likely lies near the plane of the protoplanetary disk, which is optically invisible, we should assume the disk to be flat enough and the orbits of most large bodies in the disk to be coplanar.

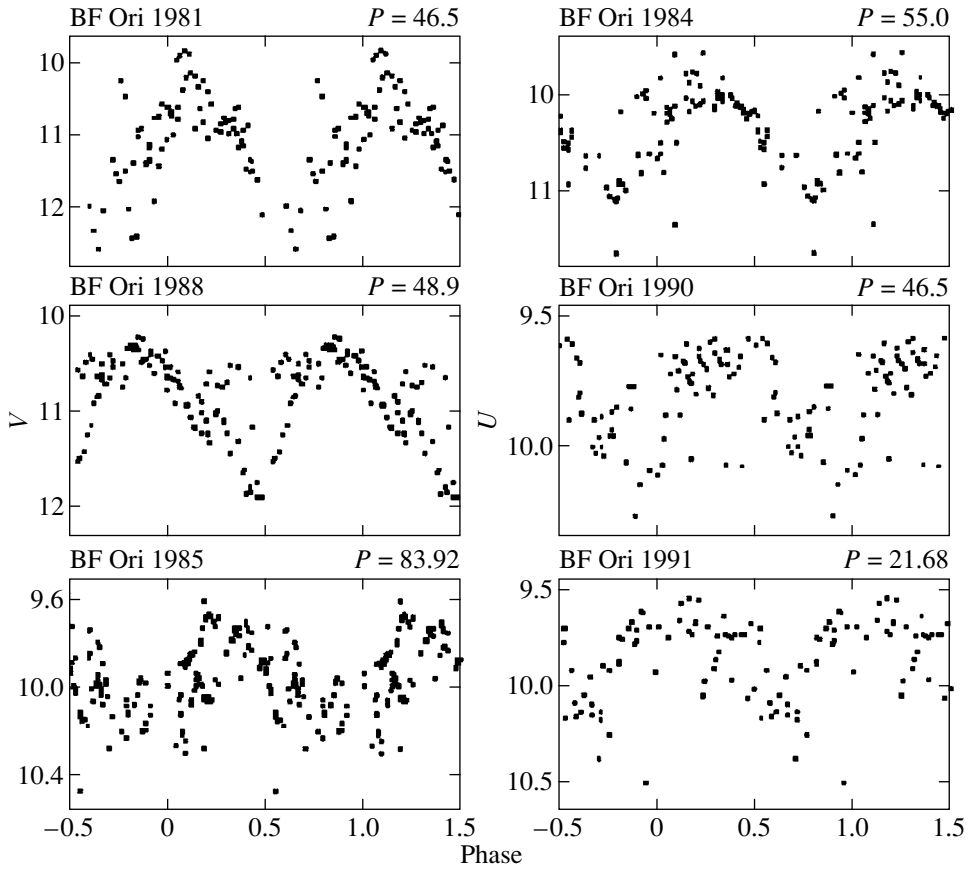

Fig. 3. Light curves for several seasons folded with periods revealed by a periodogram analysis.

Given the above discussion, we have every reason to believe that the 6.3-year periodicity of BF Ori was caused by the passage of a GPC, which we propose to call GPC I BF Ori, through periastron.

PROPERTIES OF GPC I BF Ori

The decline in brightness can be estimated from the light curves (Figs. 1a and 1b) to occur in a shorter interval than its rise to maximum (<0.5 and ~2 years, respectively). Algol-like eclipses also last for ~2 years, and the out-of-eclipse period is the same.

We may assume that, through tidal friction, GPC I BF Ori broke up into several fragments following each other and occupying 1/3 of its elliptical orbit. The deepest fadings apparently occur when GPC passes between the star and the observer. We hope that the periastron of the GPC I BF Ori orbit lies closer to the plane of the sky. During each passage near periastron, the GPC I BF Ori matter, which fills and overfills the Roche lobe of GPC I BF Ori, intensely disperses. A gas–dust medium emerges around the central star, which accretes onto its surface and scatters its light. The lifetime of such a temporary cool envelope is 2.5–3 years. At these epochs, the star's maximum V brightness decreases by almost 1^m compared to its brightness outside eclipse. A mandatory condition for the existence of such an envelope is its constant "replenishment" with GPC I BF Ori matter. If there is no such replenishment, the envelope will fall to the star or disperse. This can be easily calculated based on the free-fall time or on the grain evaporation time (Lang 1978).

While describing our model in the Introduction, we mentioned the presence of a compact permanent envelope with a temperature of ~7000 K, which is clearly seen when analyzing the BF Ori spectrum. At the epoch of Algol-like light variations, accretion onto this envelope is enhanced, and hot or cool spots (regions) can emerge on the compact envelope.

The Algol-like variations are cyclic with a period of 40–50 days, and their total depth exceeds 3^m in V at eclipse onset.

There are two explanations of the 40-day cyclicity at minimum light:

(1) The rotation of a spotted compact envelope with a 40-day period or its multiples. Because of spot migration and changes in the spot area and figure and because of the variations in the equatorial envelope radius due to a nonuniform accretion rate, this period undergoes small variations (Fig. 3).

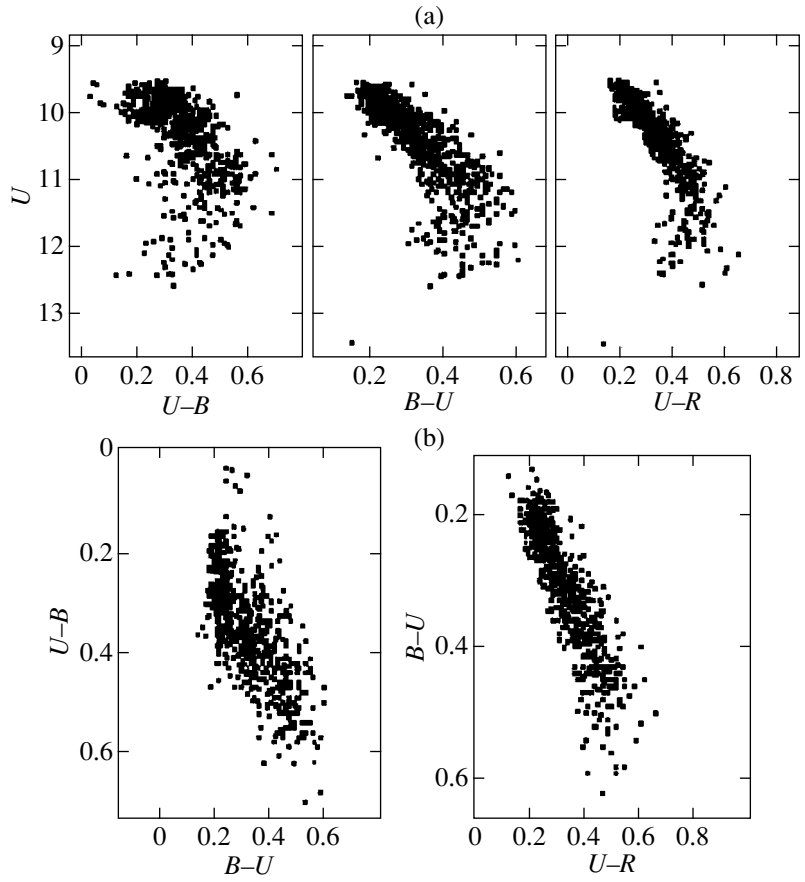

Fig. 4. Color variations in BF Ori from the combined photoelectric light curve: (a) colors versus *V* magnitude; (b) two-color diagrams.

(2) The fragments into which GPC I BF Ori broke up are spaced approximately equally (30 ± 15 million km). The number of fragments (of the order of ten) and their sizes can then be roughly estimated. The cyclicity is indistinct near maximum light.

Both these explanation may hold simultaneously and be interrelated.

The only known parameter of GPC I BF Ori is its revolution period of 6.3 years. More or less realistic assumptions about the masses of the central star and GPC I BF Ori, as well as about the orbital eccentricity, yield an estimate of the semimajor axis for GPC I BF Ori, ~10 ± 3 AU.

According to preliminary estimates, the revolution period of GPC I BF Ori decreases at a rate of 0.01 *P*/*P*, although it may well be that the period abruptly decreased in 1990. In the past nine years, a periodogram analysis has revealed a period of 2100 days, or 5.75 years. A similar period was also found by Grinin *et al.* (1998), because they used only recent observations.

The above parameters (for example, the period) of comet orbits in the Solar system can vary for various reasons, while GPCs, as well as comets in the Solar system, can break up into such small fragments that the period can subsequently become unobservable.

On the other hand, it should be remembered that, although GPC I BF Ori dominates in mass and size over other GPcs, their manifestations on the BF Ori light curve are quite real and may already be observable.

The historical light curve of UX Ori (Figs. 5a and 5b) is an example of cyclicity with several periods. Apart from a cyclicity of about 3.7 days (Shevchenko *et al.* 1993), for which the mean light curve is similar to that of BF Ori, there are a 30-year cyclicity and, possibly, several more. Shevchenko *et al.* (1993) gave cyclicity periods for seven more Herbig Ae/Be stars, one of which was not confirmed in subsequent observations.

Herbst and Shevchenko (1999) failed to establish a cyclicity for some young nonstable stars with distinct large-amplitude Algol-like fadings, for example, WW Vul. Two or more cyclic processes with similar amplitudes may be superimposed on each other. We believe that these periods should be searched for by using a different mathematical apparatus than that we used here (Terebizh 1992).

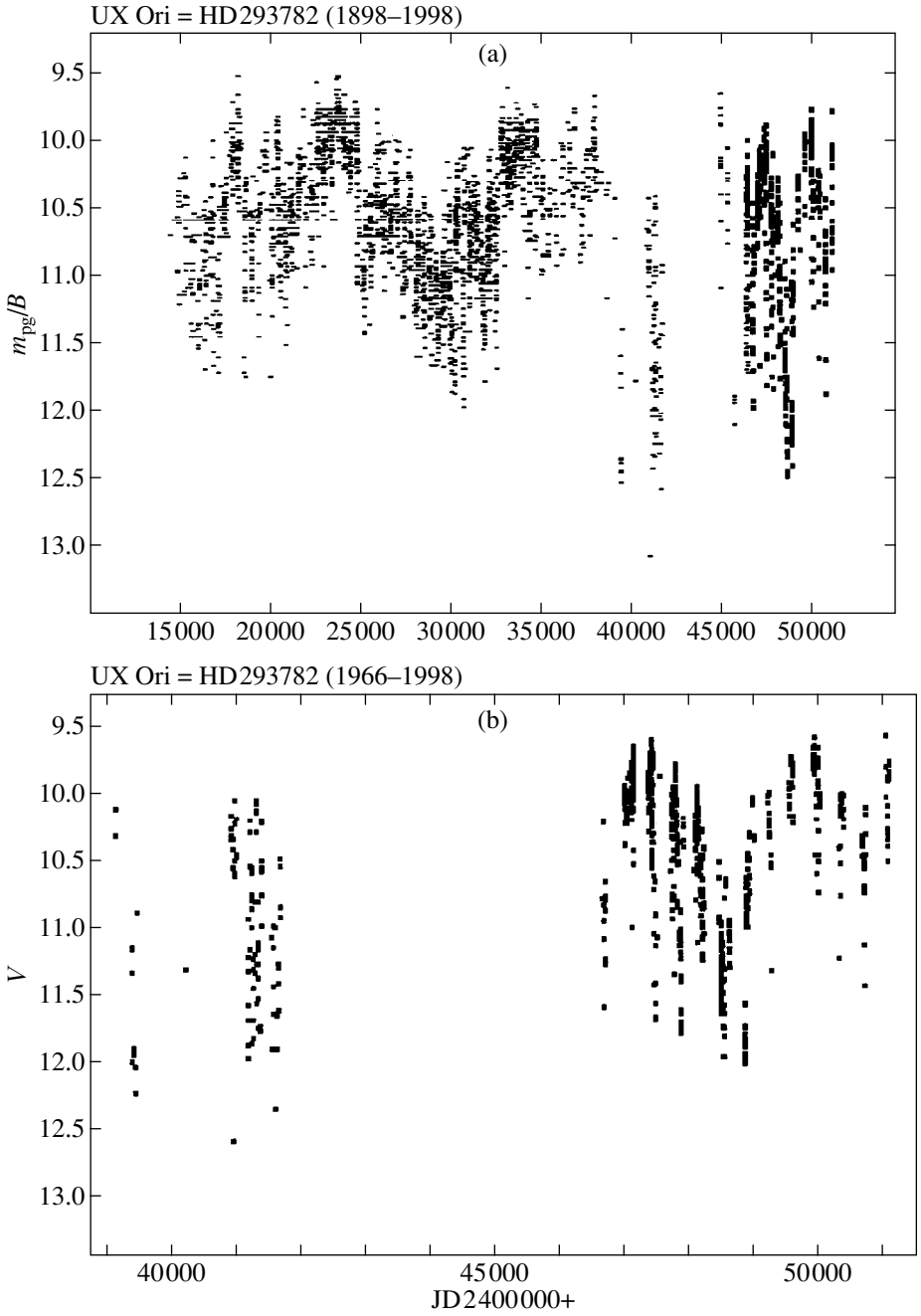

Fig. 5. Combined light curve of UX Ori (a) from photographic observations and *B*-band measurements and (b) from photoelectric *V*-band measurements. A cyclic variability with a different cycle duration is seen.

COMPARATIVE ANALYSIS OF NONSTATIONARITY MODELS FOR YOUNG STARS AND PROTOCOMET PROPERTIES

Although Grinin's model (below, we call it so for simplicity) is similar to ours, there are marked differences between them. It should therefore be considered in more detail. A detailed description of the model was given by Voshchinnikov and Grinin (1991) as applied to WW Vul. The visible emission originates from the star in a nonspherical envelope with a semimajor axis of about 140 AU and a semiminor axis of 50 AU. There is a cavity with a radius of ~7 AU at the envelope center in which the temperature of dust grains is higher than 1000 K, and they rapidly evaporate. The mass of the dust producing the scattered emission is approximately 10^{25} g. In the star's bright state, the contribution of the scattered emission is modest (~10%).

Dust clouds move in a tenuous envelope, occasionally shielding the starlight and producing Algol-like

minima. These clouds have a more or less compact central clump (core) with a radius of ~0.1 AU and a several times larger tenuous region. The clouds producing eclipses move in elongated orbits with semimajor axes $A > 10$ AU. A more recent phenomenological model of circumstellar envelopes was given by Grinin and Rostopchina (1996).

The main element of the updated model is a rotating gas envelope (disk). The disk is replenished with matter by the accretion of circumstellar material. Part of the accreting matter decelerates and is thrown back as it interacts with the star's rotating magnetosphere and under light pressure. The magnetic field of the dust disk coincides with its equatorial plane. As a result, an anisotropic wind is formed, which is peculiar in that the outflowing matter fills a conical layer. The Hα profiles change with the angle at which we observe the envelope.

Finally, this model has been updated most recently by Grinin *et al.* (1998), who took into account long-term cyclicities. In this model, emphasis is placed on the large-scale perturbations in hypothetical flat protoplanetary dust disks produced by the (tidal) effect of companions like brown dwarfs or giant proto-Jupiters. On the other hand, the new interpretation does not deny the existence of periodic GPCs or whole families of GPCs either, although Grinin *et al.* (1998) argue that a weakness of this idea is the lack of any clear explanations whatsoever for the so-called "two-component" structure of activity cycles found by them.

We gave much attention to a description of Grinin's model in order to emphasize its strength (the full interpretation of all colorimetric, polarimetric, spectroscopic, and infrared observations) and to justify the marked differences between it and our model.

(1) While critically analyzing this study, V.P. Grinin insist that, according to the calculations of Artymowicz and Lubow [see Grinin *et al.* (1998) for references], mass flows are formed in gas–dust disks of young stars, which result from the binary nature of these stars and which lead to a departure from axial symmetry. This departures can be responsible for periodicities. We do not reject this explanation. Nevertheless, the binary nature of BF Ori has not yet been established, while the pattern of variability on a time scale of 40–50 days with an amplitude up to 2^m in V (see Fig. 3) cannot be explained in terms of this model.

Previously, an elliptical cloud with randomly distributed protocometary bodies embedded in a gas–dust medium have been considered. The motion of such bodies does not account for the cyclicity in Algol-like fadings and for the repeatability of small-scale cyclicity. This would require a large number of protocomets with sizes increasing along the line of sight and irregularly distributed in the cloud. In addition, the protocomet tails, if their nature is the same as that of the tails of real comets in the Solar system, have virtually no effect on the eclipse duration, because most of their matter lies on the line of sight.

A flat protoplanetary disk is also preferred to such a cloud, because the circumstellar absorption near maximum light (for two years) is too low in several cases. *A dust cloud in which light is scattered and polarized appears to emerge when a GPC arrives to the periastron region and when it partially breaks up*. After the GPC and its fragments go away from the periastron region, accretion onto the central star ceases, and transparency is restored, as in the case of BF Ori, in a time comparable to the free-fall time.

In some cases, the breakup and eclipse of the central star are so intense that the eclipse amplitude exceeds the constraint imposed by other models (V1686 Cyg with an amplitude of $\sim 5^m$ in V and V1318 Cyg with an amplitude $>7^m$ in V may serve as examples). In this case, the bluing effect can be unobservable or have the nature of a partial eclipse (see also The 1994). This is probably related to the sizes and density of the newly formed dust envelope. Only for eclipsing-region sizes of ~1 AU is a bluing is observed, while only a reddening is observed for more compact sizes or at high density (mass).

(2) The Hα profile for Herbig Ae/Be stars and related objects (Grinin and Rostopchina 1996) may be associated with the orientation of an elliptical cloud or disk, as in classical stars with γ Cas-type envelopes.

First, the Hα profile for many stars undergoes large and, occasionally, rapid variations, changing in several hours from a split one to a single and/or multicomponent one (see, e.g., Shevchenko 1991), which cannot be associated with the orientation of an elliptical or flat disk.

Second, the most recent observational data (Shevchenko *et al.* 1998) suggest that *the star is not eclipsed by a flat disk* even at a disk inclination $i > 87$. An elliptical disk would cause a permanent circumstellar reddening. This is not observed for BF Ori.

THE FORMATION AND PROPERTIES OF PROTOPLANETARY DISKS

Let us revert to our analysis of the conditions in circumstellar envelopes and protoplanetary disks at the epoch of planet formation and intense accretion.

As was shown previously (Shevchenko 1989; Shevchenko 1994a), at the initial stage of protoplanetary-disk formation, when accretion onto the star proceeds from the decaying cocoon, it can actually be nonsteady, and changes in its activity can be caused by tidal phenomena. An analysis of the spectrum for the Herbig Ae star V380 Ori (Shevchenko 1994a, 1998), a neighbor of BF Ori, indicates that enhanced heavy-element differentiation in the circumstellar formation and light-element dissipation through a biconical funnel take place at this epoch. However, an envelope with strong emission lines prevails in the star at this epoch, while

the photometric variability in such stars is irregular and has a low amplitude; Algol-like light variations in stars with strong emission lines are rare, have low amplitudes, and are random in nature. The circumstellar absorption in such stars is generally substantial. In addition, the unidentified molecular bands, which apparently also originate in circumstellar space, are strong. This stage is short in the observed sample. Herbig Ae/Be stars with very strong emission lines account for less than 10% of their total number.

The number of stars with optically thick (in lines) envelopes is considerably larger. In particular, they include BF Ori and almost all stars with Algol-like minima (Shevchenko 1989; Shevchenko *et al.* 1994).

At this stage, the formation of a protoplanetary disk is essentially complete, and accretion onto the star proceeds mainly from the disk.

First, as was pointed out above, the circumstellar absorption at maximum light is negligible, and, accordingly, the amount of dust on the line of sight in an elliptical disk is modest.

Second, since no external perturbations can cause a significant enhancement of the dust density in an elliptical envelope, accretion may be considered to be replenished through a flat disk alone.

Below, however, we attempt to show that the dust component in the protoplanetary disk is modest in mass, limited in distance from the central star, and, consequently, variable accretion from a flat dust disk cannot satisfactorily explain the observed pattern of Algol-like periodic eclipses.

The accretion period and the lifetime of the dust grains falling to the star from the decaying cocoon are comparable to the time of grain free fall to the star; they finish in 100–1000 years. Grains with elliptical orbits whose periastron is less than several AU cannot exist for a long time because of their evaporation and mass loss; they will evaporate or be accreted onto the star in several tens or hundreds of revolutions.

There can be no large dust layer in the planet formation region either, because the protoplanets collect dust grains in a fairly broad belt around their orbits in a very short time (dust clouds near protoplanets can exist for a long time near Lagrangian points or inside their Roche lobes). Even if a dust (gas–dust) layer exists in the protoplanetary disk, it lies at a distance from the star where its radiation has no effect on the existence of grains, while the amount of matter is not enough for protoplanets to be formed, i.e., at a distance of tens of AU from the star. Accretion from such a hypothetical disk cannot produce observable large-scale Algol-like periodicities, especially if we take into account grain transformation on the long path from the hypothetical disk to the star.

Let us consider yet another type of protoplanetary-disk population, which can play a certain role at the epoch of planet formation. We have in mind meteoritic matter, which exceeded in mass the currently existing meteoritic substance in the Solar system by millions of times. In order for micrometeorites not to suffer the same fate as do dust grains, they must exceed them in mass by hundreds or thousands of times. Asteroids, which are similar in size to terrestrial planets, lie at the other end of the statistical mass distribution for meteorites. If the disk subsystem with meteoritic substance has a thickness from 1/20 to 1/50 and if we make the fantastic assumption that the total mass of the subsystem is equal to the solar mass, then the number of meteorites will not exceed 0.01 m^{-3} for the most favorable statistical mass distribution (when low-mass meteorites prevail). Initially, when many meteorites accrete onto the star and protoplanets, this substance can actively form an optically thick envelope around the star and can be involved in the formation of more tenuous envelopes. However, simple calculations show that this substance cannot form a large dust envelope around the star and cannot determine such phenomena as cyclic Algol-like eclipses.

Thus, using simple calculations, we can show that neither a hypothetical dust disk nor meteoritic substance bear direct relation to the observable cyclic Algol-like fadings.

It is easy to understand that at the initial formation stage, the number of protoplanets with elliptical orbits can be considerably larger than the number of protoplanets with circular (or nearly circular) orbits. An overwhelming majority of these protoplanets or GPCs is doomed to disruption and breakup if their periastrons are sufficiently close to the central star.

It is such GPCs that produce the entire complex of observable phenomena related to cyclic Algol-like fadings.

As for the two-component structure of activity cycles discussed by Grinin *et al.* (1998), it is attributable, to a large extent, to the short duration of the observational epoch compared to the cycle duration (ratios from 1 : 1 to 1 : 4) and to the effect of secondary GPCs on the light curve.

CONCLUSION

Previously, Grinin *et al.* (1988, 1989, 1996, 1998), Shevchenko (1989), and Shevchenko *et al.* (1993a, 1993b, 1993c) provided observational evidence and calculations in support of the existence of GPCs causing Algol-like phenomena in Herbig Ae/Be stars and bright T Tau stars. Having established long-term cyclicity in a number of these objects (Shevchenko 1989; Shevchenko *et al.* 1994; Herbst and Shevchenko 1998), we have also adduced arguments for our version of the GPC hypothesis.

An analysis of the light curve for the Herbig Ae star BF Ori has allowed us to illustrate the GPC hypothesis by using GPC I BF Ori with a period of 6.3 years and with a semimajor axis of 10 ± 3 AU as an example.

Further studies of such phenomena are of considerable interest. We would be grateful to all the astrono-

mers who could participate in our program of GPC research in spectroscopic, polarimetric, and infrared observations.

ACKNOWLEDGMENTS

We wish to thank the CRDF Foundation for support and the Program for Support of Scientific Schools (project no. 96-15-96656). We also wish to thank S.D. Yakubov, K.N. Grankin, S.Yu. Mel'nikov, M.A. Ibragimov, V.B. Kondrat'ev, and the other observers whose took part in the ROTOR program. We are especially grateful to V.P. Grinin, whose critical remarks enabled us to correct some inaccuracies.

REFERENCES

1. V. P. Grinin and A. N. Rostopchina, Astron. Zh. **73**, 194 (1996) [Astron. Rep. **40**, 171 (1996)].
2. V. P. Grinin, N. N. Kiselev, N. Kh. Minkulov, and G. P. Chernova, Pis'ma Astron. Zh. **14**, 514 (1988) [Sov. Astron. Lett. **14**, 219 (1988)].
3. V. P. Grinin, N. N. Kiselev, and N. Kh. Minkulov, Pis'ma Astron. Zh. **15**, 1028 (1989) [Sov. Astron. Lett. **15**, 448 (1989)].
4. V. P. Grinin, A. N. Rostopchina, and D. N. Shakhovskoĭ, Pis'ma Astron. Zh. **24**, 925 (1998) [Astron. Lett. **24**, 802 (1998)].
5. L. Hartmann and N. Calvet, Astron. J. **109**, 1846 (1995).
6. W. Herbst, Astron. J. **108**, 1906 (1994).
7. W. Herbst and V. S. Shevchenko, Astron. J. **118**, 1043 (1999).
8. L. A. Hillenbrand, S. E. Strom, F. J. Vrba, and J. Kenne, Astrophys. J. **397**, 613 (1992).
9. V. I. Kardopolov and F. K. Ropaev, Astron. Tsirk., No. 1499 (1987).
10. K. R. Lang, *Astrophysical Formulae: a Compendium for the Physicist and Astrophysicist* (Springer-Verlag, Berlin, 1974; Mir, Moscow, 1978).
11. M. G. Nurmukhamedov, *Young Stellar Complexes* (FAN, Tashkent, 1973).
12. C. R. O'Dell and Shui Kwan Wong, Astron. J. **111**, 846 (1996).
13. P. P. Parenago, Tr. Gos. Astron. Inst. Mosk. Gos. Univ. **25** (1954).
14. L. Rosino and A. Cian, Asiago Contr. **125**, 30 (1962).
15. S. Rossiger, Mitt. Var. Stars **10** (2), 23 (1983).
16. A. N. Rostopchina, V. P. Grinin, A. Okazaki, *et al.*, Astron. Astrophys. **327**, 145 (1997).
17. C. Sa, M. V. Penston, and T. V. Lago, Mon. Not. R. Astron. Soc. **22**, 213 (1986).
18. A. F. Shaĭmieva and N. A. Shutemova, Perem. Zvezdy **22**, 167 (1985).
19. V. S. Shevchenko, *Herbig Ae/Be Stars* (FAN, Tashkent, 1989).
20. V. S. Shevchenko, Pis'ma Astron. Zh. **17**, 372 (1991) [Sov. Astron. Lett. **17**, 146 (1991)].
21. V. S. Shevchenko, Tsirk. Astron. Inst. Akad. Nauk Uz. SSR, No. 108, 23 (1993).
22. V. S. Shevchenko, Astron. Zh. **71**, 572 (1994a) [Astron. Rep. **38**, 505 (1994a)].
23. V. S. Shevchenko, Astron. Soc. Pac. Conf. Ser. **62**, 359 (1994b).
24. V. S. Shevchenko, Astron. Zh. **75**, 838 (1998) [Astron. Rep. **43**, 246 (1999)].
25. V. S. Shevchenko and S. D. Yakubov, Astron. Zh. **69**, 705 (1992a) [Sov. Astron. **36**, 359 (1992a)].
26. V. S. Shevchenko and S. D. Yakubov, Astron. Zh. **69**, 986 (1992b) [Sov. Astron. **36**, 509 (1992b)].
27. V. S. Shevchenko, K. N. Grankin, M. A. Ibragimov, *et al.*, Astrophys. Space Sci. **202**, 121 (1993a).
28. V. S. Shevchenko, K. N. Grankin, M. A. Ibragimov, *et al.*, Astrophys. Space Sci. **202**, 137 (1993b).
29. V. S. Shevchenko, É. A. Vitrichenko, K. N. Grankin, *et al.*, Pis'ma Astron. Zh. **19**, 334 (1993c) [Astron. Lett. **19**, 125 (1993c)].
30. V. S. Shevchenko, K. N. Grankin, M. A. Ibragimov, *et al.*, Astron. Soc. Pac. Conf. Ser. **62**, 57 (1994).
31. V. S. Shevchenko, K. N. Grankin, S. Yu. Mel'nikov, and S. A. Lamzin, Pis'ma Astron. Zh. **24**, 614 (1998) [Astron. Lett. **24**, 528 (1998)].
32. A. V. Solov'ev and G. E. Erleskova, Byull. Tadzhik. Obs., No. 34 (1963).
33. V. Yu. Terebizh, *Analysis of Astrophysical Time Series* (Nauka, Moscow, 1992).
34. P. S. The, Astron. Soc. Pac. Conf. Ser. **62**, 11 (1994).
35. N. V. Voshchinnikov and V. P. Grinin, Astrofizika **34**, 181 (1991).
36. LTPV Photometric Catalogue, ESO Scientific Report, No. 12 (1993).
37. LTPV Photometric Catalogue, ESO Scientific Report, No. 14 (1994).
38. LTPV Photometric Catalogue, ESO Scientific Report, No. 16 (1995).

Translated by V. Astakhov

Astronomy Letters, Vol. 27, No. 1, 2001, pp. 51–57. Translated from Pis'ma v Astronomicheskiĭ Zhurnal, Vol. 27, No. 1, 2001, pp. 61–67.

Minimum on the Light Curve of the Classical Symbiotic Star AS 338 in 1999

E. A. Kolotilov[1], I. Mikolajewska[2], P. M. Marrese[3], U. Munari[3], S. Yu. Shugarov[1], and B. F. Yudin[1]*

[1] *Sternberg Astronomical Institute, Universitetskiĭ pr. 13, Moscow, 119899 Russia*
[2] *N. Copernicus Astronomical Center, Bartycka 18, Warsaw, 00-716 Poland*
[3] *Padua Astronomical Observatory, Asiago, I-36012 Italy*

Received April 25, 2000

Abstract—We present our *UBVRI* photometry and spectroscopy of AS 338 performed in 1999–2000. Another eclipse of the hot component in this symbiotic binary system, the deepest one ever observed, occurred in September 1999. The *U* brightness declined by ~2^m, the Hβ flux decreased by a factor of ~2.3, and the [O III] λ5007 flux did not change. The hot component is eclipsed at orbital phases φ ≈ 0.045–0.057. The *U–B* color index begins to appreciably fluctuate during an eclipse of the hot component and its circumstellar envelope. About 100 days after a strong outburst of 1995, the mean *UBV* brightness of AS 338 declined linearly in the ensuing five years at the same rate in all bands ($\Delta U/\Delta t \approx 10^{-3}$ mag/day). The brightness of the outer, uneclipsed parts of the circumstellar envelope also decreased, which is attributable to a reduction in the luminosity of the hot component against the rise in its temperature. The appearance of He II lines has not yet been recorded, though the optical brightness of AS 338 has already dropped by ~2^m after the outburst. © *2001 MAIK "Nauka/Interperiodica".*

Key words: *stars—variable and peculiar*

INTRODUCTION

AS 338 was cataloged as a symbiotic star by Allen (1984). Having obtained its spectrum in 1978, he found numerous emission lines (H I, He I, He II, [O III]), along with strong TiO molecular bands. In other words, the spectrum was clearly a combination one, and AS 338 had every reason to be included in the group of symbiotic stars (Boyarchuk 1976; Yudin 1992).

The first and second novalike outbursts of AS 338 were recorded in 1983 (Schulte-Ladbeck 1985) and 1995 (Elizalde *et al.* 1995), respectively. Regular photometric and spectroscopic observations of the star were initiated in 1983; their results were published by Esipov *et al.* (2000).

By the pattern of its outburst activity, AS 338 can be assigned to the group of classical symbiotic stars, i.e., Z And stars (Yudin 1992). The 1983–1998 observations show that, ~90% of the time, the hot component of AS 338 was in a state when its optical brightness was enhanced, while its temperature was too low, by the standards of symbiotic stars ($T_{\rm hot} < 5 \times 10^4$ K), to be capable of exciting He II lines. This state was called active. The state when the hot component excited these lines was called quiescent, considering that the star's visual brightness at this time was close to a minimum. The two states differ markedly in *B–V* (Esipov *et al.* 2000).

Munari (1992) noticed several minima on the combined *V* light curve of AS 338, which were repeated with a period $P \approx 434^{\rm d}$. He associated them with eclipses of the binary's hot component by the red giant, as was subsequently confirmed by *UBV* observations (Esipov *et al.* 2000).

Esipov *et al.* (2000) analyzed the quiescent state of AS 338 and its transition to a new phase of activity, which manifested itself in two successive strong outbursts in 1993 and 1995. Here, we present our photometric (*UBVRI*) and spectroscopic observations of AS 338 in 1999–2000, when another eclipse was observed in the system. Its analysis allowed us to estimate parameters of the individual components of this binary symbiotic system when the hot component was in an active state with greatly reduced brightness. The star's optical brightness decreased by ~2^m after the 1995 outburst. Thus, this study complements our view of the pattern of transformations in the symbiotic star AS 338. Note that the next two eclipses will take place during a season when AS 338 will not be observable at the Crimean Station of the Sternberg Astronomical Institute (SAI).

* E-mail address for contacts: yudin@sai.msu.ru

Table 1. *UBV* photoelectric observations of AS 338

JD 2450000+	*U*	*B*	*V*
1277	13.57	13.69	12.76
1319	13.58	13.77	12.88
1346	13.56	13.75	12.86
1368	13.69	13.88	12.91
1375	13.64	13.82	12.95
1399	14.02	14.02	13.12
1404	14.14	14.29	13.41
1422	15.57	16.02	14.97
1431	15.50	15.84	14.78
1432			14.64
1434	15.73	15.81	14.76
1438	15.33	15.80	14.64
1439			14.61
1440			14.55
1441			14.45
1442			14.48
1444			14.35
1445			14.28
1448	15.11	14.97	13.97
1449	14.59	14.86	14.13
1452	14.35	14.31	13.52
1453	14.19	14.30	13.39
1455	14.02	14.06	13.14
1456	13.91	14.04	13.11
1459	14.00	14.01	13.13
1467			13.02
1468	13.99	13.99	13.13
1475	13.56	13.88	13.04
1482			13.00
1487			13.04
1491		14.03	13.11
1493	13.66	13.94	13.02
1522	13.61	13.76	12.93
1633			12.89
1634	13.92	14.05	13.06
1641			12.92

Table 2. *RI* photoelectric observations of AS 338

JD 2450000 +	*R*	Δ*I*
1432	12.17	–1.18
1434	12.17	–1.19
1438	12.17	–1.20
1439	12.14	–1.21
1440	12.14	–1.23
1441	12.10	–1.17
1442	12.13	–1.23
1444	12.11	–1.24
1445	12.07	–1.24
1467	11.44	–1.63
1487	11.62	–1.54
1491	11.55	
1633	11.40	–1.25
1641	11.42	–1.20

Note: Δ*I* is the *I* magnitude difference between AS 338 and the comparison star.

OBSERVATIONS

Photometric *UBVRI* observations of AS 338 have been carried out with the 0.6-m telescope at the Crimean Station (SAI). The star lying ~20″ north of AS 338 was chosen as the standard. In this case, the standard is recorded simultaneously during CCD observations. We estimated the standard's magnitudes to be $U = 14\overset{m}{.}24$, $B = 13\overset{m}{.}97$, $V = 13\overset{m}{.}21$, and $R = 12\overset{m}{.}27$. The measurement errors in the magnitudes of AS 338 do not exceed $0\overset{m}{.}03$.

Our *UBVRI* photometry is presented in Tables 1 and 2. Since the standard has not yet been calibrated in the I band, Table 2 gives magnitude differences between AS 338 and the standard. Figure 1 shows the combined *U* light curve of the star and its *U–B* and *B–V* color curves. The data for 1983–1998 were taken from Esipov *et al.* (2000).

Figure 2 shows the *V* light curve of AS 338 and its *U–B* and *B–V* color curves folded with the period $P = 434\overset{d}{.}3$. The dates of minima are given by

$$\mathrm{Min}(V) = 2\,448\,822 + 434\overset{d}{.}3E.$$

We searched for periodicities using the code written by Yu.K. Kolpakov (SAI). The phase φ = 0 in Fig. 2 corresponds to minimum optical brightness. Mikolajewska and Munari (1992) give the following values for the initial epoch of minima and for the variability period: JD 2 44 8820, $P = 435\overset{d}{.}4$, and JD 2 448 820.4, $P = 434\overset{d}{.}1$, respectively.

Figure 3 shows fragments of the two spectra of AS 338 taken with the 1.25-m telescope at the Crimean Station (SAI) before the beginning of an eclipse (July 27, 1999, φ ≈ –0.09) and near its middle (Sept. 14, 1999, φ ≈ 0.02). Figure 4 presents Hα profiles in the high-resolution spectra obtained on November 25, 1993 (φ ≈ 0.14) and October 27, 1999 (φ ≈ 0.12) with the 1.8-m Padua Astronomical Observatory telescope in Asiago (Italy). The crossed-grating echelle spectrograph takes spectra in the range 4000–7000 Å with a resolution of ~0.3 Å. We also have the December 1998 (φ ≈ 0.37) and

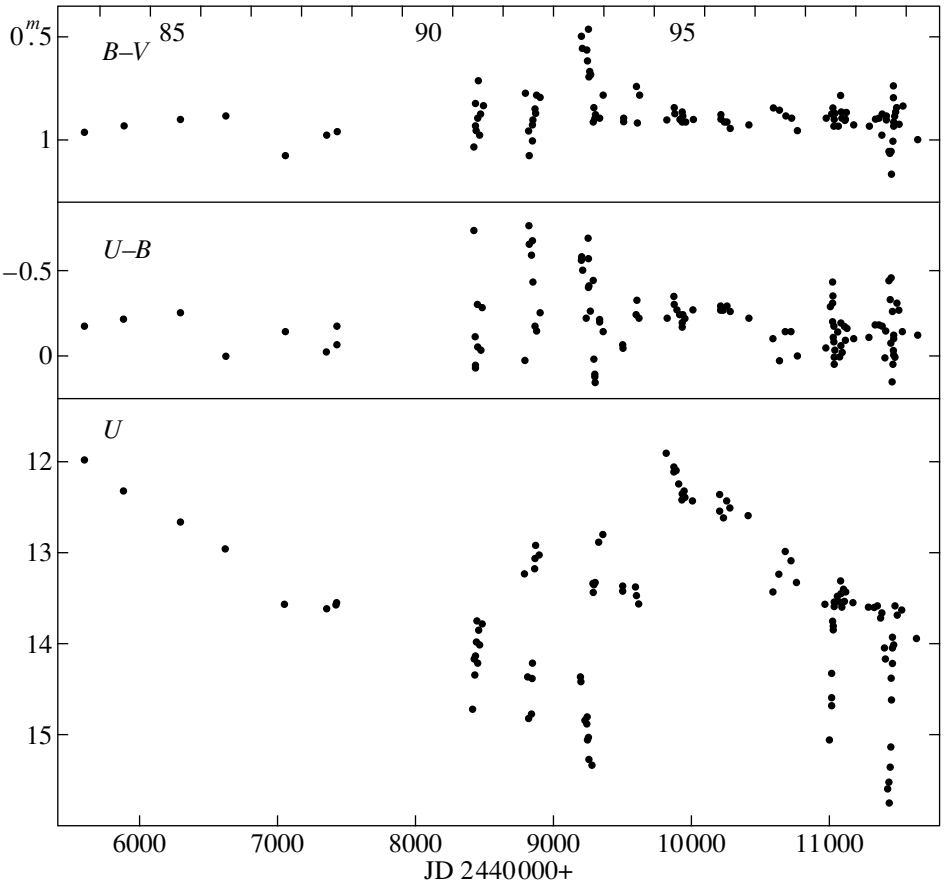

Fig. 1. The *U* light curve and the *B–V* and *U–B* color curves for AS 338. The data are from Table 1 and from Esipov *et al.* (2000).

November 1999 ($\varphi \approx 0.18$) spectra. Note that the continuum-normalized Hα profile is identical in all the 1998–1999 spectra.

DISCUSSION

The Hot Component

Photometrically, the 1995 strong outburst of AS 338 was completed in 2000 (Fig. 1). The *U* brightness decreased by $\sim 2^m$. The decline rate within the first 100 days after the outburst was a factor of ~3 higher than that in the ensuing ~5 years. In the second time interval, the mean *U* brightness decreased linearly with $\Delta U/\Delta t \approx 10^{-3}$ mag per day.

The star's brightness in *B* and *V* declined in the same fashion and approximately at the same rate. We can say that the *U–B* color index increased by $\leq 0.^m2$; i.e., the star slightly reddened in this spectral range, whereas the *B–V* color index did not change at all. Note that, in this case, we are dealing with times outside eclipses of the hot component and with trends in the mean level of these radiation parameters. At $E(B–V) = 0.5$ (Esipov *et al.* 2000), the color temperature of AS 338 at optical wavelengths was ~7500 K. Note that the contribution of spectral lines to the *B* and *V* radiation from AS 338 only reduces, though insignificantly, the *B–V* color index and, accordingly, increases the color temperature estimate. In other words, the continuum is redder than the star (continuum + spectral lines).

Typical classical symbiotic stars, such as, for example, Z And and CI Cyg, pass from the red-supergiant phase, at which they are found during outbursts, to the phase of a hot subdwarf capable of exciting He II lines in the circumstellar envelope as the *U* brightness decreases by $<1^m$. At the same time, there was no He II λ4 686 line in the 1999–2000 spectrum of AS 338 (Fig. 3), so, according to our classification, the star continued to be in its active state, characterized by a relatively low temperature of the hot component. In general, it resembles a Be star.

The reduction in AS 338 brightness after its outburst (Fig. 1) is accompanied by an increase in the hot component's temperature, as can be judged from the increase in contrast (equivalent widths) of the H I, He I, and [O III] emission lines. This conclusion is based on our yearly spectroscopic observations of AS 338. Portions of the two 1999 spectra are shown in Fig. 3. The rise in the hot component's temperature, if judged from the degree of envelope ionization, contrasts sharply

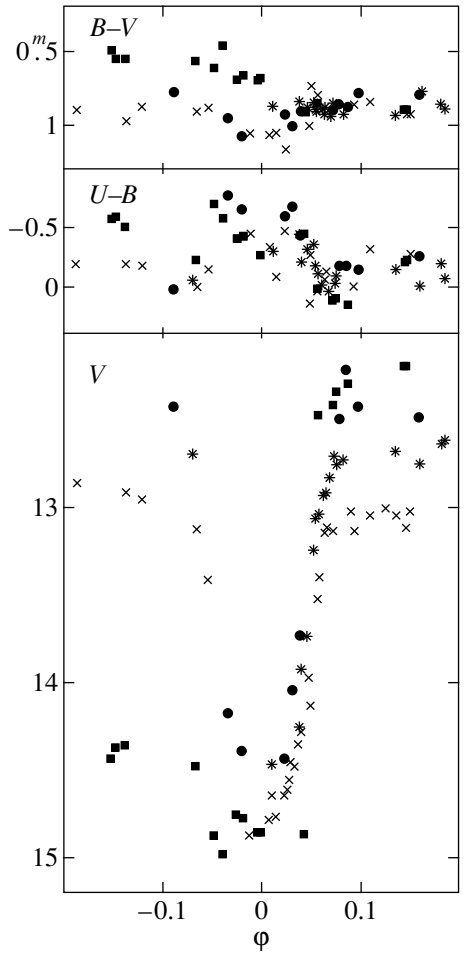

Fig. 2. The *V* light curve and the *B–V* and *U–B* color curves for AS 338 folded with the period $P = 434^{d}.3$. Circles, squares, asterisks, and crosses mark the 1992, 1993, 1998, and 1999 eclipses, respectively.

with the modest change in the shape of the star's optical spectral energy distribution spectrum.

Clearly, the color temperature at optical wavelengths is also considerably lower than the effective temperature. The hot component of AS 338 ionizes not only its own envelope but also the envelope around this binary system. We observe radiation from the latter during an eclipse of the hot component (Fig. 3). Thus, the hot component must have a very extended atmosphere, which is most likely not spherically symmetric. This is easy to understand if the hot-component outbursts in AS 338 have an accretion nature rather than a thermonuclear one (Yudin 1992). In that case, the hot component for the observer is actually the outer, fairly cool layers in an edge-on accretion disk.

If the temperature rose at constant bolometric luminosity of the hot component, as observed for symbiotic novae, then the brightness of the outer parts of the circumstellar envelope around AS 338 uneclipsed by the red giant at least would not decrease. However, as we see from Fig. 1, the brightness of AS 338 during the 1999 eclipse was lower than that during the 1998 eclipse. Consequently, the hot component's luminosity increases during an outburst and decreases after it. This fact is not obvious *a priori*, because the change in optical brightness of a symbiotic star can in principle be due to the energy redistribution in its spectrum alone. This is the case, for example, for symbiotic novae after their outbursts.

The Cool Component

Near the middle of the 1999 eclipse (phases $\varphi = 0 \pm 0.05$), AS 338 appeared redder in *B–V* by $\leq 0^{m}.2$ than it was outside eclipse. Simultaneously, the TiO λλ6215, 6717, 7125 molecular absorption bands became distinct in the red spectral region. Thus, the cool component begins to show up at visual wavelengths during an eclipse of the hot radiation source (hot component plus ionized envelope). However, its contribution to the symbiotic star's *V* light does not exceed 20% even during this period. Given the interstellar reddening, $(B–V)_0 \approx 0.65$ even during an eclipse, whereas for red giants, $(B–V)_0 \approx 1^{m}.5$.

During the 1999 minimum, the *R* magnitude of AS 338 was 12.16 (Table 1). Without the Hα and He I λλ6678, 7065 emission lines, whose equivalent widths are 480 and 9 Å, respectively, the magnitude is $R \approx 12.5$. If it is identified with the magnitude of the cool component, then its color index will be $(R–J)_0 \approx 2.8$, corresponding to a red giant's spectral type of M5. Munari (1992) also classified the cool component as M5 based on the 7000–11000 Å spectrum of AS 338 taken in August, 1990.

The Circumstellar Envelope

Outside eclipse (July 27, 1999, $\varphi \approx -0.09$), the Hβ and [O III] λ5007 fluxes were $\sim 9.2 \times 10^{-13}$ and $\sim 2.8 \times 10^{-13}$ erg cm^{-2} s^{-1}, respectively. During the eclipse (Sept. 14, 1999, $\varphi \approx 0.02$), the flux in the hydrogen line decreased by a factor of ~2.3, while that in the oxygen line did not change. At the same time, the *U* flux dropped by a factor of ~5.8. Thus, the forbidden [O III] line originates in the outer parts of the circumstellar envelope uneclipsed by the red giant. For $T_e = 1.5 \times 10^4$ K and a solar oxygen abundance in the envelope of AS 338, the $F(\text{H}\beta)/F([\text{OIII}])$ ratio corresponds to an electron density of $\sim 10^8$ cm^{-3}.

Figure 4 shows the Hα profile in November 1993, when AS 338 flared up and passed from quiescence to its active state (Esipov *et al.* 2000), and in December 1999. Both dates of observation correspond to approximately the same optical-brightness phase ($\varphi \approx 0.14$ and 0.12, respectively), while the star was brighter in *U* in 1993 by $\sim 0^{m}.7$ than it was in 1999. Note that, during

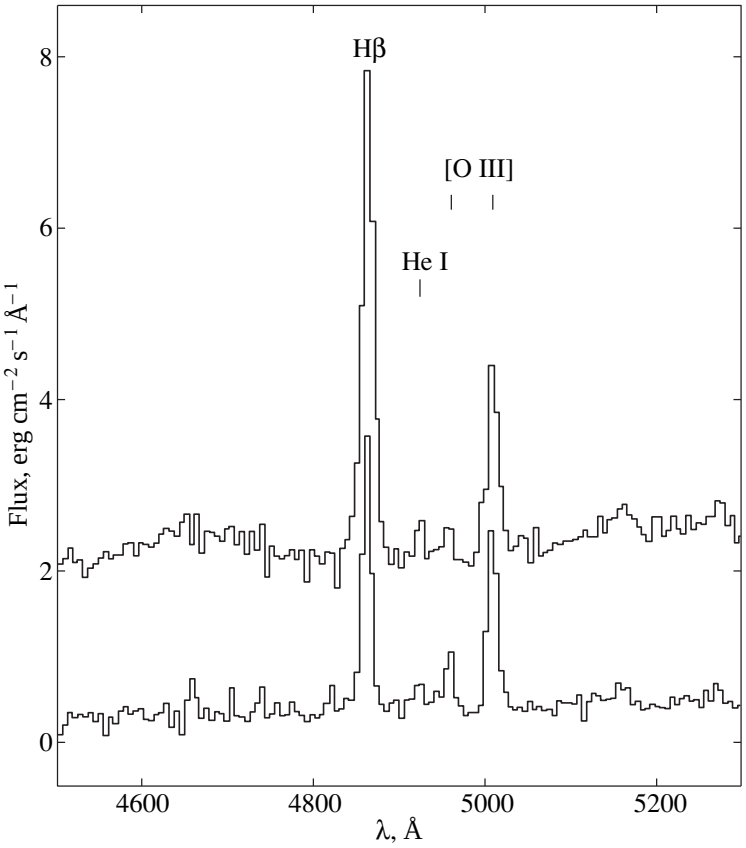

Fig. 3. Portions of the 1999 spectra for AS 338 outside and during eclipse of the hot component

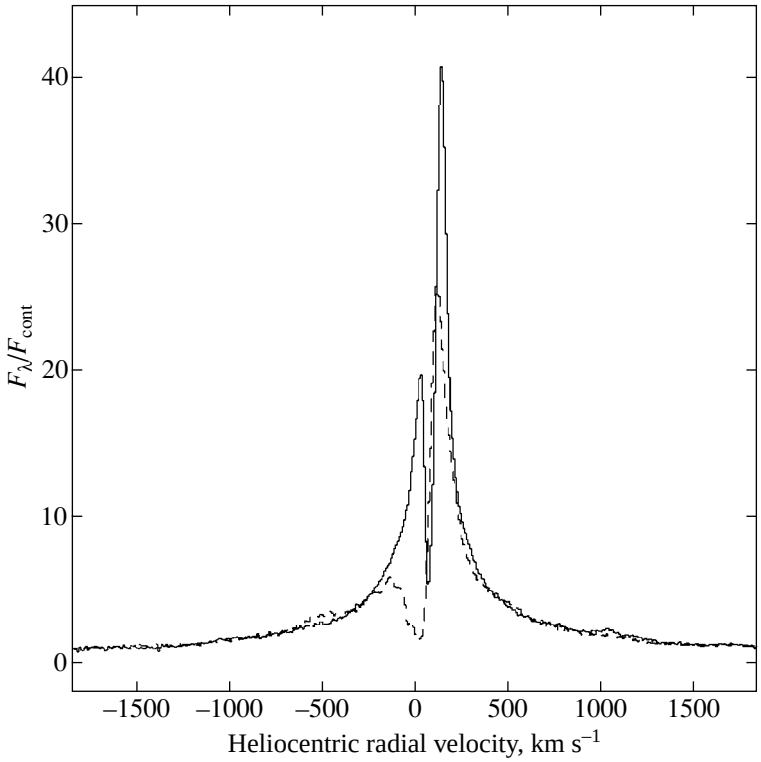

Fig. 4. Hα profiles during the outburst of the hot component of AS 338 (dashed line) on Nov. 25, 1993, and during its active state (solid line) on Oct. 27, 1999. Continuum-normalized intensity is along the vertical axis.

the star's outburst in 1995, it was brighter by $\sim 2^m$. In other words, the 1993 outburst is a medium one in amplitude.

The Hα line on both dates shows a distinct P Cyg profile. However, during outburst, the absorption component noticeably broadens through its blue wing, which extends to radial velocities of –120 km s^{-1}. This must be the case if the outburst of the hot component of AS 338 is accompanied by a sharp increase in mass-loss rate. And this undoubtedly must be the case if its outburst is thermonuclear in nature, as in the hot components of symbiotic novae or classical novae. However, temporal parameters of the AS 338 outbursts suggest that they most likely have an accretion nature (Esipov *et al.* 2000). In that case, accretion of the red giant's matter in the orbital plane must be accompanied by its ejection from the surface of the hot component in other directions.

The center of the fairly symmetric [O III] λ5007 emission line is at a radial velocity $V_r \approx 90$ km s^{-1}. Since this line originates in the outer, comparatively stationary parts of the circumstellar envelope around AS 338, this velocity can be identified with the radial velocity of the binary's center of mass. With respect to it, the absorption component of the Hα line extends to velocities of ~200 and ~60 km s^{-1} in 1993 and 1999, respectively.

A broad emission feature at $V_r \approx -500$ km s^{-1} is observed in the Hα blue wing during the outburst. A less intense emission feature is also present in the red wing at $V_r \approx 1000$ km s^{-1} (Fig. 4). They are absent in 1999. At the same time, the Hα profile in 1999 is the same as that in 1993 in its extended wings stretching to velocities of ±1500 km s^{-1}. Note that, as yet, no high-velocity features in the Hα profile and no very broad wings have been recorded in any other classical symbiotic star. They are observed in symbiotic novae when they pass through the Wolf–Rayet stage after their outbursts, as well as in the peculiar symbiotic star CH Cyg.

In Fig. 2, the data points for the 1993 eclipse, when an outburst of AS 338 occurred, are indicated by squares. The rightmost lower square ($\varphi \approx 0.043$) refers to the time when the star has already flared up, and those to the left from it refer to quiescence (Esipov *et al.* 2000). The brightness of AS 338 did not rise immediately after the outburst of the hot component, because it was still shielded by the red giant. It emerged from the eclipse 6 days later ($\varphi \approx 0.057$). Figure 2 shows that the steepest brightness rise during the eclipse egress in 1999 was also observed in this phase interval.

If we associate the amplitude of the *U* light variations in AS 338 at these orbital phases mainly with the hot component's eclipse egress, then we can estimate the flux ratio $F_{gas}(U)/F_{hot}(U)$, where $F_{gas}(U)$ and $F_{hot}(U)$ are the *U* fluxes from the ionized envelope and the hot component, respectively. This ratio was ~0.2, ~1.7, and ~2.0 in 1993, 1998, and 1999, respectively. Its rise, as well as the increase in emission-line contrast, suggest that the temperature of the hot component increased as the outburst decayed.

The *U–B* color index begins to noticeably fluctuate during the eclipse of the hot component and its circumstellar envelope (Figs. 1 and 2). Schematically, this process can be described as follows. At $\varphi \approx 0.09$–0.06, the *U–B* color index slightly increases (the star reddens). Subsequently, it decreases appreciably (by $\sim 0\overset{m}{.}3$) at $\varphi \approx 0.05$–0.02 (the star becomes bluer). Near the mid-eclipse ($\varphi \approx \pm 0.01$), the fluctuations are damped out. Clearly, the fluctuations appear due to a change in the relative contribution of the hot component and its circumstellar envelope during their eclipse to the total radiation from the star. We can say that the temporal blueing occurs at the time when the hot component is already shielded by the red giant, and only the light from its envelope is seen. The latter disappears behind the giant near the mid-eclipse, and the blueing vanishes. At this time, only the radiation from the circumstellar envelope surrounding both components of the symbiotic binary reaches us.

To summarize, we can say that the outbursts of AS 338, like those of typical classical symbiotic stars, are accompanied by an increase in the luminosity of the hot component and by a decrease in its temperature. To all appearances, the outbursts have an accretion nature. In particular, the temporal parameters of the AS 338 outbursts can be reproduced in the model of unsteady disk accretion, which cannot be said about the competing thermonuclear outburst model applicable to the outbursts of symbiotic novae. In addition, we see that the hot components of symbiotic novae during their outbursts can be considered as spherically symmetric radiation sources, whose color temperature at optical wavelengths does not contrast sharply with the effective temperature. At the same time, the accretion model is yet to reproduce the P Cyg profile, which appreciably broadens during outbursts.

AS 338 has the shortest orbital period among the classical symbiotic stars. At the same time, its cool component belongs to late-type red giants. There are no classical symbiotic stars with cool components later than M5. For the parameters of an M5 III red giant from Tsuji (1978), it will fill its Roche lobe in the binary system AS 338, which must cause accretion to activate. Its activity can account for the rareness of quiescent-state events in the hot component.

ACKNOWLEDGMENTS

We wish to thank M.S. Frolov for helpful advice on the photometric observations and to the referee for critical remarks. This study was supported by the Polish Research Committee (KBN grant no. 2P03D02112).

REFERENCES

1. D. A. Allen, Proc. Astron. Soc. Aust. **5**, 369 (1984).
2. A. A. Boyarchuk, in *Eruptive Stars* (Nauka, Moscow, 1976), p. 113.
3. F. Elizalde, F. Jablonski, D. Cieslinski, and R. Baptista, IAU Circ., No. 6165, 1995.
4. V. F. Esipov, E. A. Kolotilov, J. Mikolajewska, *et al.*, Pis'ma Astron. Zh. **26**, 200 (2000) [Astron. Lett. **26**, 162 (2000)].
5. U. Munari, Astron. Astrophys. **257**, 163 (1992).
6. R. Schulte-Ladbeck, Messenger **39**, 3 (1985).
7. T. Tsuji, Astron. Astrophys. **62**, 29 (1978).
8. B. F. Yudin, Zemlya Vselennaya **4**, 10 (1992).

Translated by N. Samus'

Astronomy Letters, Vol. 27, No. 1, 2001, pp. 58–64. Translated from Pis'ma v Astronomicheskiĭ Zhurnal, Vol. 27, No. 1, 2001, pp. 68–75.

Trigonometric Parallaxes and a Kinematically Adjusted Distance Scale for OB Associations

A. K. Dambis*, A. M. Mel'nik, and A. S. Rastorguev

Sternberg Astronomical Institute, Universitetskiĭ pr. 13, Moscow, 119899 Russia

Received March 6, 2000

Abstract—By directly comparing the photometric distances of Blaha and Humphreys (1989) (BH) to OB associations and field stars with the corresponding Hipparcos trigonometric parallaxes, we show that the BH distance scale is overestimated, on average, by 10–20%. This result is independently corroborated by applying the rigorous statistical-parallax method and its simplified analog (finding a kinematically adjusted rotation-curve solution from radial velocities and proper motions) to a sample of OB associations. These two methods lead us to conclude that the BH distance scale for OB associations should be shrunk, on average, by 11 ± 6 and $24 \pm 10\%$, respectively. Kinematical parameters have been determined for the system of OB associations: $u_0 = 8.2 \pm 1.3$ km s^{-1}, $v_0 = 11.9 \pm 1.1$ km s^{-1}, $w_0 = 9.5 \pm 0.9$ km s^{-1}, $\sigma_u = 8.2 \pm 1.1$ km s^{-1}, $\sigma_v = 5.8 \pm 0.8$ km s^{-1}, $\sigma_w = 5.0 \pm 0.8$ km s^{-1}, $\Omega_0 = 29.1 \pm 1.0$ km s^{-1} kpc^{-1}, $\Omega_0' = -4.57 \pm 0.20$ km s^{-1} kpc^{-2}, and $\Omega_0'' = 1.32 \pm 0.14$ km s^{-1} kpc^{-3}. The distance scale for OB associations reduced by 20% matches the short Cepheid distance scale (Berdnikov and Efremov 1985; Sitnik and Mel'nik 1996). Our results are a further argument for the short distance scale in the Universe.

Key words: *star clusters and associations, stellar dynamics*

INTRODUCTION

Even the nearest OB-stars are very distant objects; therefore, the distances to these stars are determined mainly by comparing their apparent magnitudes corrected for interstellar extinction with the absolute magnitudes that can be estimated from the known spectral types and luminosity classes or equivalent widths of hydrogen absorption lines. The distance scale of OB-associations is calibrated using blue supergiants in open clusters. The distances of the latter are referred to that of one of the nearest clusters (usually Hyades or Pleiades). Constructing the distance scale of blue supergiants is therefore a multistage procedure where each stage can introduce additional biases that are difficult to control. The Hipparcos catalog (ESA 1997) provided the first source of high precision trigonometric parallaxes and proper motions that can be used to directly refine the distance-scale zero points and perform detailed analyses of space velocities of high-luminosity stars, respectively. The Hipparcos catalog data have been used by many authors to calibrate the distance scale and infer the kinematical parameters of the system of classical Cepheids (Feast and Catchpole 1997; Feast and Whitelock 1997; Rastorguev *et al.* 1999) and to analyze the distance scale and large-scale kinematics of OB-stars and associations (Miyamoto and Zhu 1998; Kaltcheva and Knude 1998; de Zeeuw *et al.* 1999; Sitnik and Mel'nik 1999; van Leeuwen 1999; Reid 1999). However, the studies of the distance scale of OB-stars were either limited to III–V luminosity classes and small solar neighborhoods (within 1 kpc) (Miyamoto and Zhu 1998; de Zeeuw *et al.* 1999) or focused on the deviations from circular rotation due to the spiral density wave (Sitnik and Mel'nik 1999; Mel'nik *et al.* 1998), without determining the parameters of this circular rotation itself which were adopted from other works based on other objects (e.g., classical Cepheids). In this paper, we use for the first time the Hipparcos data to infer a zero point correction to the photometric distance scale of OB-associations and OB-stars of all luminosity classes.

Trigonometric parallaxes of OB-stars define the absolute distance scale of these objects that depends neither on empirical calibrations nor on theoretical models. Unfortunately, for the overwhelming majority of OB-stars, the accuracy of their individual distances based on Hipparcos trigonometric parallaxes is much lower than that of the corresponding photometric distances. Trigonometric parallaxes can nevertheless be used to statistically calibrate the zero point of the photometric distance scale. To do this, we found a relation between the OB-association photometric distances r_{BH} adopted from the catalog of luminous stars by Blaha

* E-mail address for contacts: mirage@.sai.msu.ru

and Humphreys (1989) and the distances inferred from trigonometric parallaxes.

Given radial velocities, proper motions, and photometric distances r_{BH} to associations, and interpreting these data in terms of a model of purely circular rotation of the Galactic disk, we can use statistical parallax technique to simultaneously determine a correction factor to the adopted distance scale as well as the full set of kinematical parameters for the sample under study. These parameter values and the correction to the scale allow the distribution of radial velocities to be best reconciled with that of proper motions (and with the hypothesis about the ellipsoidal distribution of residual velocities). On the other hand, adopting a number of simplifying assumptions about the distribution of residual velocities (in particular, assuming that it is isotropic), allows one to estimate a correction to the adopted initial distance scale by solving jointly the Bottlinger equations for radial velocities and proper-motion components in Galactic longitude. We thus determine the kinematically adjusted distance scale. This method is a simplified version of the statistical-parallax technique. Compared to the more rigorous classical version of the technique, the simplified method is less sensitive to eventual misestimates of the standard errors of the adopted proper motions and radial velocities, which can bias the inferred kinematical parameters.

The agreement between the trigonometric and kinematic distance scales can serve as an independent criterion for assessing the quality of observational data and our concepts of the motion of young stars in the Galactic disk.

REFINEMENT OF THE DISTANCE SCALE OF OB-ASSOCIATIONS USING TRIGONOMETRIC PARALLAXES

We used Hipparcos catalog data to compute the trigonometric parallaxes, p_t, of OB-associations from the Blaha and Humphreys (1989) list as median values of the parallaxes of individual member stars. The initial data are in the form of trigonometric parallaxes and we therefore converted the photometric distances r_{BH} of OB-associations into photometric parallaxes, $p_{BH} = 0.001/r_{BH}$ (r_{BH} in kpc). Table 1 lists 29 associations, each containing at least 10 stars with known parallaxes. The columns of table give the name of the association, its Galactic coordinates l and b; photometric distance, r_{BH}; photometric parallax, p_{BH}; trigonometric parallax, p_t and its standard error, ε_p; distance r_t corresponding to parallax p_t, and the number of stars n with known parallax.

Figure 1a shows the relation between trigonometric (p_t) and photometric (p_{BH}) parallaxes of OB-associations. Nearby associations ($p_{BH} > 0.001$ arcsec) outline a well-defined linear relation between the two quantities, $p_t = k'p_{BH}$. Least-squares solution of the set of linear equations $p_t = k'p_{BH}$ for 29 associations yields $k' = 1.14 \pm 0.05$. The standard deviation of the association parallaxes from the above relationship is 0.0004 arcsec. Parameter k' remains unchanged if we introduce weight coefficients $p \sim n$. The exclusion of the Sco OB2 association, which is nearest to the Sun, has no effect on the formal k' value, but only increases its standard error to 0.1.

In order to increase the sample size, we turned to the second part of the luminous-star catalog of Blaha and Humphreys (1989), i.e., that of field stars. The distances to these stars were determined using the same photometric calibration as was used to measure distances r_{BH} to OB-associations. The Hipparcos catalog (ESA 1997) gives trigonometric parallaxes p_t with standard errors of less than 0.001 arcsec for 855 field stars. Note that 496 of them are located within 1 kpc of the Sun. Figure 1b shows the relationship between trigonometric (p_t) and photometric (p_{BH}) parallaxes of these nearby field stars. Least squares solution yields a proportionality factor of $k' = 1.19 \pm 0.02$ between the two parallaxes, implying that trigonometric parallaxes are on the average 19% greater than the observed photometric parallaxes ($p_t = 1.19p_{BH}$).

It thus follows that the distance-scale factor k relating photometric (r_{BH}) and parallax-based (r_t) distances is $k = 0.88 \pm 0.05$ and $k = 0.84 \pm 0.02$ for OB-associations and OB field stars, respectively. The parallaxes of OB-stars thus require a 10–20% reduction of the Blaha and Humphreys (1989) distance scale.

REFINING THE DISTANCE SCALE TO OB-ASSOCIATIONS VIA STATISTICAL PARALLAXES

Method

In this paper, we use the most rigorous version of the statistical-parallax technique whose detailed description in the general form can be found in Murrey's (1986) book and in the paper by Hawley *et al.* (1986). This method consists in the simultaneous determination of the set of kinematical parameters (the vector of the full space velocity and the components of the velocity dispersion tensor) and the correction factor to the initial distance scale in order to maximize the likelihood of the actually observed data combination (coordinates, relative distances, radial velocities, and proper motions). The concrete formulas for our case can be found in Rastorguev *et al.* (1999), where statistical parallax technique has for the first time been used to refine the distance scales of Classical Cepheids and young open clusters. However, the analysis made in the above paper ignored random errors in the distance estimates for individual objects. The corresponding errors are not small in the case of OB-stars; therefore, we supplement formula (8) for covariance tensor L_{obs} of the observed quantities given in Rastorguev *et al.* (1999) by an additional term to allow for the errors in the observed distances (Murrey 1986).

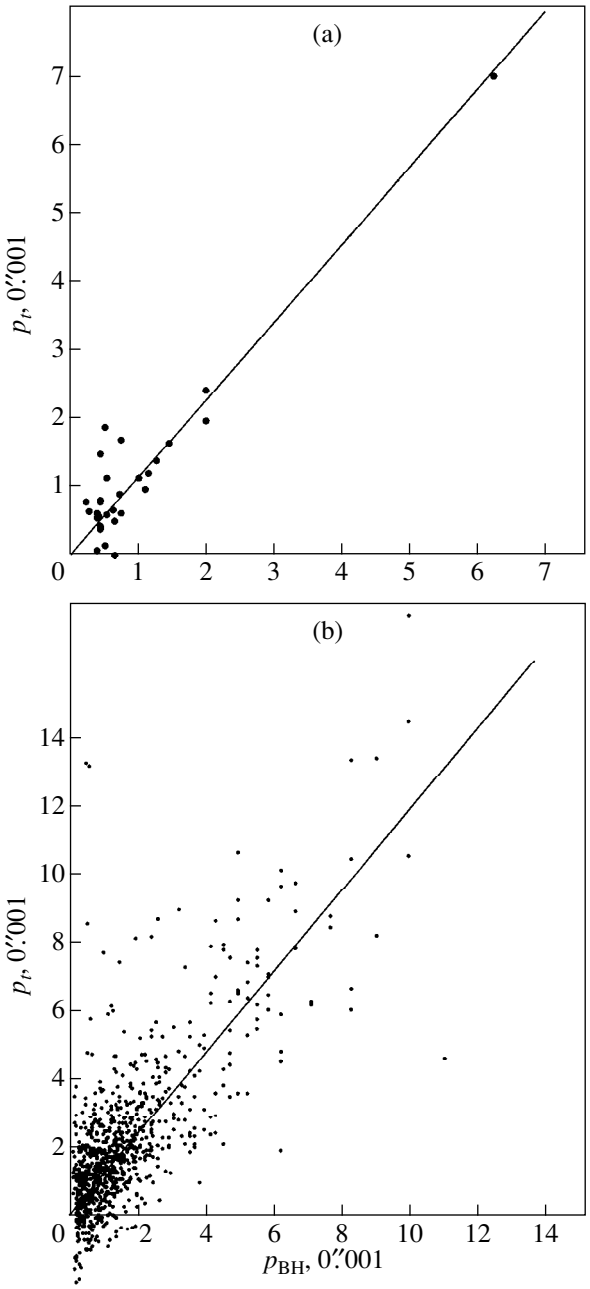

Fig. 1. Trigonometric p_t parallaxes of OB-associations (a) and field stars (b) plotted as a function of photometric p_{BH} parallaxes.

Initial Data

As the initial distances to associations we used the mean individual stellar photometric distances given in the BH catalog averaged over member stars. We adopted the radial velocities and the proper-motion components for association stars from the WEB (Duflot *et al.* 1995) and Hipparcos (ESA 1997) catalogs, respectively. We determined the median radial velocities, V_r, and median proper-motion components, μ_l and μ_b, along the Galactic longitude and latitude, respectively, for 59 OB-associations, each containing at least two stars with known radial velocities and at least two stars with known proper motions. We determined the standard errors of the association distance moduli, $\sigma_{DM_{ass}}$ from the following formula:

$$(\sigma_{DM_{ass}})^2 = (\sigma_{DM_0})^2/N_s, \quad (1)$$

where σ_{DM_0} is the standard error of the distance modulus of an individual OB-star (in this paper we assumed that it is equal to $0\overset{m}{.}5$) and N_s, the number of association members used to determine the mean distance. The "cosmic" dispersion of the distance-scale parameter was computed in accordance with formula (8) of Hawley *et al.* (1986).

Table 2 gives the following parameters for the associations with known kinematical characteristics: Galactic coordinates l and b; heliocentric distance, r_{BH}; median radial velocity V_r and its error ε_{V_r}; the number of association stars with known radial velocity n_r; median proper-motion components in Galactic longitude (μ_l) and latitude (μ_b) and their random errors $\varepsilon_{\mu l}$ and $\varepsilon_{\mu b}$, respectively, and the number of association stars with known proper motion, n_{lb}. Errors ε_{vr}, $\varepsilon_{\mu l}$, and $\varepsilon_{\mu b}$ correspond to the $P = 68\%$ confidence interla.

Results

We applied the statistical-parallax technique to a sample of 59 OB-associations. As provisional distances (to be refined) we used the distances from the BH catalog. Our free parameters in the likelihood-function minimization are the mean heliocentric velocity components of the association sample, u_0, v_0, and w_0 (in the directions of the Galactic center, Galactic rotation, and North Galactic Pole, respectively); the components of association velocity dispersion tensor, σ_u, σ_v, and σ_w; angular velocity of Galactic rotation at the solar Galactocentric distance, Ω_0 and its first two derivatives with respect to Galactocentric distance, Ω_0' and Ω_0'', taken at the solar Galactocentric distance, R_0; distance-scale factor k converting the provisional distances into the true distances ($r = kr_{BH}$). We adopted a solar Galactocentric distance of $R_0 = 7.1$ kpc (Dambis *et al.* 1995; Rastorguev *et al.* 1994; Glushkova *et al.* 1998). The results are summarized in Table 3. The correction factor to the BH distance scale is $k = 0.89 \pm 0.06$. The statistical-parallax analysis thus also requires a reduction of the BH distance scale. Of other results we point out rather small dispersion of association velocities relative to the circular rotation law: the ellipsoid semiaxes are equal to $\sigma_u = 8.2$ km s^{-1}, $\sigma_v = 5.7$ km s^{-1}, and $\sigma_w = 5.0$ km s^{-1}; i.e., they are much smaller than the corresponding parameters for the Cepheid subsystem [$\sigma_u = 15.0$ km s^{-1}, $\sigma_v = 10.3$ km s^{-1}, and $\sigma_w = 8.5$ km s^{-1}, Rastorguev *et al.* (1999)].

Table 1. Trigonometric and photometric parallaxes of OB-associations

Association	l	b	r_{BH}, kpc	p_{BH}, 0.″001	p_t, 0.″001	ε_p, 0.″001	r_t, kpc	n
Sgr OB1	7.6	–0.8	1.6	0.63	0.65	0.18	1.5	29
Ser OB1	16.7	0.0	1.9	0.52	1.88	0.17	0.5	12
Cyg OB3	72.8	2.0	2.3	0.44	0.43	0.16	2.3	18
Cyg OB1	75.9	1.1	1.8	0.55	0.59	0.20	1.7	14
Cyg OB8	78.0	3.3	2.3	0.44	0.81	0.27	1.2	10
Cyg OB7	89.1	0.0	0.8	1.27	1.39	0.11	0.7	28
Cep OB2	102.2	4.6	0.9	1.10	0.97	0.12	1.0	47
Cep OB1	104.2	–1.0	3.5	0.29	0.65	0.15	1.6	24
Cep OB3	110.5	2.6	0.9	1.15	1.19	0.21	0.8	15
Cas OB5	116.1	–0.5	2.5	0.40	0.08	0.19	12.5	13
Per OB1	134.7	–3.1	2.3	0.44	0.77	0.16	1.3	63
Cas OB6	135.1	0.8	2.2	0.46	1.47	0.33	0.7	13
Cam OB1	141.2	0.9	1.0	1.00	1.13	0.25	0.9	33
Aur OB1	173.9	0.2	1.3	0.76	1.69	0.21	0.6	20
Ori OB1	207.0	–17.6	0.5	2.00	2.43	0.09	0.4	61
Gem OB1	189.0	2.3	1.5	0.66	0.49	0.27	2.0	17
Mon OB2	207.5	–1.6	1.5	0.66	–0.01	0.32		18
CMa OB1	224.6	–1.5	1.3	0.76	0.61	0.21	1.6	10
Coll 121	238.5	–8.4	0.7	1.45	1.65	0.22	0.6	13
NGC 2439	245.3	–4.1	4.4	0.23	0.77	0.12	1.3	10
Vela OB2	262.1	–8.5	0.5	2.00	1.97	0.25	0.5	12
Vela OB1	264.9	–1.4	1.8	0.55	1.13	0.15	0.9	18
Car OB1	286.5	–0.5	2.5	0.40	0.53	0.05	1.9	18
Car OB2	290.4	0.1	2.2	0.46	0.39	0.12	2.6	12
Cru OB1	294.9	–1.1	2.5	0.40	0.61	0.17	1.6	19
Cen OB1	304.2	1.4	2.4	0.42	0.56	0.14	1.8	32
Ara OB1A	337.7	–0.9	1.4	0.72	0.89	0.18	1.1	10
Sco OB1	343.7	1.3	1.9	0.52	0.15	0.18	6.7	16
Sco OB2	351.4	18.9	0.2	6.25	7.04	0.36	0.1	10

REFINING THE DISTANCE SCALE OF OB-ASSOCIATIONS VIA ADJUSTMENT OF THE ROTATION-CURVE PARAMETERS

As noted above, the rotation-curve parameters inferred from an analysis of radial velocities and proper motions have different sensitivity toward the choice of the distance scale ($r = kr_{BH}$). Statistical parallax technique constitutes the most rigorous use of this circumstance for the distance-scale refinement (see previous Section). However, generally speaking, the parameters thus inferred are inevitably biased should incorrect standard errors be adopted for the observed quantities – radial velocities and proper motions. We cannot be certain that the adopted standard errors of the initial data (this concerns mainly the radial velocities of OB-stars) are correct, and therefore can never rule out systematic biases in the inferred parameters the distance-scale correction factor included. It is therefore of interest to construct a kinematically adjusted distance scale for associations under a simplified assumption about the isotropy of the distribution of residual velocities of the objects considered. It can be easily understood that the first derivative of the angular rotation velocity with respect to Galactocentric distance, Ω_0', inferred from an analysis of proper motions is, to a first approximation, virtually independent of the adopted distance-scale factor, k, whereas the value inferred form an analysis of radial velocities is inversely proportional to factor k ($\Omega_0' = \text{const}/k$). This very circumstance can be used to find a distance-scale factor k that would best reconcile the rotation-curve parameters inferred from the analyses of radial velocities and proper motions. Strictly speaking, k is determined from a joint solution of the radial-velocity and proper-motion equations as a parameter minimizing the sum of squared normalized residual velocities.

Given a model of circular rotation of the Galactic disk and Bottlinger equations (Kulikovskiĭ 1985), we

Table 2. Radial velocities and proper motions of OB-associations

Association	l	b	r_{BH}, kpc	V_r, km s^{-1}	ε_{V_r}, km s^{-1}	n_r	μ_l	$\varepsilon_{\mu l}$	μ_b	$\varepsilon_{\mu b}$	n_{lb}
							0.″001 yr^{-1}		0.″001 yr^{-1}		
Sgr OB5	0.0	−1.2	3.0	−6.5	10.8	4	0.1	1.0	0.1	1.3	3
Sgr OB1	7.6	−0.8	1.6	−9.5	1.8	38	−1.6	0.2	−1.3	0.2	29
Sgr OB7	10.8	−1.6	1.7	−4.0	9.9	3	0.0	0.2	−3.3	0.1	2
Sgr OB4	12.1	−1.0	2.4	0.5	3.3	8	−0.7	0.8	−0.8	1.4	3
Ser OB1	16.7	0.0	1.9	−5.0	5.1	17	−0.7	0.3	−0.8	0.5	12
Sct OB3	17.3	−0.8	1.7	6.0	6.4	7	−0.9	0.3	−0.6	0.6	3
Ser OB2	18.2	1.6	2.0	−4.0	1.8	6	−0.8	0.3	−1.4	0.1	5
Sct OB2	23.2	−0.6	2.0	−11.0	7.3	7	−0.5	1.1	−0.6	0.5	6
Vul OB1	60.4	0.0	2.0	7.8	5.7	8	−4.7	0.6	−0.1	0.2	8
Vul OB4	60.7	−1.2	1.0	−2.9	4.3	3	−4.1	0.6	−1.9	0.7	3
Cyg OB3	72.8	2.0	2.3	−8.5	2.1	30	−7.6	0.2	−1.2	0.3	18
Cyg OB1	75.9	1.1	1.8	−15.0	1.7	35	−6.3	0.3	−0.8	0.3	14
Cyg OB9	77.8	1.8	1.2	−17.0	4.6	11	−6.7	0.5	−1.4	0.3	8
Cyg OB8	78.0	3.3	2.3	−25.0	3.4	8	−6.2	0.1	0.8	0.4	10
Cyg OB4	82.8	−7.5	1.0	−5.1	0.7	2	−0.7	1.2	−1.3	1.1	2
Cyg OB7	89.1	0.0	0.8	−7.1	2.3	16	−3.2	0.7	−1.1	0.2	28
Lac OB1	96.8	−17.7	0.6	−13.8	2.8	2	−3.3	0.2	−4.4	0.3	2
Cep OB2	102.2	4.6	0.9	−15.0	1.3	35	−3.8	0.2	−0.8	0.2	47
Cep OB1	104.2	−1.0	3.5	−55.8	3.1	13	−4.0	0.2	−0.4	0.2	24
Cas OB2	112.0	0.0	2.6	−45.0	13.4	2	−4.5	0.4	−0.1	0.5	5
Cep OB3	110.5	2.6	0.9	−21.8	1.7	8	−2.2	0.3	−1.7	0.4	15
Cas OB5	116.1	−0.5	2.5	−43.1	6.8	9	−3.6	0.3	−2.0	0.3	13
Cas OB4	120.1	−0.3	2.9	−38.0	0.0	4	−2.1	0.5	−1.3	0.4	7
Cas OB14	120.4	0.8	1.1	−15.0	3.5	4	1.6	1.2	−1.1	0.6	3
Cas OB7	123.0	1.2	2.5	−37.0	7.2	3	−2.0	0.2	−0.9	0.2	8
Cas OB1	124.8	−1.7	2.5	−42.0	7.6	7	−2.0	0.0	−1.6	0.8	3
NGC 457	126.7	−4.4	2.5	−46.0	6.4	2	−1.6	0.1	−1.7	0.1	2
Cas OB8	129.2	−1.0	2.9	−32.5	2.5	8	−1.4	0.2	−1.0	0.6	9
Per OB1	134.7	−3.1	2.3	−41.7	0.8	71	0.1	0.1	−1.7	0.2	63
Cas OB6	135.1	0.8	2.2	−41.2	3.0	10	−0.6	0.4	−1.2	0.4	13
Cam OB1	141.2	0.9	1.0	−10.8	2.4	29	0.6	0.3	−1.7	0.3	33
Cam OB3	147.0	2.9	3.3	−27.6	11.1	3	1.6	1.2	0.9	0.5	3
Per OB2	160.4	−16.5	0.4	19.8	1.7	7	6.5	0.9	−1.3	0.7	7
Aur OB1	173.9	0.2	1.3	0.1	3.3	24	3.0	0.3	−2.0	0.4	20
Ori OB1	207.0	−17.6	0.5	25.0	0.9	64	0.7	0.2	0.6	0.2	59
Aur OB2	173.3	−0.2	3.0	−1.5	4.0	3	0.0	0.7	−0.9	0.1	2
Gem OB1	189.0	2.3	1.5	16.6	1.5	19	1.5	0.3	−1.1	0.2	17
Mon OB1	202.2	1.2	0.7	23.3	4.9	7	1.9	0.7	−2.1	0.8	7
Mon OB2	207.5	−1.6	1.5	22.0	2.5	27	−1.0	0.3	−1.2	0.4	18
CMa OB1	224.6	−1.5	1.3	32.8	5.7	8	−3.2	0.2	−2.6	0.3	10
Coll 121	238.5	−8.4	0.7	34.3	2.6	11	−5.2	0.3	−1.0	0.3	13
NGC 2362	237.9	−5.9	1.5	35.0	5.7	6	−4.2	0.8	0.1	0.5	3
NGC 2439	245.3	−4.1	4.4	60.8	4.8	2	−4.5	0.3	−0.7	0.3	10
Coll 140	244.5	−7.3	0.4	12.4	2.7	6	−7.0	0.4	−5.3	0.8	6
Vela OB2	262.1	−8.5	0.5	24.0	2.7	13	−9.7	0.4	−1.4	0.5	12
Vela OB1	264.9	−1.4	1.8	23.0	1.7	17	−6.7	0.3	−1.3	0.2	18
Car OB1	286.5	−0.5	2.5	−4.0	1.6	25	−7.6	0.1	−1.0	0.1	18
Tr 16	287.3	−0.3	2.6	1.3	1.1	4	−7.2	0.4	−0.9	0.0	2
Coll 228	287.6	−1.0	2.5	−28.0	5.7	2	−6.7	0.5	−1.0	0.1	2
Car OB2	290.4	0.1	2.2	−3.5	2.3	16	−6.8	0.2	−0.8	0.2	12
Cru OB1	294.9	−1.1	2.5	−3.0	2.0	33	−6.0	0.2	−0.8	0.1	19
Cen OB1	304.2	1.4	2.4	−20.0	2.0	26	−4.9	0.1	−0.9	0.2	32
R 103	332.4	−0.8	4.0	−56.5	8.0	8	−4.0	0.2	−2.0	0.3	4
Ara OB1B	338.0	−0.9	3.5	−34.0	5.1	8	−3.6	0.2	−2.2	0.3	6
Ara OB1A	337.7	−0.9	1.4	−11.7	9.0	7	−2.5	0.4	−2.2	0.4	10
Sco OB1	343.7	1.3	1.9	−27.6	2.2	26	−1.5	0.2	−0.7	0.2	16
Sco OB2	351.4	18.9	0.2	−3.3	0.9	10	−24.0	0.6	−8.7	0.7	10
HD 156154	351.4	1.4	2.6	−8.5	1.8	2	−1.2	0.1	−0.9	0.9	2
Sco OB4	352.7	3.2	1.2	4.5	0.3	4	−0.8	0.1	−2.3	0.2	4

Table 3. Kinematical parameters of the system of OB-associations and correction factor k ($r = kr_{BH}$) to the BH distance scale as inferred by applying statistical-parallax technique to a sample of 59 associations

u_0, km s^{-1}	v_0, km s^{-1}	w_0, km s^{-1}	σ_u, km s^{-1}	σ_v, km s^{-1}	σ_w, km s^{-1}	Ω_0, km s^{-1} kpc^{-1}	Ω', km s^{-1} kpc^{-2}	Ω'', km s^{-1} kpc^{-3}	k
8.2 ± 1.3	11.9 ± 1.1	9.5 ± 0.9	8.2 ± 1.1	5.8 ± 0.8	5.0 ± 0.8	29.1 ± 1.0	−4.57 ± 0.20	1.32 ± 0.14	0.89 ± 0.06

Table 4. Parameters of the Galactic rotation curve inferred by analyzing radial velocities and proper motions of OB-associations at $k = 0.74$

N	u_0, km s^{-1}	v_0, km s^{-1}	Ω', km s^{-1} kpc^{-2}	Ω'', km s^{-1} kpc^{-3}	Ω_0, km s^{-1} kpc^{-1}	σ_0, km s^{-1}
118	7.3 ± 1.0	12.0 ± 1.3	−5.0 ± 0.2	1.5 ± 0.2	31 ± 1	7.4

can write the following expressions for radial velocities and proper motions of OB-associations:

$$\begin{aligned} V_r &= -(u_0\cos l\cos b + v_0\sin l\cos b + w_0\sin b) \\ &+ R_0\Omega_0'(R-R_0)\sin l\cos b \\ &+ 0.5R_0\Omega_0''(R-R_0)^2\sin l\cos b + V_{r,\,\mathrm{pec}}, \end{aligned} \tag{2}$$

$$\begin{aligned} 4738\mu_l kr_{\mathrm{BH}} &= -(-u_0\sin l + v_0\cos l) \\ &+ \Omega_0'(R-R_0)(R_0\cos l - kr_{\mathrm{BH}}\cos b) \\ &+ 0.5\Omega_0''(R-R_0)^2(R_0\cos l - kr_{\mathrm{BH}}\cos b) \\ &- \Omega_0 kr_{\mathrm{BH}}\cos b + V_{l,\,\mathrm{pec}}, \end{aligned} \tag{3}$$

where $V_{r,\,\mathrm{pec}}$ and $V_{l,\,\mathrm{pec}}$ are the components of peculiar velocity and R, the Galactocentric distance of the star computed as follows:

$$R^2 = (kr_{\mathrm{BH}}\cos b)^2 + R_0^2 + 2R_0 kr_{\mathrm{BH}}\cos l\cos b. \tag{4}$$

We then solved the radial-velocity and proper-motion equations with weight factors p_{V_r} and p_{V_l} introduced to allow for observational errors and "cosmic" velocity dispersion:

$$p_{V_r} = (\sigma_0^2 + \varepsilon_{V_r}^2)^{-1/2}, \tag{5}$$

$$p_{V_l} = (\sigma_0^2 + (4738\varepsilon_{\mu l} kr_{\mathrm{BH}})^2)^{-1/2}. \tag{6}$$

Here, σ_0 is the dispersion of residual velocities of associations relative to the rotation curve (the so-called "cosmic" velocity dispersion) under the assumption of isotropic distribution. We found $\sigma_0 = 7.4$ km s^{-1} via iterative technique. Even if we adopt 10 km s^{-1} as the initial value, the first iteration already yields $\sigma_0 = 7.6$ km s^{-1}.

Distance-scale factor k is virtually independent of R_0 over a wide range of solar Galactocentric distance values, $R_0 = 6$–9 kpc. To determine other parameters, we adopted a solar Galactiocentric distance of $R_0 = 7.1$ kpc (Dambis *et al.* 1995; Rastorguev *et al.* 1994; Glushkova *et al.* 1998). We assumed that the Sun's velocity component w_0 along the z-axis is $w_0 = 7$ km s^{-1} (Rastorguev *et al.* 1999).

We applied the method described above to a sample of 59 associations, each with at least two stars with known radial velocities and at least two stars with proper motions from the Hipparcos catalog (Table 2). We used standard least squares method [see p. 499 in the book of Press *et al.* (1987)] to solve the sets of conditional equations (2) and (3), which are linear in parameters u_0, v_0, Ω_0', Ω_0'', and Ω_0 with weight factors (5) and (6) for each value of parameter k and then determined the parameter that minimizes the sum of squared normalized residual velocities.

Figure 2 shows χ^2 plotted as a function of distance-scale factor, k. Quantity χ^2 is minimum at $k = 0.74$. The standard error of the k value thus inferred is about 0.1 [see Hawley *et al.* (1986) for the algorithm used to estimate this error]. Table 4 gives rotation-curve parameters u_0, v_0, Ω_0', Ω_0'', and Ω_0 and their standard errors; the number of equations N, and the rms residual, σ_0, at $k = 0.74$.

Note that a threefold increase in the adopted proper-motion errors changes parameter k by a mere 6% ($k = 0.80$), and a similar increase of the radial-velocity errors has even weaker effect on the final result: l changes by 2% ($k = 0.72$). In either case, the change is swamped by the standard error of k ($\sigma = 0.1$). Our result is thus extremely robust toward eventual errors in the adopted standard errors of observational data.

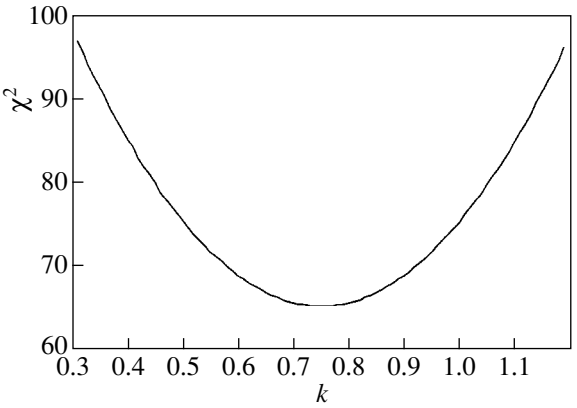

Fig. 2. χ^2 plotted as a function of distance-scale factor, k.

CONCLUSION

We found that trigonometric parallaxes of OB-associations and field stars require a 10–20% reduction of the photometric distance scale of Blaha and Humphreys (1989) (BH): $r_t = (0.88 \pm 0.05)\, r_{BH}$ for OB-associations and $r_t = (0.84 \pm 0.02)\, r_{BH}$ for field stars. This conclusion is corroborated by a kinematical analysis of objects considered: the kinematically adjusted distance scale of OB-associations is about 25% shorter than the BH distance scale, $r_k = (0.74 \pm 0.10)\, r_{BH}$.

Furthermore, a similar reduction of the BH distance scale also follows from the results obtained via a more rigorous statistical-parallax method: $r_{sp} = (0.89 \pm 0.06) r_{BH}$.

The short distance scale of OB-associations, which is equal to about 80% of the BH distance scale, $r_t = (0.8 \pm 0.1) r_{BH}$, is consistent with the short distance scale of classical Cepheids defined by Berdnikov and Efremov (1985) PL relation (Sitnik and Mel'nik 1996). The fact that the trigonometric and kinematically adjusted distance scales of OB-associations agree with the short distance scale of Cepheids serves as additional argument in favor of the short distance scale of the Universe.

ACKNOWLEDGMENTS

We are grateful to the referee for useful comments. The work was supported by the Russian Foundation for Basic Research (grants nos. 99-02-17 842, 98-02-16 107 and 00-02-17 804), the Council for the Support of Leading Science Schools (grant no. 00-15-96 627), and "Astronomy" State Science and Technology Program.

REFERENCES

1. L. N. Berdnikov and Yu. N. Efremov, Astron. Tsirk., No. 1388, 1 (1985).
2. C. Blaha and R. M. Humphreys, Astron. J. **98**, 1598 (1989).
3. A. K. Dambis, A. M. Mel'nik, and A. S. Rastorguev, Pis'ma Astron. Zh. **21**, 331 (1995) [Astron. Lett. **21**, 291 (1995)].
4. P. T. de Zeeuw, R. Hoogerwerf, J. H. J. de Bruijne, *et al.*, Astron. J. **117**, 354 (1999).
5. M. Duflot, P. Figon, and N. Meyssonier, Astron. Astrophys., Suppl. Ser. **114**, 269 (1995).
6. M. Feast and R. Catchpole, Mon. Not. R. Astron. Soc. **286**, 1 (1997).
7. M. Feast and P. Whitelock, Mon. Not. R. Astron. Soc. **291**, 683 (1997).
8. E. V. Glushkova, A. K. Dambis, A. M. Mel'nik, and A. S. Rastorguev, Astron. Astrophys. **329**, 514 (1998).
9. S. L. Hawley, W. H. Jefferys, T. G. Barnes, *et al.*, Astrophys. J. **302**, 626 (1986).
10. N. Kaltcheva and J. Knude, Astron. Astrophys. **337**, 178 (1998).
11. P. G. Kulikovskiĭ, *Stellar Astronomy* (Nauka, Moscow, 1985).
12. A. M. Mel'nik, T. G. Sitnik, A. K. Dambis, *et al.*, Pis'ma Astron. Zh. **24**, 689 (1998) [Astron. Lett. **24**, 594 (1998)].
13. M. Miyamoto and Zhu Zi, Astron. J. **115**, 1483 (1998).
14. C. A. Murray, *Vectorial Astrometry* (Adam Hilger, Bristol, 1983; Naukova Dumka, Kiev, 1986).
15. W. H. Press, B. P. Flannery, S. A. Teukoisky, and W. T. Vetterling, *Numerical Recipes: The Art of Scientific Computing* (Cambridge Univ. Press, Cambridge, 1987).
16. A. S. Rastorguev, O. V. Durlevich, E. D. Pavlovskaya, and A. A. Filippova, Pis'ma Astron. Zh. **20**, 688 (1994) [Astron. Lett. **20**, 591 (1994)].
17. A. S. Rastorguev, E. V. Glushkova, A. K. Dambis, and M. V. Zabolotskikh, Pis'ma Astron. Zh. **25**, 689 (1999) [Astron. Lett. **25**, 595 (1999)].
18. N. Reid, Annu. Rev. Astron. Astrophys. **37**, 191 (1999).
19. T. G. Sitnik and A. M. Mel'nik, Pis'ma Astron. Zh. **22**, 471 (1996) [Astron. Lett. **22**, 422 (1996)].
20. T. G. Sitnik and A. M. Mel'nik, Pis'ma Astron. Zh. **25**, 194 (1999) [Astron. Lett. **25**, 156 (1999)].
21. F. van Leeuwen, Astron. Astrophys. **341**, L71 (1999).
22. The Hipparcos and Tycho Catalogues (European Space Agency, 1997), Vols. 1–20.

Translated by A. Dambis